EFFECT OF AN ARTIFICIAL OYSTER REEF ON WAVE ATTENUATION

LUIS SIGEL

EFFECT OF AN ARTIFICIAL OYSTER REEF ON WAVE ATTENUATION

LUIS SIGEL

by

Luis Sigel

to obtain the degree of

Master of Science
in Civil Engineering

at the TU Delft University of Technology
to be defended publicly on the 26.08.2021

Student Nr:	5159148	
Project duration	Dec 2020 - Aug 2021	
Thesis committee	Dr. ir. B.C. van Prooijen	TU Delft
	Dr. M.F.S. Tissier	TU Delft
	Dr. ir. P.L.M. de Vet	TU Delft
	Dr. ir. M.A de Schipper	TU Delft

An electronic version of this thesis is available at http://repository.tudelft.nl/.

ABSTRACT

An increasing amount of the worlds coastal regions suffer from structural erosion due to anthropogenic influences. A prime example of this phenomenon is the Oosterschelde, Netherlands, where the partial closure of an estuary lead to a decline of the local intertidal flats, threatening the valuable functions they provide as an ecosystem and for shore protection. A sustainable measure to slow down the decline is the usage of wave disrupting oyster reefs, which reduce the wave energy on the flat, thus reducing erosion. As of now, the conditionality and extend of the wave attenuation effect of such reefs is still widely unknown. This is thwarting a more extensive usage of oyster reefs for erosion management since the actual effects of such a reef are highly uncertain prior to construction.

This thesis was designed to investigate and quantify wave attenuation capabilities of an artificial oyster reef in a macrotidal environment, improving the understanding of the impact of such structures on their physical environment. A wave analysis was carried out on a reef using field data, allowing for the quantification of attenuation, the identification of processes, a parameterization of the results and an insight on the predictability of attenuation.

Extensive field data was acquired on seven locations on a transect over the investigated reef, including pressure and velocity data. The reef was built using shell filled wire gabions and is orientated perpendicular to the main wind direction. It has dimensions of approximately 120 m length, 8 m width and 0.8 m height. The reef crest is located 0.5 m above mean low water level and 2.3 m below mean high water level, being emerged approximately 30 % of the time. Incoming waves are characterized by maximum significant wave heights of 0.8 m and maximum mean periods of 3 seconds.

Wave attenuation was quantified by comparing the energy flux in front of (seaward) and behind (shoreward) the reef under different hydrodynamic conditions. The conditionality of attenuation was found to be best represented by the relative submergence $d_s / H_{m0,i}$, which represents the ratio of the freeboard on top of the reef and the incoming wave height. Attenuation was found until a $d_s / H_{m0,i}$ ratio of approximately 4. Compared to the bare tidal flat in front of the reef, the reef attenuated energy on average 18 times more effectively per distance. The spatial footprint of the reef was found to vary strongly with different $d_s / H_{m0,i}$ ratios, but being roughly of the same order of magnitude as the reef length.

Reflection, overtopping, wave breaking and friction were identified as the main mechanisms behind energy attenuation. An attempt to parameterize these was done using dimensionless numbers, which can be used to predict attenuation by using incoming

wave, and reef characteristics. The determined processes were best represented by the parameters $d_s / H_{m0,i}$ and L_{01} / d_s.

Three empirical relations describing wave attenuation over breakwaters were used to investigate whether existing formulas can predict wave attenuation over the observed oyster reef. The measured and calculated results show a strong correlation of R ~ 0.9 but need to be tuned to reach reasonable root mean square errors. This implies that such existing formulas can be adjusted to represent oyster reefs, making them a possible tool to predict oyster reef performance in the future.

The findings show that the present oyster reef is effective in attenuating waves and contribute to the overall understanding of how oyster reefs can reduce erosion. A better insight on the quantity of attenuation and the spatial footprint of the reef's effects was achieved. The footprint of the reef's effect is hereby limited to an area close to it, meaning that the reefs impact on erosion should not be overestimated. Such a reef should thus rather be seen as a complementary measure against erosion, stabilising the local area. As a next step, setting up a numerical model is recommended, where the wave attenuation can be linked to actual erosion quantities. Quantitative research on additional oyster gabions can further be used to refine existing empirical relations, creating some predictability of transmission values over oyster reefs.

CONTENTS

List of Figures

LIST OF TABLES

List of Symbols

WNW = West North West
ESE = East South East
SSE = South South East
MHW = mean high water
MLW = mean low water
K_t = transmission coefficient wave height
$K_{t,f}$ = transmission coefficient energy flux
K_r = reflection coefficient
H_t = transmitted wave height
H_i = incident wave height
H_{m0} = spectral wave height
H_s = significant wave height
a = wave amplitude
L = wave length
L_i = incident wave length
L_t = transmitted wave length
L_p = peak wave length
T = period
T_p = peak period
f_p = peak frequency
k = wave number
c = phase velocity
c_g = group velocity
F = energy flux
ρ = density
g = gravitational acceleration = 9.81 m/s^2
μ = dynamic fluid viscosity
D_{50} = grain diameter
n = porosity of structure
h_s = structure height
h_p = pressure sensor height from bed
d = water depth
d_s = water depth over structure crest
R_c = structure crest freeboard (=d_s in case of submergence)
α = seaward slope of structure
B = structure width
ξ = breaker parameter = $tan(\alpha)/s_{op}^{0.5}$
s_{op} = wave steepness = $2\pi H_i/(gT_p^2)$
K_p = pressure response factor

f_c = cut off frequency
$S_{\eta\eta}$ = water surface elevation power spectral density
m_0 = zeroth spectral moment
N_{Ursell} = Ursell Nr
xi = Iribarren Nr.
NAP = Normaal Amsterdams Peil
MSL = Mean sea level
F = Fetch [m]
U_{10} = 10 m average wind speed

1

INTRODUCTION

Coastal zones play an important role in today's civilization with a growing population located close to the ocean (Neumann et al. 2015, Hallegatte et al. 2013) and an immense importance for the world's economy (*WorldBank* 2021). At the same time, coastal regions have enormous ecological value and contribute to an estimated 38 % of the worlds ecosystem services (Costanza et al. 1998). However, increasing human-induced pressure on coastal regions and poor local governance structures have led to a decline of coastal ecosystems as well as of their attributed ecosystem services (Aguilera et al. 2020). Additionally, Climate change and Sea level rise put further strain on the world's coastal regions (Gornitz 1991). As a result, an increasing amount of the world's coasts are currently affected or threatened by coastal erosion (Zhu et al. 2010, Ysebaert et al. 2019), expecting to reach unmanageable conditions in the near future (Shi and Kasperson 2015). The usual response to combat these problems is the implementation of conventional structures such as breakwaters, sea walls or revetments, characterised as hard structures. Such structures have received increasing criticism in the past decade, however, due to their expensive and laborious maintenance requirements (Temmerman et al. 2013) and their negative impacts on the adjacent ecosystem such as loss of habitat, reduction of water quality and increased scour (Currin 2019). Furthermore, hardened structures can reduce the capability of shorelines to naturally keep up with sea-level rise, leading to the drowning of the low lying intertidal ecosystems (Currin 2019, Temmerman et al. 2013). As a response to these drawbacks of conventional solutions, new, ecosystem-based strategies have been brought into practice in recent years.

1

An ecosystem-based coastal defence approach aims to create, restore or maintain a coastal ecosystem that delivers ecosystem services like flood or erosion protection (Salvador de Paiva et al. 2018). Additionally, an ecosystem-based flood and erosion defence offers many other benefits compared to conventional approaches, such as water filtration, carbon sequestration, fishing nurseries and recreational space (Temmerman et al. 2013). Typically the approach is introducing one or several ecosystem engineering species, which are capable of modulating the availability of resources in its surroundings by changing the physical state of biotic or abiotic material (Jones et al. 1994). Interesting for coastal defence are hereby species whose temporal and spatial scale of influence are much larger than the temporal and spatial scale they occupy themselves, examples being oyster reefs, seagrass or salt marshes (Borsje et al. 2011). Such species can contribute to coastal defence by trapping sediment and attenuating waves (Borsje et al. 2011, Temmerman et al. 2013). The basic principle is hereby visualised in figure 1.1. In comparison to conventional methods, an ecosystem-based defence can offer an equal or superior solution considering sustainability, adaptability to climate change and cost-effectiveness, if certain conditions are met (Borsje et al. 2011, Temmerman et al. 2013, Vriend et al. 2014).

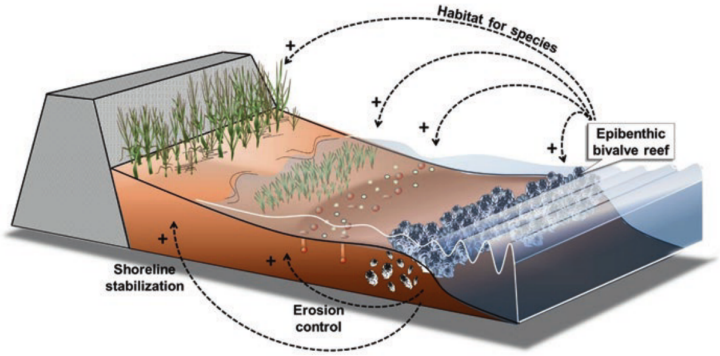

Figure 1.1: Principle of ecosystem services provided by reef structures. Taken from Ysebaert et al. 2019

1.1. RESEARCH AIM

Many of the intertidal flats located in the Netherlands suffer from structural erosion due to human interventions. As part of a prevention scheme, the Dutch government wants to implement ecosystem-based solutions to protect its coastal areas. A focus is hereby set on the reduction of the wave energy on top of the reef, which can be directly linked to erosion due to waves ability to stir up sediment. Fitting to the dutch coastal ecosystem, the restoration of previously lost oyster populations is envisaged, bringing back the wave disrupting ecosystem service they provide. As part of this strategy, several artificial oyster reefs were built for research purposes in the Oosterschelde, Netherlands, using wire gabions as a recruitment base (see figure 1.2). The research aim of this thesis is to increase the knowledge of the processes involved in wave attenuation over such reefs,

thus creating some predictability of the impacts on the environment. This can then give further insights into the potential usages of oyster reefs at other locations.

Figure 1.2: Artificial oyster reef built on an intertidal flat. Photo taken during emergence at low tide.

1.2. PROBLEM STATEMENT

The effectiveness of oyster reefs in reducing coastal erosion was observed in many studies (Scyphers et al. 2011, Ysebaert et al. 2019, Wiberg et al. 2018). However, literature is having difficulties in quantifying the effects of oyster reefs, with observations often varying significantly at different sites. This makes decision makers reluctant to push oyster reef projects forward, since the conditions required for a successful implementation are still widely unknown. This can be traced back to a lack of knowledge of the wave attenuation processes over oyster reefs. The existing research approaching this lack of knowledge, was predominantly done in scaled laboratory experiments. Field experiments on the other hand are scarce and are mainly conducted in the microtidal environment of the US coasts in the Gulf of Mexico. Additionally, the research is distributed among many oyster reef structure types, whose geometry can vary substantially. For the structure type observed in this study, oysters recruited on a shell filled gabion, as well as for the present macrotidal environment, no extensive field or laboratory data was collected so far.

At the study tidal flat, reduced erosion has been observed (Walles, Salvador de Paiva, et al. 2014). However, no formal link to wave attenuation by the present oyster reef has been drawn yet. An attempt to quantify wave attenuation has been made after construction in 2010 (cite) but is lacking validity because of a lack of oyster recruitment, a short measurement period and faulty data.

To quantify wave attenuation over the reef, wave data in the form of pressure measurements has to be collected. However, the study site is characterised by a macrotidal and low energy environment. In such conditions, it can prove difficult to obtain reliable wave data from pressure measurements. Thus steps have to be taken to ensure an adequate data quality

1.3. RESEARCH QUESTION AND OBJECTIVES

In concordance with the research aim, the following research question is explored in this thesis.

- How effectively can an artificial gabion oyster reef contribute to erosion prevention on a macrotidal flat by attenuating waves?

In the process of answering this question, several research objectives are explored. Objectives 1, 2 and 3 discuss the main objective of this thesis, regarding the quantification and predictability of the reef's effects. Additionally, two sub-questions are explored which cover important information needed to fulfil the objectives. These two questions are presented in section 1.4, which indicates the approach. The research objectives are:

1. Obtain a comprehensive and extensive data set with measurements of wave characteristics at the observed oyster reef.

2. Quantify the wave attenuation and identify the processes which govern the modification of waves over the observed oyster reef.

3. Parameterize the effect of the modification of the wave field by the oyster reef and investigate potential predictability.

1.4. APPROACH

The aforementioned objectives are approached by conducting extensive field measurements at the study site in the Oosterschelde, Netherlands. The resulting data is processed using the Matlab environment. Wave data is derived using spectral analysis, which is then used to describe wave attenuation over the oyster reef. The results are then conceptualised and compared to literature. Finally, an attempt to predict the results using existing empirical formulations is made. Apart from the three mentioned objectives, two side questions are covered in detail. These were deemed necessary as background knowledge on the research site and the measurement method.

A What are the insights on the morphological and hydrodynamic conditions at the research site?

   a What are the erosional trends on the tidal flat and what is the cause of this?

   b What hydrodynamic forcing can be expected around the research site?

B How do pressure sensors cope in the present macrotidal, low energy environment?

a How can the collected data set be filtered to avoid unrealistic amplifications of short waves in the high frequency range?

b During what conditions can the instruments be expected to deliver reliable results?

The thesis outline is summarized in figure 1.3

1

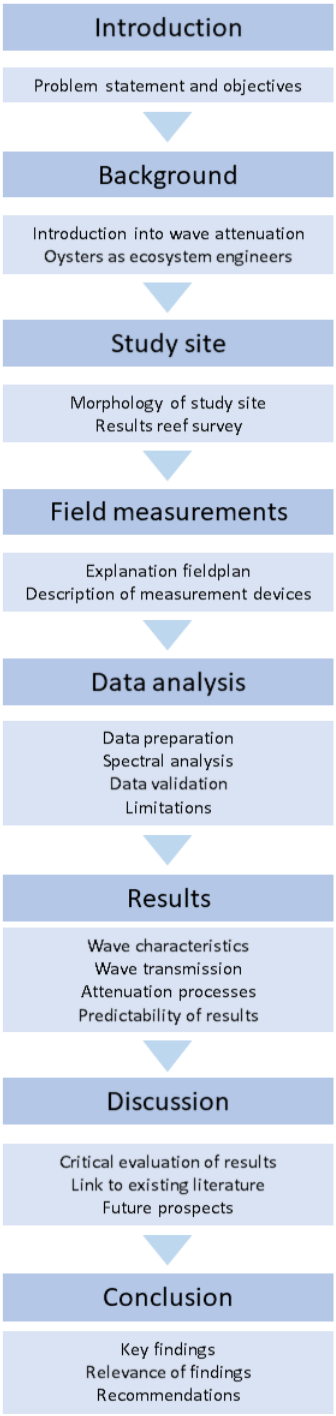

Figure 1.3: Thesis structure

2

BACKGROUND

To understand the background of the usage of oyster reefs for coastal protection, a literature review is presented. First a brief overview about oysters as ecosystem engineers is given, highlighting the advantages of healthy oyster populations in coastal regions. Then the principle of wave attenuation by structures is explained, showing how oyster reefs can reduce wave energy. Third, existing empirical relations describing wave attenuation over submerged breakwaters are laid out. These can be used to investigate if empirical breakwater relations can produce reliable predictions for oyster reefs as well. And lastly, the current literature on wave attenuation over oyster reefs is summarised.

2.1. OYSTERS AS ECOSYSTEM ENGINEERS

Oysters used to be a widely common species in many of the world's estuaries, supporting local economies and dominating local ecology (Kirby 2004). Anthropogenic influence however lead to an estimated global loss of 85 % of oyster reef ecosystems compared to historic conditions, with coastal regions in Europe struck especially hard (Beck et al. 2011). This decline led to negative impacts on the local ecosystem and communities, because of the many ecosystem services that oyster reefs provide. Oyster reefs act as an important habitat for many species, increasing biodiversity and leading to positive effects on recreational fisheries (Fisheries 2020, Scyphers et al. 2011, Borsje et al. 2011). Oysters are furthermore filter feeders that extract phytoplankton, algae, and both organic and anorganic particles, reducing turbidity in the process (Coen et al. 2007) and actively combating eutrophication (Wall et al. 2011). Located on intertidal areas Oyster reefs can also effectively reduce erosion and facilitate sedimentation (Borsje et al. 2011, Scyphers et al. 2011, Walles, Salvador de Paiva, et al. 2014). They do this by building three dimensional, complex structures, making them natural submerged breakwaters, which potentially attenuate waves and lead to less wave attack on their lee side(Wiberg et al. 2018). Another valuable characteristic of oyster reefs is their capability of responding to changes in abiotic conditions. This enables them to naturally grow with sea-level rise, resist drowning due to subsidence and self-repair after storm events(Walles, Mann, et al. 2015, Rodriguez et al. 2014).

2.2. WAVE TRANSMISSION OVER SUBMERGED BREAKWATERS

Oyster reefs are inhomogeneous and constantly changing systems. Yet their base geometry does resemble that of a classical breakwater. In literature, oyster reefs are thus often characterised as low crested, or submerged breakwaters (Ysebaert et al. 2019). Consequently, the theory regarding wave transmission over breakwaters is expected to have some relevance for the wave disrupting effects of oyster reefs. Some well known empirical relations regarding wave transmission are thus presented in this chapter. Later on, these formulations will be used in an attempt to predict the reef wave transmission.

2.2.1. TRANSMISSION

Breakwaters are an effective way of protecting coastal regions against severe wave attacks. The classical breakwater known from ports and marinas is hereby emerged, aiming for a near-complete removal of wave energy. But when some wave transmission is allowed or even desired, submerged breakwaters can be employed, removing only part of the wave energy. The amount of transmitted energy is hereby most often presented in the form of the transmission coefficient K_t, which is calculated using the incident, and the transmitted wave height, H_i and H_t respectively:

$$K_t = \frac{H_t}{H_i} \tag{2.1}$$

This transmission coefficient can be written as the function of a variety of incident wave and structure variables (Seabrook and Hall 1998):

$$H_t = f(\rho, g, \mu, d_{50}, n, H_i, L, d_s, \alpha, B, h_s, d) \tag{2.2}$$

Where ρ is the water density, g the gravitational acceleration, μ the dynamic fluid viscosity and n the porosity. The other parameters are defined in figure 2.1, which also shows the typical geometry of a submerged breakwater.

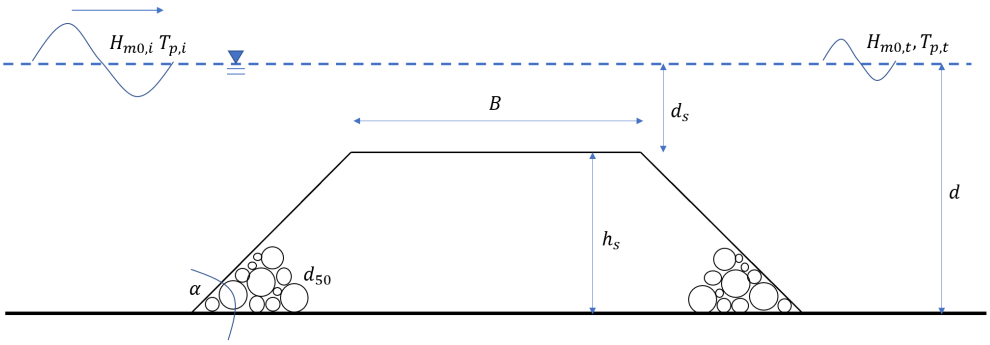

Figure 2.1: Definition plot for submerged breakwaters

These parameters can then be brought into a large variety of dimensionless forms, examples being:

$$K_t = f(\frac{d_s}{H_i}, \frac{B}{H_i}, \frac{L}{H_i}, \frac{h_s}{H_i}, \frac{d_{50}}{H_i}) \tag{2.3}$$

Such dimensionless numbers are used to describe the different relevant processes in wave transmission over breakwaters and are found in most empirical relations.

2.2.2. EMPIRICAL RELATIONS

A variety of empirical relations describing wave transmission over submerged breakwaters exist. Some of the most relevant and recent are: Van der Meer et al. 2005, Seabrook and Hall 1998 and Srineash and Murali 2019, which are presented in this section. All authors hereby use dimensionless numbers to parameterize the relevant processes in wave attenuation over a breakwater. Seabrook and Hall 1998 extensively describes this process and explains his usage of dimensionless numbers and which processes they represent. Before presenting all three formulations, Seabrook and Hall 1998s description of dimensionless parameters is briefly summarized since it can serve as a base understanding of parameterization of wave attenuation processes over a submerged structure.

Seabrook and Hall 1998 identified four processes as relevant for wave attenuation over breakwaters. The processes and the dimensionless parameters he linked to these are described as follows:

- $d_s/H_{m0,i}$ is described as the most important parameter regarding wave transmission. It describes the relative submergence of the structure and represents structure-induced wave breaking. Low values of this parameter come with low transmission coefficients since most or all waves break over the structure. At increasing $d_s/H_{m0,i}$ values, the influence of this parameter on K_t decreases, since a lower portion of the incident waves breaks over the structure.
- For a very low relative submergence, under wave breaking conditions, overtopping is expected to become an important process. The transmission hereby depends on the potential of waves overtopping the structure. As a representative parameter describing this, the relative crest width, $H_{i,m0}/B$ is used.
- Because of the typically rough surface, some energy is expected to dissipate due to friction. Seabrook and Hall 1998 relates this process to the Darcy-Weisbach expression for head loss, resulting in a representative dimensionless number of $(d_s * H_{m0})/(B * D_{50a})$, where D_{50a} is the nominal diameter of the armor rock.
- Lastly, flow within the structure leads to energy dissipation. This is related to the porosity of the armour layer, the wavelength reaching the structure crest and the geometry of the structure. The dimensionless parameter representing this is given as $(B * d_s)/(L * D_{50a})$.

SEABROK AND HALL FORMULATIONS

Seabrook and Hall 1998 conducted extensive 2D and 3D measurements in a laboratory on submerged rubble mound structures. The experiment consisted of a multitude of tests, with varying crest width, relative submergence and wave characteristics.

The suggested formula for wave attenuation reads:

$$K_t = 1 - (e^{-0.65 * \frac{d_s}{H_{m0,i}} - 1.09 * \frac{H_{m0,i}}{B}} + 0.047 * (\frac{B}{L} * \frac{d_s}{D_{50a}}) - 0.067 * (\frac{d_s}{B} * \frac{H_{m0,i}}{D_{50a}})) \tag{2.4}$$

Where the interpretation of the used dimensionless numbers was already given. The formula is not applicable in the case of an unusually wide, or narrow structure width B, where the equation does become unbound, resulting in unrealistic values of the transmission coefficient. Seabrook and Hall 1998 thus recommends only to apply the equation within the following bounds:

$$0 \leq \frac{B * d_s}{L * D_{50a}} \leq 7.08 \qquad 0 \leq \frac{d_s * H_{m0,i}}{B * D_{50a}} \leq 2.14 \tag{2.5}$$

The authors identified that the transmission coefficient is most sensitive to changes in the depth of submergence d_s, incident wave height $H_{m0,i}$ and structure crest width B. In terms of dimensionless numbers, they name $d_s/H_{m0,i}$, representing wave breaking, as most important. The conducted 3D tests concluded that incident wave angle plays little to no role and is thus not included in the formula. It should be noted that contrary to the Van der Meer et al. 2005 relations the Seabrook and Hall 1998 formulas can only be used for fully submerged rubble mound breakwaters.

VAN DER MEER FORMULATIONS

Van der Meer et al. 2005 developed several well known empirical relations for low crested structures. His work is a continuation on Van der Meer and Daemen 1994 and d'Angremond et al. 1996 and is based on using an extensive database collected about rubble mound structures. Structure crest width is determined as the most crucial parameter for accuracy in the developed relation. Ultimately two formulas for different relative crest widths ($B/H_{s,i}$) are proposed (Van der Meer et al. 2005).

$$For B/H_{s,i} < 8 \qquad K_t = -0.4 * \frac{d_s}{H_{s,i}} + 0.64 * (\frac{B}{H_{s,i}})^{-0.31} * (1 - e^{-0.5 * \xi_{op}}) \tag{2.6}$$

$$For B/H_{s,i} > 12 \qquad K_t = -0.35 * \frac{d_s}{H_{s,i}} + 0.51 * (\frac{B}{H_{s,i}})^{-0.65} * (1 - e^{-0.41 * \xi_{op}}) \tag{2.7}$$

Where d_s is defined positive downward from the breakwater crest and ξ_{op} is defined as the breaker parameter, which indicates wave breaking and is defined using the slope angle α and the wave steepness:

$$\xi_{op} = \frac{tan(\alpha)}{\sqrt{2 * \pi * \frac{H_{i,m0}}{g * T_p^2}}} \tag{2.8}$$

In between the range of $8 < B/H_{s,i} < 12$ the Van der Meer et al. 2005 formulas are not defined and it is suggested to linearly interpolate for this region. As limits for the applicability of the formulas, Van der Meer et al. 2005 suggests a constant value of $K_t = 0.05$ for

the lower limit, while describing the upper limit with a linear dependency on the relative crest width $B/H_{s,i}$:

$$K_{tu} = -0.006 * \frac{B}{H_{s,i}} + 0.93 \tag{2.9}$$

Van der Meer et al. 2005 also looked at 3D experimental data, where he found no significant differences between waves approaching the breakwater obliquely or normal incident. Thus he concluded that the angle of incidence is of no importance for wave transmission.

SRINEASH AND MURALI FORMULATIONS

A rather recently developed relation regarding porous submerged breakwaters is described in Srineash and Murali 2019. In this study, empirical relations for transmission coefficient (K_t) and reflection coefficient (K_r) were designed via scaled physical modelling in a wave flume. The set-up was varied in crest width, depth of submergence and wave forcing (Srineash and Murali 2019). The authors proposed both relations for regular and irregular waves. The formula for irregular waves are given below:

$$\begin{aligned} K_{t,m0} = 8.6 * (0.71 * \tfrac{B}{L_{p,i}} * \tfrac{d_s}{H_{m0,i}})^{0.109} - 0.1 * (0.71 * \tfrac{d_s}{H_{m0,i}})^{1.04} - 3.5(\tfrac{d}{L_{p,i}})^{0.8} - \\ 4.45 * (0.71 * \tfrac{B}{H_{m0,i}})^{0.1} + 1.17(1 - \tfrac{d_s}{d})^{4.43} - 1.5(\tfrac{B}{L_{p,i}})^{0.46} \end{aligned} \tag{2.10}$$

$$K_{r,m0} = 3.4 * (0.71 * \frac{B}{L_{p,i}} * \frac{d_s}{H_{m0,i}})^{-0.024} - 4.3 * (\frac{d}{L_{p,i}})^{0.05} + 0.29 * (\frac{B}{L_{p,i}})^{0.85} + 0.44 * (\frac{d_s}{H_{m0,i}})^{1.04} \tag{2.11}$$

The applicability of the equations is suggested to be within a d/L range of 0.06–0.20 and a d_s/H range of 0.3–5.2, where d is defined as the water depth at the toe of the structure. The paper only mentions the bounds for regular waves, not for random waves. The relation for wave attenuation was compared to Van der Meer et al. 2005 and Seabrook and Hall 1998 and shows close proximity for conditions with smaller relative crest width but deviates for higher relative crest widths.

COMPARISON FORMULATIONS

All formulations were developed on typical trapezoidal breakwaters in flume experiments with random waves. Van der Meer et al. 2005 included the largest database by using data from more than 2300 tests. His formulation thus includes a larger variety of test setups. Both Van der Meer et al. 2005 and Seabrook and Hall 1998 based their formulations on tests including a wide sandy foreshore, leading to breaking not just on top, but also in front of the structure. Srineash and Murali 2019 does not mention if breaking occurs before the structure.

Only Seabrook and Hall 1998 gives a detailed description of how the processes of wave attenuation are represented in the used dimensionless numbers. The only parameter clearly defined in all formulations is $d_s/H_{m0,i}$, representing wave breaking and defined as the most important parameters by all authors. Using the Seabrook and Hall 1998 definition of the representation of dimensionless numbers, also the process of overtopping

is represented in all formulations due to the parameter $H_{i,m0}/B$, or an inverse of it. The nominal diameter of the the armor rock $D_{n50,a}$, which Seabrook and Hall 1998 uses to represent friction and flow within the structure are not present in the Van der Meer et al. 2005 or Srineash and Murali 2019 formulations. This means that their results are independent of the surface roughness and porosity of the structure. Van der Meer et al. 2005 incorporates the Iribarren number ξ, including information about the wave steepness and the breakwater angle α. This allows further information about the breaking capabilities of the incoming waves. Srineash and Murali 2019 incorporates several other dimensionless parameters, such as a different form of the relative width B/L_p. However, the processes which the author attributes to the used dimensionless numbers are not apparent from the paper.

2.3. WAVE ATTENUATION BY OYSTER REEFS

Oyster reefs offer a multitude of ecosystem services. Of special interest for coastal engineers are hereby their wave attenuation capabilities in coastal regions. To use this property, oysters have to be recruited at the location of interest. The conditions required for a healthy oyster reef to develop are out of the scope of this thesis but are described e.g. in Walles, Troost, et al. 2016. The used recruitment structures or substrate, however, are of interest since the existing shapes vary significantly which influences the performance of the oyster reefs in wave attenuation. Fundamental is hereby the provision of a hard substrate on which the oyster larvae can settle, and grow on. Often used techniques are the usage of concrete blocks, called oyster castles, or steel wire gabions, which are filled with substrate like shells. It should be noted that the used structures themselves already resemble breakwaters. The recruitment of oysters however can lead to an increase in surface roughness, and both vertical and horizontal growth, changing the geometry of the structure. Some used methods are visualised in figure 2.2.

Figure 2.2: Different artificial oyster reef structures in practice. tl: shell gabions used in the Netherlands (ecoshape.org), tr: OysterBreak™ (Wayfarer Environmental Technologies), bl: The Oyster Castle®(alliedconcrete.com), br: Oyster Reef Ball (reefinnovations.com)

The performance of such artificial oyster reefs in attenuating waves and reducing erosion was investigated in many field or laboratory tests, mainly in the USA. Most field studies focus hereby on the quantification of the erosion, with only a few studies investigating wave attenuation directly. The most relevant results found in literature are summarised

below.

Webb and Allen 2015 conducted scaled laboratory experiments using two types of artificial reef structures, namely triangular oyster gabions (ReefBLK) and concrete wave transmission frustums (WTFs), which are lines of pyramid-shaped oyster castles, investigating their wave attenuation capabilities. The tests were done with the structures only, having no oyster cover. Both structure types had a height of 0.3 m in the test, with a test scale of 1:5 for the WTFs and a scale of 1:2 for the Reef BLK. The results show a strong inverse relationship between the transmission coefficient K_t and the dimensionless parameter h_s/d, representing relative submergence or emergence, for both types. Additionally, the non-dimensionless length B/L_i is shown to play a secondary role. However, the influence of the wavelength on the wave transmission was found to be opposite for the two structure types, with a positive correlation between K_t and B/L_i for ReefBLK and a negative correlation for WTFs. An explanation was not given for this phenomenon. K_t values of lower than 0.5 only appear if the structure crest is above still water level, of which the conclusion was drawn that such structures are little effective if built-in subtidal environments. The authors compared the measurement results to the empirical formulations of Van der Meer et al. 2005, showing poor concordance. They attribute this to the shapes of the used oyster castles, which do not resemble a classical breakwater, which the Van der Meer et al. 2005 formulations are based on.

Wiberg et al. 2018 examined wave dissipation over four restored intertidal oyster reefs, constructed using different reef structure types in Ramshorn Bay, Virginia, USA. Three of the observed oyster reefs were constructed using a type of oyster castle, but one reef resembles the structure observed in this thesis. This reef was built with crushed whelk shells, showing gently sloping sides, a mean crest height of 0.7 m and a reef width of 3-5m. The reef is emerged 25 % of the time and the mean tidal range in the bay is 1.2-1.3 m. Mean incident wave height was recorded as H_s = 0.03 m while the maximum measured incident wave height was H_s = 0.38 m. The study quantified wave attenuation for this reef; for water depths between 0.5-1.0 m, waves attenuated by 48 ± 7 % , between 1.0-1.5 m by 20 ± 4% and for water depths higher 1.5 by 8 ± 4%. The authors concluded that the oyster reef proved effective in reducing wave energy in smaller, more frequent storms when the freeboard was below 0.75m. During larger storm events, however, when a storm surge increases the water depth, the reef proved less effective.

Chauvin 2018 conducted field experiments at 4 different locations with different concrete oyster castle types in Eloi Bay, Lousiana USA. The smallest observed structure had dimensions of 0.32 m in height and 2.6 m in width, while the largest structure had dimensions of 0.59 m in height and 4 m in width. The study area is characterised by a microtidal, and low energy environment, with a mean tidal range of 0.3 m and maximum recorded wave heights of 0.45 m. All four structure crests are located above mean sea level (MSL), with two structure crests located higher than mean higher high water (MHHW), only being fully submerged during some spring tides and extreme storm events. At the time of the study, all structures showed medium to no oyster recruitment. Chauvin 2018 quantified the wave attenuation by grouping the wave conditions into wa-

ter elevation ranges of 0.5 ft and relating the incident and transmitted wave heights with linear regression. He found significant wave height reductions for all four reefs during all observed conditions. Maximum mean transmission coefficients at the highest water elevation group were about $K_t = 0.6$ for the lower two reefs which had a maximum freeboard of 15 cm. For the highest reef with near-permanent emergence, the maximum transmission coefficient was $K_t = 0.4$.

Other researches did not measure wave dissipation directly, but rather an oyster reef's effect on erosion on adjacent tidal flats or marshes. Scyphers et al. 2011 found reduced shoreline retreat of up to 40 % for artificial constructed oyster breakwater reefs. La Peyre 2017 analysed marsh retreat at seven independent oyster reef restoration projects and found a lower retreat at all locations compared to reference transects. Moody et al. 2013 assessed shoreline loss at three different locations between 2009 and 2011. Artificial oyster reefs were established at each site and the adjacent marsh erosion compared to control sites. The authors found a significant reduction in shoreline loss for all three sites. They furthermore suggest that the effect of oyster reefs increases until it reaches maturity. Walles, Salvador de Paiva, et al. 2014 measured flat elevations around eleven natural oyster reefs to assess their effect on erosion. Behind all reefs, an elevation of >5 cm compared to adjacent areas could be measured. The affected area was determined to be of the same order of magnitude as the area of the oyster reef itself.

2.3.1. REFLECTION ON LITERATURE AND RELEVANCE FOR STUDY

In general, literature seems to show that oyster reefs are effective in reducing erosion, but can only stop retreat in few cases. This means that next to oyster reefs also other mitigation strategies have to be considered if structural erosion is to be halted. It should however be noted that most field research about oyster reefs is conducted in the US part of the Gulf of Mexico, where the tidal range is typically low (as in experiments of Chauvin 2018, Scyphers et al. 2011 and La Peyre 2017). Furthermore, concrete oyster castles seem to be the preferred recruitment structure in most studies. These often exhibit an irregular shape with gaps in between (see Oyster reef ball in figure 2.2), showing less resemblance to typical breakwaters than e.g. gabion oyster breakwaters which are used in this study. For these reasons, a comparison of the existing literature with oyster reef effects in a macrotidal environment and with different reef-building mechanisms should be made with care.

3

STUDY SITE

The oyster reef of interest is located in the Oosterschelde, Netherlands. In the following, a quick overview of the study area, present oyster populations and known tidal and wave forcing is given. Furthermore, information on the erosional trend, including newly acquired transect data is presented. Overall this section will answer question A defined in section 1.4.

3.1. OOSTERSCHELDE

The Oosterschelde is a macro tidal, semi-diurnal estuary located in the region of Zeeland, south of the Netherlands (see figure 3.2). In 1986 the estuary was semi-closed off as part of the Delta Plan, which was established after severe flooding in 1953. This turned the Oosterschelde into a 351 km^2 large tidal basin including 118 km^2 of tidal flats (Nienhuis and Smaal 1994). Under normal, low energy conditions, the barrier only semi closes off the basin, allowing for tidal flow through it. Only during storm conditions do the gates shut and create a fully closed basin (Bosboom and Stive 2015). The structure itself, however, permanently reduced the cross-sectional area at the mouth of the basin, changing the hydrodynamics by decreasing the tidal prism, the tidal range and the tidal currents(Bosboom and Stive 2015, Walles, Salvador de Paiva, et al. 2014). An overview of the current tidal range and flow velocities is given in figure 3.1.

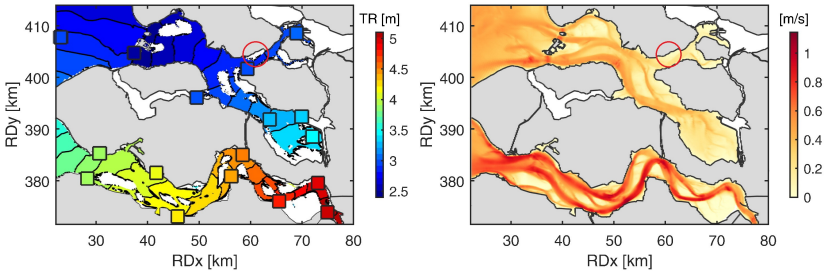

Figure 3.1: Tidal range (MHW-MLW) and depth averaged flow velocities in the Oosterschelde and Westerschelde. Derived from 1 month Deflt3D models. Study site is marked with a red circle. (Figure taken from: de Vet et al. 2017)

There is little freshwater inflow into the estuary, leading to high salinity of generally > 30 PSU (Troost 2009). Because of the reduced tidal prism and flow, the Oosterschelde is currently not in morphological equilibrium (Walles, Salvador de Paiva, et al. 2014). The channels are too deep and wide for the present flow characteristics and are consequently filling up with sediment eroding from the adjacent tidal flats (Walles, Salvador de Paiva, et al. 2014, Vriend et al. 2014). This has lead to structural erosion of the tidal flats with average erosion rates of 1 cm/y in height and a predicted 50 % area loss till 2100 (Ysebaert et al. 2019). With the disappearance of the tidal flats, also valuable services like wave dissipation or habitat function are at risk. As a response, the dutch directorate for public works and water management, Rijkwaterstaat, is investigating the usage of oyster reefs and sediment nourishments to conserve the tidal flats.

Figure 3.2: Map of Zeeland and the Oosterschelde. (Google Earth Pro 7.3.3 2020)

Originally, the native European flat oyster Ostrea Edulis was the dominant oyster species in the Oosterschelde. However, this changed in the aftermath of a mass mortality event in 1963 (Drinkward 1998). To find more robust alternatives, the local fishers introduced a new species in 1964, the Crassostrea gigas (or pacific oyster), originating from British Columbia (Drinkward 1998). Soon after, also natural recruitment was recorded (Drinkward 1998), after which C. giga spread rapidly throughout the estuary (Walles, Salvador de Paiva, et al. 2014), quickly making it the dominant species in the region. The unexpected success of the invasive species in naturally spreading across the coast can be traced back to a lack of natural predators and low vulnerability to disease and parasites compared to the native counterpart (Troost 2009). Most of the new, naturally built reefs, are furthermore not fished and are largely left undisturbed (Kater and Baars 2004), leading to the existence of stable reefs with well over 30 years of lifetime (Walles, Mann, et al. 2015).

As of 2005 close to 7 % (8 km^2) of intertidal areas were covered by oysters, showing an increasing trend (Smaal et al. 2009, Kater and Baars 2004).

3.2. REEF AT THE VIANE TIDAL FLAT

Within the framework of the 'Biobouwers project' and the 'Building with Nature' program, the concept of artificial shellfish reefs for erosion management was first researched in the Netherlands (ecoshape 2021). After some small scale pilots in 2009, 3 large scale artificial oyster reefs were constructed on eroding intertidal flats, using C. gigas in the Oosterschelde in 2010, two at the intertidal flat of Viane (VianeEast and VianeWest) and one at De Val (Walles, Troost, et al. 2016). The reefs were constructed using 25 cm high steel wire gabions, which were filled with dead oyster shells on which oyster spat could attach (Ysebaert et al. 2019). Of the three reefs, only the reef VianeWest developed into a fully self-sustaining and growing reef, while VianeEast is showing no live oysters and De Val is suffering from low recruitment, which is likely the result of a too long immersion time (Walles, Troost, et al. 2016). To capture the effect of live oysters, the measurements for this thesis were thus only conducted at the reef VianeWest, which is located at 51°36'38.64"N, 4° 1'26.44"E, as shown in figure 3.3.

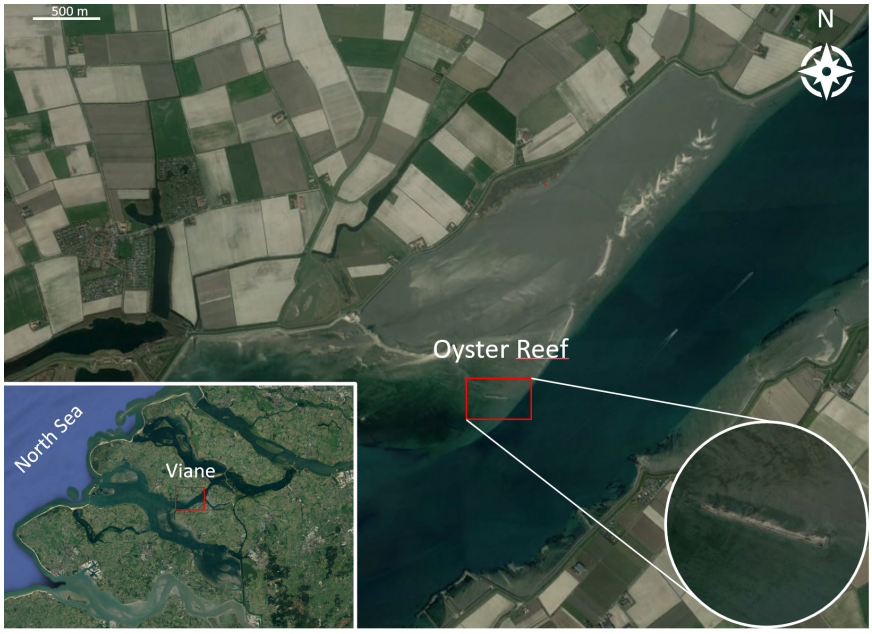

Figure 3.3: Study-area in the Oosterschelde basin, Netherlands: VianeWest. (Google Earth Pro 7.3.3 2020)

After construction, the reef dimensions were initially defined by the used shell filled gabions. These built a reef measuring 204 m in length, 8 m in width and 0.25 m in height (Walles, Troost, et al. 2016). However, oyster growth changed the width and the height

of the structure, with the new dimensions determined in a reef survey, laid out in section 3.2.2. The orientation of the reef was defined in WNW / ESE direction, with a 20 ° tilt compared to WE direction (see figure 3.3) (Walles, Troost, et al. 2016). This orientates the reef perpendicular to the dominant wind direction, which approaches the reef from SSW. In relation to the mean sea level (MSL) the reef is located at 0.96 ± 0.03 m MSL, leading to an average emersion time per low tide of 23 ± 1.5 % (Walles, Troost, et al. 2016).

The reef can generally be characterised as healthy, with sufficient oyster recruitment to self sustain it (Walles, Troost, et al. 2016). The oysters on the reef have lengths of ~ 10 cm (Walles, Troost, et al. 2016, own observations), with large specimens reaching over 20 cm of length (own observations). The density of the oyster population varies over the width of the reef. At the front of the reef, on a width of about 4 meters, the oyster population is built very densely. After 4 meters, areas with no oyster growth exist at some parts of the reef. At some locations, the reef furthermore expanded its width considerably landwards. These locations are generally characterised by a lower elevation than the front part of the reef and by a less dense oyster population (see figure 3.4).

Figure 3.4: Oyster reef Viane West. Visible is continuous dense oyster growth on the first 4 meters and areas with no growth behind. (Picture taken on 03.02.2021)

Statistical wind data was obtained from the station at Stavenisee. Wind direction is coming predominately from SW direction (figure3.5). Since the flat is in an enclosed bay, only locally generated wind waves are to be expected, which is why the wind likely aligns with the dominant wave direction. The fetch in this direction is relatively small at 2.5 km.

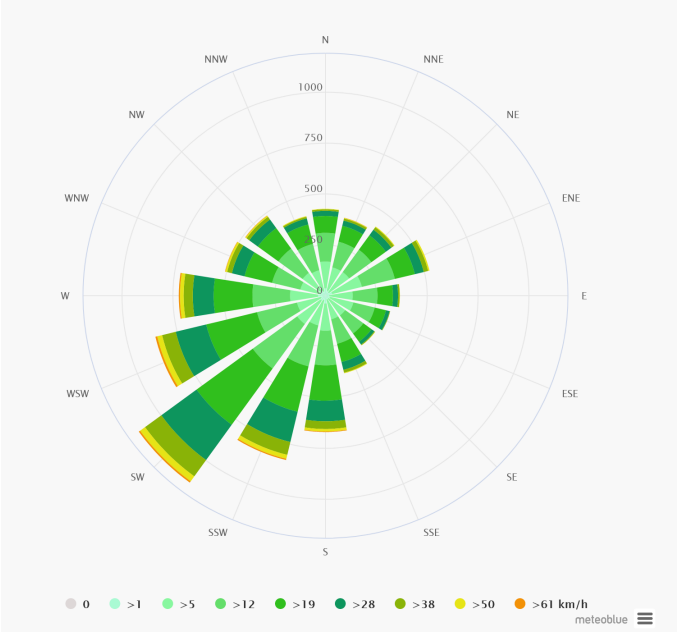

Figure 3.5: Windrose at Stavinesse *Climate Stavenisse* 2021

3.2.1. EROSIONAL TREND

After the Delta Plan changed the hydrodynamics of the Oosterschelde, the adjacent intertidal flats in the basin started to erode. To keep track of the erosion quantities, the dutch Directorate for Public Works and Water Management, Rijkwaterstaat, started collecting elevation data of the intertidal flats. Such data is important to assess the current erosional trend of the flat, which can be used to indicate the effect of counter measurements and the potential necessity of further action. For the present intertidal flat Viane, such transect measurement were collected from 1988 to 2021 (see figure 3.6). These show elevation losses of up to one meter since 1988. While erosion can still be observed on the entirety of the transect, erosion did slow down, currently reaching values of around 1 to 3 cm/y on the shown transect.

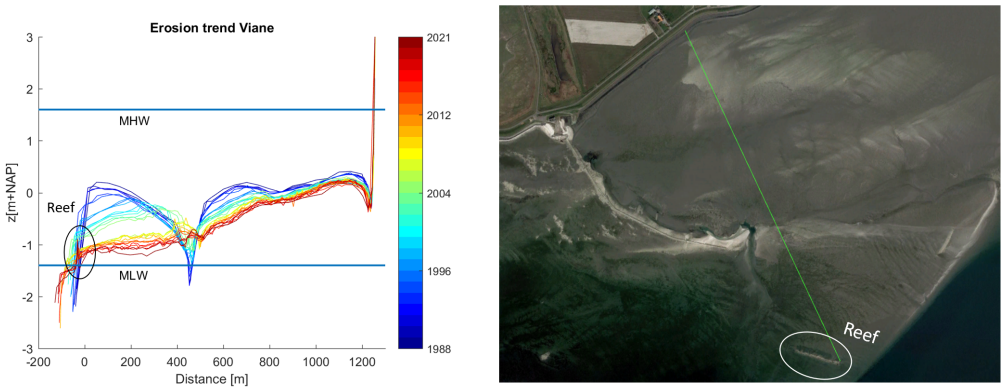

Figure 3.6: Transect Data intertidal flat at Viane. The oyster reef is located at x = 0 m (see circle). Transect data was collected yearly with gaps only in between 2003 -2008 and 2017-2021. ((l)de Vet et al. 2017, *Rijkwaterstaat* 2021, (r) Google Earth Pro 7.3.3 2020)

Only the elevation data in between x = -50-200 m is directly influenced by the oyster reef since this section is located directly behind the reef. After the construction of the reef in 2010, a reduction of the erosional trend in this area can be seen compared to the area at x = 200 - 350 m, which showed equal erosion rates prior to 2010. This indicates a reducing effect of the oyster reef directly behind it. However, also other effects may play a role and further investigation of the actual contribution of the reef to this effect is not within the scope of this thesis.

3.2.2. REEF SURVEY

To get a better idea of the current dimensions of the reef, new GPS measurements on several transects were conducted (see figure 3.7). These transects capture the variability of the reef crest height over its length and width differences due to irregular oyster growth.

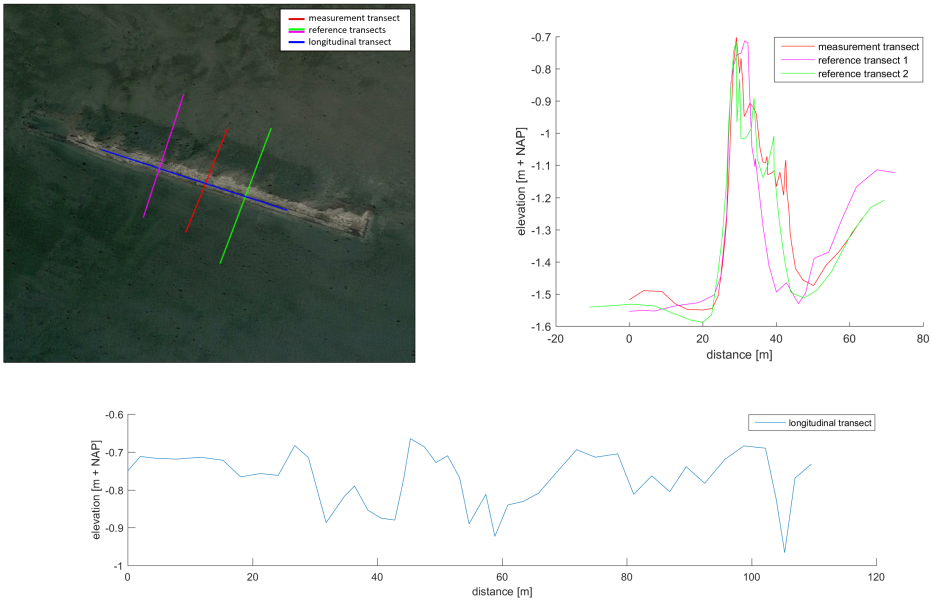

Figure 3.7: Reef-transects taken during measurement campaign.(tl) location of taken transects,(tr) reef-normal transects, (b) longitudinal elevation

On the measurement transect, the reef exhibits a width of approximately 20 m and a crest height h_s of 0.8 m compared to the bed in front of the reef. The crest height is hereby measured until the tip of the oysters which covers the structure. However, the transects show that the spacial reef dimensions are quite inhomogeneous and change substantially. Crest height differences can reach up to 0.2 meters over the reef length, while the reef width varies from about 8 m, which was the original oyster gabion width, to 20m. Wave approaching the reef on an angle might thus experience different reef dimensions. It is furthermore visible, that the elevation of the reef varies significantly over its width, with the highest crest elevation only present over a small width at the front of the reef. Towards the back of the reef, the elevation reduces quickly, reaching about only half of the highest crest elevation.

3.2.3. PAST DATA SETS

Within the context of the Emergo 2021 project, long term pressure data was collected in front of the reef in 2017. Wave characteristics are thus known in front of the reef and summarized in figure 3.8. Since the tidal flat is located in an enclosed area no swell energy is measurable as shown in the sample 10 minute spectrum above. Furthermore, a maximum H_s/d ratio of approximately 0.42 can be estimated from the data, which can likely be lead back to wave breaking. Significant wave heights do not exceed 1 m and maximum peak periods are around 5.5 s.

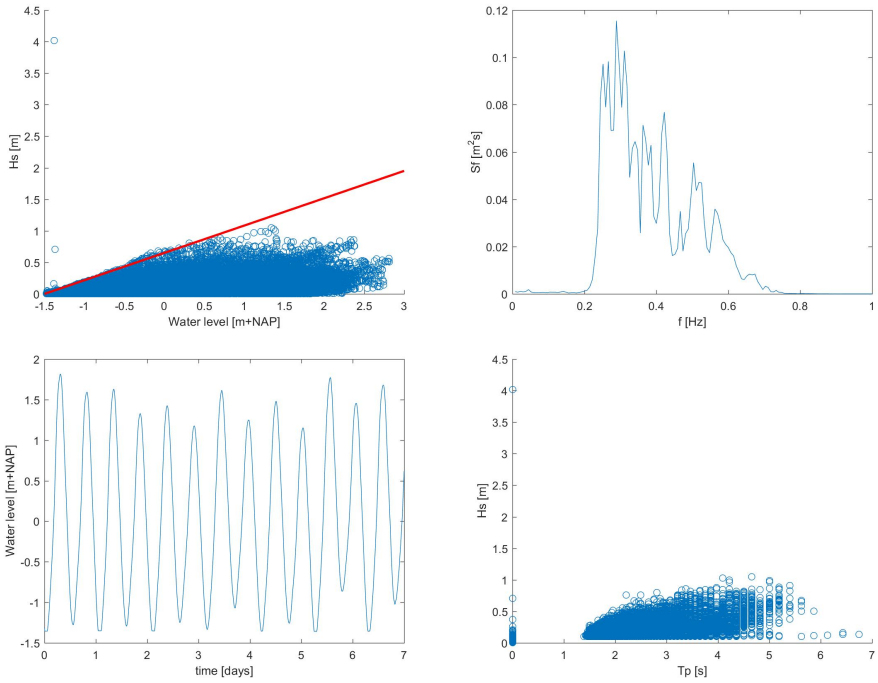

Figure 3.8: Past wave data set at Viane. Collected at at 51.61073, 4.02300: (tl) H_s/d ratio; (tr)typical 10 minute spectrum at energetic conditions (Hs = 53 cm / Tp = 3.4 s); (bl) typical tidal characteristic; (br) wave characteristics de Vet 2020

Shortly after the oyster reefs at Viane were constructed in 2010 and before oysters could settle an intensive measurement campaign including pressure sensors, ADCPs, OBSs and LISST instruments was conducted by Deltares. The resulting data was analysed and processed within a master thesis (Dorsch 2012). For the reef at Viane west, a regime plot was created showing the conditionality of wave attenuation over the reef (figure 3.9)

Viane West

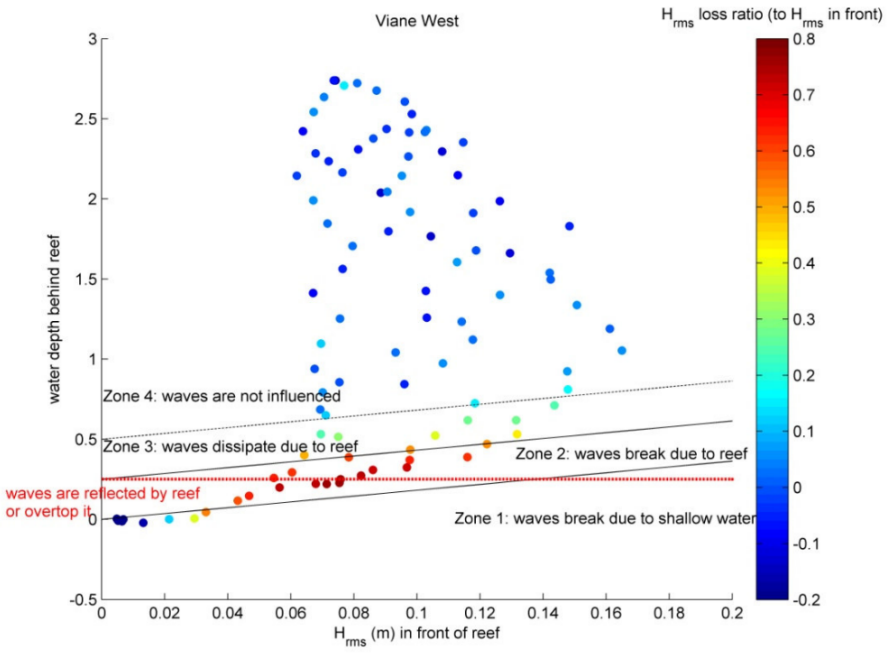

Figure 3.9: Conditionality of wave attenuation. Measured over the oyster gabion VianeWest as a function of water depth and wave height Dorsch 2012

The findings in figure 3.9 should be treated with care though since the measurement period only consisted of one day, with no captured storm conditions. Furthermore, the measurement campaign had to deal with instrument problems and incomplete data sets which is why a reanalysis of the data for this thesis was not successful. Nevertheless, the above results could prove sufficient for the analysis of the added value of live oysters on the gabion structure.

4

FIELDPLAN

To fulfil the first research objective, a field campaign was conducted at the research site. In the following first the general outline of the field plan is given. Then the used measurement systems and their employment is described. The collected data set is freely available via DOI: 10.4121/14916612.

4.1. OUTLINE OF FIELD PLAN

A variety of pressure sensors, acoustic doppler velocimeters (ADVs) and acoustic doppler current profilers (ADCPs) was used to collect the necessary pressure and velocity data at 7 locations (ML_1-ML_7) at and around the reef. The focus lies hereby on the pressure measurements, with which a detailed wave analysis can be conducted. The first campaign, where instruments were deployed, was conducted on the 16.12.2020. ADVs and ADCPs were then retrieved 1.5 months later on the 03.02.2021. On the 12.02.2021 the remaining OSSIs were retrieved, earlier than planned because of cold temperature. In figure 4.1 and figure 4.2 the outline of the measurement plan with measuring heights and locations are laid out. In case of the OSSIs, the depicted heights give the distance between bed and sensor point, for the ADCP the height until the centre of the first cell and for the ADVs the height until the measurement point (15 cm from the probe). Furthermore, the elevation of the reef at the different measurement locations is given. In table 4.1 the used numeration for the instruments is listed next to other relevant information. Specs and settings for each used measurement device as well as the reasoning for the outline are summarised in the following sections.

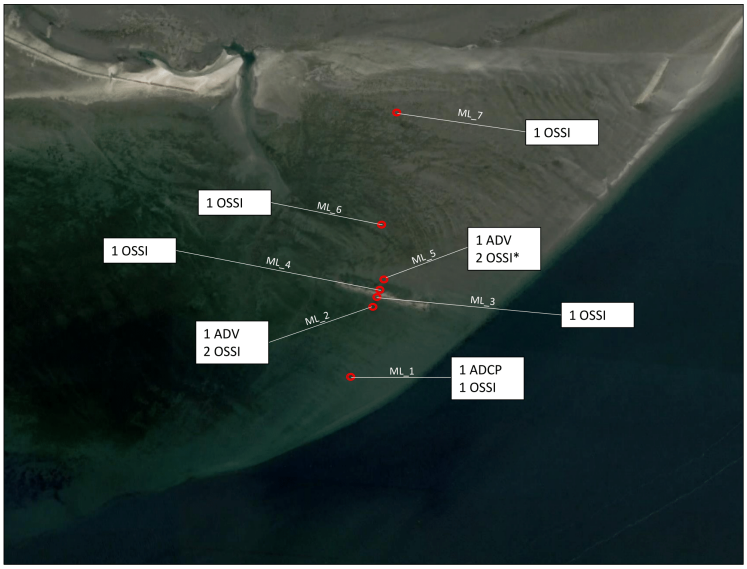

Figure 4.1: Location of the deployed measurement systems on the intertidal flat

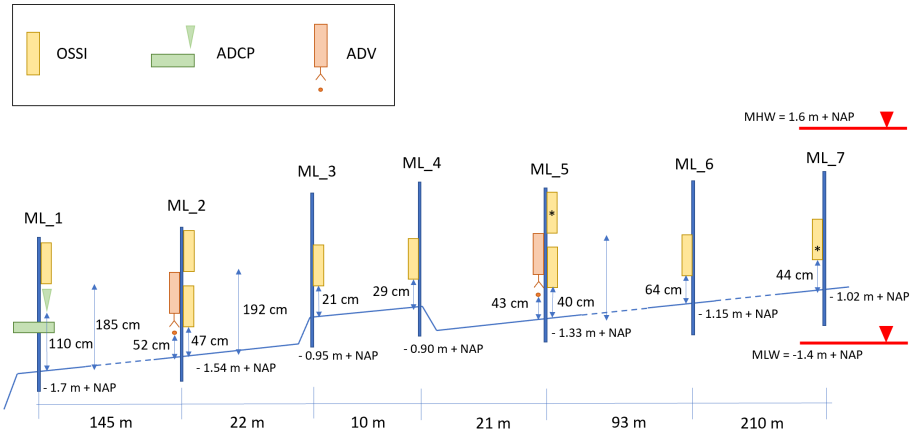

Figure 4.2: Detailed outline of measurement plan. Depicted are measurement height, flat elevation (NAP), distances between measurement locations and mean high water (MHW) as well as mean low water (MLW). Distances and elevations are not depicted to scale.

Measurement device	sample rate [Hz]	flat elevation [m NAP]	measuring length [days]	Location [°]
$OSSI\_ML_{1,top}$	-	-	faulty data	51.60932, 4.02306
$OSSI\_ML_{2,top}$	10	-1.54	41	51.61057, 4.02371
$OSSI\_ML_{2,bottom}$	10	-1.54	57	51.61057, 4.02364
$OSSI\_ML_3$	10	-0.90	42	51.61074, 4.02384
$OSSI\_ML_4$	10	-1.15	49	51.61082, 4.02385
$OSSI\_ML_5$	10	-1.33	57	51.61100, 4.02390
$OSSI\_ML_6$	10	-1.15	57	51.61184, 4.02392
$OSSI\_ML_7$	10	-1.02	41	51.61372, 4.02416
$ADCP\_ML_1$	8*	-1.7	47	51.60932, 4.02309
ADV_ML_2	8*	-1.54	33	51.61057, 4.02365
ADV_ML_5	8*	-1.33	33	51.61100, 4.02393

Table 4.1: List of measurement devices and deployment length. Measurement length depends on battery life.
* ADVs and ADCP measured in 15 minute bursts every 30 minutes at 8 Hz.

4.2. PRESSURE MEASUREMENTS

GENERAL INFORMATION

Pressure measurements can be used to obtain wave statistics at point locations. Thus these measurements were conducted at all measurement locations (ML_1-ML_7), which form a transect in the dominant wave direction perpendicular to the reef. This allows the monitoring of the wave trajectory over the flat and reef. Measurement location 1 (ML_1) is located at the fringe of the tidal flat where incoming waves are largely unchanged from bottom interactions. This data point thus represents the incoming forcing at the boundary of the system. The point can furthermore be used to quantify bottom effects on the waves up until the reef. The devices at ML_2 and ML_5 are located 22m and 21m in front and behind the reef respectively, and their measurements can be used to determine dissipation by the entire reef geometry. Dissipation right on top of the reef can be measured by the pressure gauges set up at locations ML_3 and ML_4, just on the edges of the reef. These can be used to measure the effect of friction if no breaking occurs. ML_6 and ML_7 were set up to quantify dissipation behind the reef. At all locations pressure was measured close to the bed, to have maximum submergence, and thus measurement time. Some higher located OSSIs were placed to get more reliable data at high water depths and high-frequency waves, but their usage was ultimately discarded because of instrument failure.

TYPE OF INSTRUMENT, SETTINGS AND MOUNTING

For the pressure measurements, mostly instruments of the type OSSI-010-003C-03, produced by Ocean Sensor Systems (*ocean sensors* 2021) were used. This is a submersible, self logging and self-powering pressure sensor, which can detect a pressure range of up to 3 bar. In addition, the Aquadopp Profiler (further described below) measured pressure at ML_1. For the deployment, the OSSIs were mounted on metal poles which were driven into the ground (see figure 4.3). During deployment, all OSSIs measured continuously with a sample rate of 10 Hz. The ADCP collected pressure data with a sample rate of 8 Hz and 15-minute bursts every 30 minutes. For the nomenclature, simply the position of the devices is used ($OSSI\_ML_1$ etc.). The location of the instruments and measurement height with respect to bed level was measured with a portable GPS system. The technical

sheet and used instrument settings can be found in appendix A.1.

Figure 4.3: Mounting of high OSSIs (l) and low OSSIs (r), taken on 03.02.2021

4.3. ACOUSTIC DOPPLER CURRENT PROFILER

GENERAL INFORMATION

An acoustic Doppler current profiler or ADCP can measure velocity profiles over a water column. The instrument operates by sending out acoustic waves in specific frequencies. These waves reflect from suspended particles and are detected again by the instrument. The hereby measured travel-time can be used to calculate distance, while frequency shifts, called Doppler shifts, are proportional to the particle velocity. An ADCP was placed on the fringe of the reef at ML_1 to get a detailed idea about the undisturbed incoming wave characteristics. For this thesis mainly the wave direction and pressure measurements are relevant. However, the full data can provide accurate boundary data needed for a numerical model, which is planned to be developed in the future.

TYPE OF INSTRUMENT, SETTINGS AND MOUNTING

The used ADCP is a 1 MHz Aquadopp profiler from Nortek (*Nortek* 2021). The instrument was pointed upward and mounted to a stiff metal frame as shown in figure 4.4. Velocity was measured in 7 cells of 10 cm each. The blanking distance from the instrument head is 10.4 cm. Measurements were taken with a sampling frequency of 8 Hz in 15 minutes intervals every 30 minutes. The battery life was extended using an additional external battery that was strapped to the frame. This enabled a measurement time of 47 full days. The technical sheet and a file with all detailed user-defined settings can be found in appendix A.1.

Figure 4.4: ADCP frame with external battery canister. Taken on 03.02.2021

4.4. ACOUSTIC DOPPLER VELOCIMETER

GENERAL INFORMATION

An Acoustic Doppler Velocimeter or ADV measures velocities at a single point, typically in relatively high frequency. It does so using the Doppler shift, scanning for frequency changes in an acoustic signal. The device sends out an acoustic wave with a specific frequency from a transmitter. This wave is then reflected from moving particles in the water. The reflected signal is measured by three receivers and analysed for frequency changes, which can then be used to calculate velocities in X, Y and Z directions. Typically the instrument has an indicated main axis, from which the retrieved X, Y, Z data can be transformed to an ENU fram

ADVs were used in front and behind the reef at ML_2 and ML_5 to get an idea about the directional spectrum of the waves. The aim is to find out if incident wave direction influences attenuation. Furthermore, the presence of currents and the extend of reflection can be studied.

TYPE OF INSTRUMENT, SETTINGS AND MOUNTING

Vector - 300 instruments manufactured by Nortek were used (*Nortek* 2021). The instruments were mounted to metal frames using two vertical and two horizontal poles (see figure 4.5). Special care was taken to build the frames as stiff as possible to prevent vibration and swinging during wave action. The frames were furthermore built perpendicular to the dominant wave direction, ensuring that the measured velocities were disturbed as little as possible by them. The measurements were conducted in 15-minute bursts every 30 minutes with a sampling frequency of 8 Hz. The sampling volume is located 15 cm away from the probe. To increase the possible deployment length additional battery

canisters were used. This enabled measurements for 33 full days. The technical sheet and a generated file showing all user-defined settings are attached in appendix A.1.

Figure 4.5: ADV frame and additional external battery canister. Taken on 03.02.2021

5

WAVE ANALYSIS

To obtain information about the attenuation capabilities of the observed oyster reef a wave analysis had to be performed. This was done using a spectral analysis on the collected pressure data at the seven measurement locations on the measurement transect. The steps taken to perform such an analysis are laid out below on the example of the $OSSI\_ML_{2,bottom}$ pressure measurements. All other pressure measurements are processed similarly. The wave direction was calculated from the acoustic doppler velocimeters. Wave asymmetry was calculated using the detrended pressure measurements. Lastly, the filter criteria for spectral quality and wave direction are explained, which ensure a high-quality data set. The quality of the raw data is validated in appendix A.4.

5.1. SPECTRAL WAVE PARAMETERS

5.1.1. DATA PREPARATION

The measured pressure readings were corrected for atmospheric pressure so that readings during instrument emergence have a constant value of zero bar. Additionally, the internal clock readings were compared to account for individual clock offsets. These practices are described in detail in appendix A.2. The resulting pressure readings can be transformed into uncorrected water depths above the sensor point using the equation:

$$d = \frac{P}{g * \rho} \tag{5.1}$$

where d is the uncorrected water depth above the sensor [m], P the pressure [Pa], g the gravitational acceleration m/s^2 and rho the water density $[kg/m^3]$. It should be noted that the uncorrected water depths neglect non-hydrostatic effects such as wave-induced pressure attenuation. Thus real water depths can only be obtained by averaging over a period of time. The water density was chosen as 1025 kg/m^3, considering the salinity of > 30 PSU and a water temperature of mostly around 5 °C (Engineering ToolBox 2005). Finally, the data sets were divided into 15-minute time series of 9000 data points each. To account for tidal changes the time series were detrended. For $OSSI\_ML_{5,bottom}$ this results in 5568 time-series to be analysed. These 15 minute time series of uncorrected water depths serve as the input for the spectral analysis which is explained in the chapter

below. The output parameters used in the analysis for this thesis thus always correspond to a 15 minute time period.

5.1.2. SPECTRAL ANALYSIS

The resulting uncorrected 15 minute water depth time series were processed using a MATLAB (MATLAB 2015) toolbox from Neumeir (Neumeir, Urs 2006). This toolbox is capable of computing the standard non-dimensional wave parameters using the spectral analysis or zero-crossing method, under the assumption of the linear wave theory. The application of these methods is extensively explained in literature, for example in (Karimpour and Chen 2017). In shallow water, the zero-crossing method can lead to errors due to low-frequency motions (Mouragues et al. 2019) which is why spectral analysis was used for the present data set. This method uses a Fast Fourier Transformation (FFT) to transform the 15 minute pressure time series into the frequency domain. A wave energy spectrum can then be estimated from the measured dynamic pressure power spectral density (S_{PP}) or the uncorrected water surface elevation power spectral density $S_{\eta_{uncorr}\eta_{uncorr}}$, depending on if the FFT was performed on the pressure readings or the derived uncorrected water depths (Karimpour and Chen 2017):

$$S_{\eta\eta} = \frac{1}{K_p^2} * S_{\eta_{uncorr}\eta_{uncorr}} = \frac{1}{K_p^2} * \frac{S_{PP}}{\rho^2 * g^2} \tag{5.2}$$

$$K_p(f) = \frac{cosh(k * h_p)}{cosh(k * d)} \tag{5.3}$$

Where $S_{\eta\eta}$(Karimpour and Chen 2017) is the water surface elevation power spectral density from which the standard wave properties can be obtained, K_p is the pressure response factor, k the wavenumber, h_p the sensor height above the bed and d the mean water depth. The pressure response factor K_p is used to account for the attenuation of the wave-induced dynamic pressure with depth in the water column and is derived from linear wave theory. Without this correction the spectral density would be calculated with the attenuated dynamic pressure readings, leading to an underestimation of the wave energy. As shown in equation 5.1, this attenuation, and thus the correction, is dependent on the wavelength and the elevation of the measurement point in the water column.

From the derived corrected spectrum $S_{\eta\eta}$ the the spectral wave properties can be calculated as:

$$m_0 = \int_0^\infty S_{\eta\eta}(f)\,df \tag{5.4}$$

$$H_{m0} = 4\sqrt[2]{m_0} \tag{5.5}$$

$$T_p = 1/f_p \tag{5.6}$$

Where m_0 is the zeroth moment of the energy spectrum, H_{m0} the spectral wave height, f_p the peak frequency and T_p the peak period.

5.2. WAVE DIRECTION

The incident wave directions were calculated using the ADV at measurement location ML2. Furthermore, wind data collected at the weather station Stavenisse, which is located across the channel, was used to estimate wave direction, since the ADV's measured during only part of the campaign. Wind data can be used to estimate wave direction since no swell waves are to be expected at the measurement location.

The ADV velocity data was first filtered for quality using the correlation and Signal-to-Noise-Ratio (SNR) given by the instrument. Low correlation values hereby mean that the three beams measure very different velocities, leading to unreliable averages. Low signal to noise ratios on the other hand means that the recorded velocity is of a similar magnitude as the instrument noise. As thresholds for the correlation values of > 80, with correlations between the three beams not differing for more than three, were used. For the SNR the threshold for usage was SNR > 10.

To calculate the wave direction the filtered ADV data set was split into 15-minute time series. Then the energy-weighted mean angle and the energy-weighted directional spread were calculated for each time series using the (u,v) velocity covariance matrix. This process is described in Herbers et al. 1999 and Henderson et al. 2006. Finally, the angles were translated to refer to a northeast reference system.

5.3. WAVE ASYMMETRY

Wave asymmetry was calculated using the detrended 15 minute pressure time series. This was done using a Hilbert transformation to return the analytical signal of the data. The used Matlab code is given in appendix A.3.

5.4. DATA FILTERING

The macrotidal environment of the study site can lead to quality problems of the data, when the wave-induced pressure attenuates too much before reaching the pressure sensors, especially during high water levels and low energy waves. Furthermore, it has to be ensured that only waves which crossed the reef are part of the analysis. The root of these problems and how they were treated in this theses are explained in the following. Hereby the side question B, mentioned in section 1.4 is answered.

5.4.1. SPECTRA QUALITY

The method using K_p to account for the attenuation of the wave-induced dynamic pressure can lead to an overestimation of the energy contained in the high-frequency part of the spectrum. This is indicated in figure 5.1 which shows the evolution of K_p with increasing water depths.

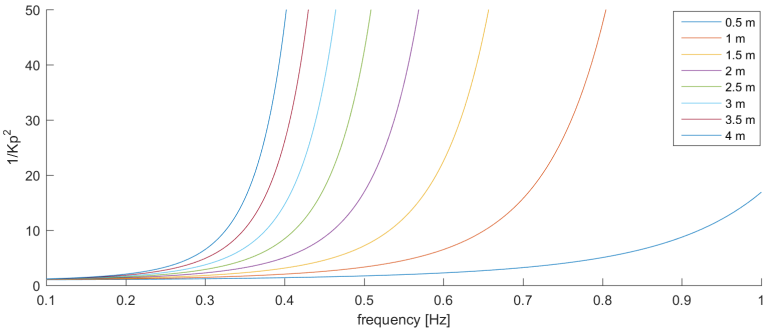

Figure 5.1: Schematic evolution of the correction factor $1/Kp^2$ at different water depths. h_p is assumed to be 0 (waves measured at bed).

5

From figure 5.1 it is clear that the correction factor $1/K_p^2$ increases exponentially in the high-frequency range, with the increase happening at lower frequencies if the water depth is high. This is not a problem if the main body of the spectra and the exponential increase can be easily distinguished, meaning that the exponential increase affects the spectra only well behind the peak frequency. For high water depths and short waves, however, the exponential increase can start close to the peak of the spectrum, severely altering its shape (see figure 5.2). This phenomena and prevention methods are explained extensively in literature, for example in Karimpour and Chen 2017.

The Neumeir, Urs 2006 tool includes two measures to deal with this exponential increase. Firstly, to limit the maximum value of $1/K_p^2$ a high cut off frequency f_c can be chosen, above which the spectra are removed and replaced with an estimated empirical diagnostic tail. This f_c has to be chosen with care, since the derived wave characteristics can react very sensitive to this choice of f_c, especially with waves in high-frequency range where substantial wave energy is located close to f_c. Yet no widely accepted method is available to determine the cut off frequency. In field applications, the range of f_c is typically between 0.25 and 0.6 Hz, but otherwise values observed in literature often seem arbitrarily chosen and poorly motivated (Mouragues et al. 2019). For this study, a maximum value of $f_c = 0.6Hz$ is not feasible, since the study site is in a macrotidal, low energy environment with low fetch and no swell energy, leading to a large variety of spectra with some peak frequencies at or above 0.6 Hz. To be able to also analyse the spectra located in this high-frequency range, a cutoff frequency of 1.2 Hz was chosen. After this value the correction factor $1/K_p^2$ decreases linearly (Neumeir, Urs 2006).

However, this high cut off frequency allows for an exponential increase at frequencies smaller than 1.2, which inevitably happen for high water levels during high tide. To prevent this, a second measure is applied, restricting $1/K_p$ to a maximum value of 10. This suppresses the exponential increase and ensures a smooth looking spectra tail.

Both these measures ensure smooth looking spectra. However, these can still contain

inaccuracies if one of the following conditions apply:

- The exponential increase might happen before the condition $1/K_p = 10$ is applied, leading to an overestimation of the wave energy.
- The condition $1/K_p = 10$ could apply before the peak frequency of the spectra, leading to a suppression of the actual energy and a shift of the peak frequency to lower frequencies, resulting in an underestimation of the wave energy.

The presence of neither of these cases can be determined directly since the applied conditions ensure a correct looking, yet faulty spectrum. Much of the data during low energy and simultaneous high water conditions is likely to fall in one of these cases, which is why it is desirable to discard these spectra. This was done by comparing the spectra calculated as described above, with the two measures preventing exponential growth, and the spectra calculated without such measures, allowing for exponential growth. If the exponential growth starts close to the peak frequency of the spectrum, it should not be used without adaptation.

All spectra were run through an automatic screening process to see if this is the case. A simple condition was applied, comparing the spectral density at the peak frequency and the spectral density at the initiation point of the exponential increase, which is indicated by the minimum spectral density found between the peak frequency f_p and $f_c = 1.2$. To reduce the impact of peaks on this process the spectra were smoothed out with a weighted average between 10 consecutive values. With this comparison, the spectra can then be sorted into quality groups.

The first group contains spectra with little confidence in accuracy and are directly discarded, the second group contains spectra with high confidence until the peak period, but low confidence in the high-frequency tail and the third group contains spectra that have high confidence overall. The conditions are explained in table 5.1. Furthermore, another condition was set regarding the water level. Even if the still water level is above the measurement point, the wave motion can still lead to some emergence time in wave troughs. This results in faulty spectra. To ensure that the devices are fully inundated at all times only spectra during water levels higher than $0.5 * H_s$ above measurement height h_m are considered.

Group:	condition:	result:	Nr of time series:
1	$min(Spec_{nofc})$ >$0.5Spec_{fc}(f_p)$	spectra discarded	825
3	$0.25Spec_{fc}(f_p)$ <$min(Spec_{nofc}*)$ <$0.5Spec_{fc}(f_p)$	spectra used until f_p	783
4	$min(Spec_{nofc}*)$ <$0.25Spec_{fc}(f_p)$	spectra fully used	2540
2	d <$h_m + 0.5H_s$	spectra discarded	1420

Table 5.1: applied conditions to filter the used spectras

The application of this conditional separation is visualised for further understanding in figure 5.2. These two spectra show how the confidence of the used spectra changes for similar wave heights $H_{m0,i}$ but varying water levels.

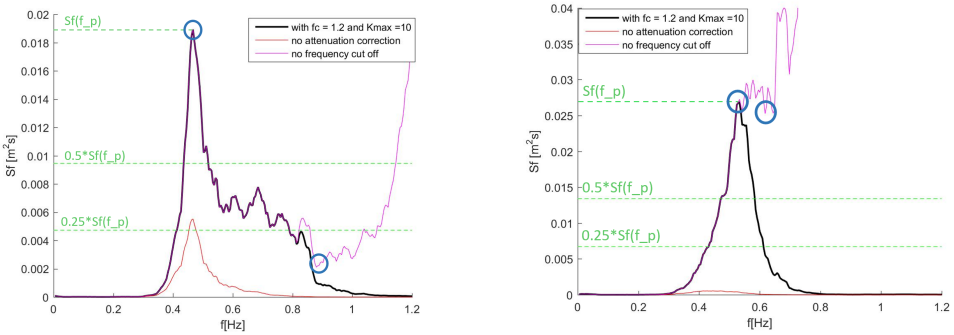

Figure 5.2: Visualization of criteria to filter spectra. Uncorrected spectra (red), corrected spectra with applied cut of frequency and K_p limit (black), corrected spectra with no applied cut of frequency and K_p limit (pink). Blue circles indicate the points where the conditions are checked. left: wave heigth H_s = 0.24 m, water elevation d = 1.35 m; right: wave heigth H_s = 0.24 m, water elevation d = 2.40 m

As shown in table 5.1 2540 spectra taken at ML_2, representing 45 % of all spectra fulfil the condition to be fully used under the given cut off frequency while 783 spectra representing 14 % of all spectra can be used up until the peak frequency f_p.

Figure 5.3 shows the conditionality of the sorting process with respect to water depth and peak period at ML2. Visible is that the discarded data plotted in green falls in the region of low peak periods and high water depths. This was to be expected since in this range only little wave energy reaches the sensors due to pressure attenuation, making it difficult to differentiate between the wave signal and noise. If only little energy reaches the sensor, of course even less energy reaches the bed, making the discarded data of little value for this analysis, since ultimately the effect of the waves on flat erosion is of interest. The data discarded because of water level plotted in blue corresponds to conditions with water elevations below the oyster reef crest elevation. During these conditions, a transmission coefficient of nearly zero can be expected which is why this data is of minor interest for this analysis too. The data of group 3, considered as fully usable and plotted in black covers the entire spectrum of present wave conditions in a sufficient sample size. This group furthermore contains the majority of high energy spectra, which are of special interest for this study. Because of the large quantity of spectra that can be fully used, no use was made of the spectra in group 2.

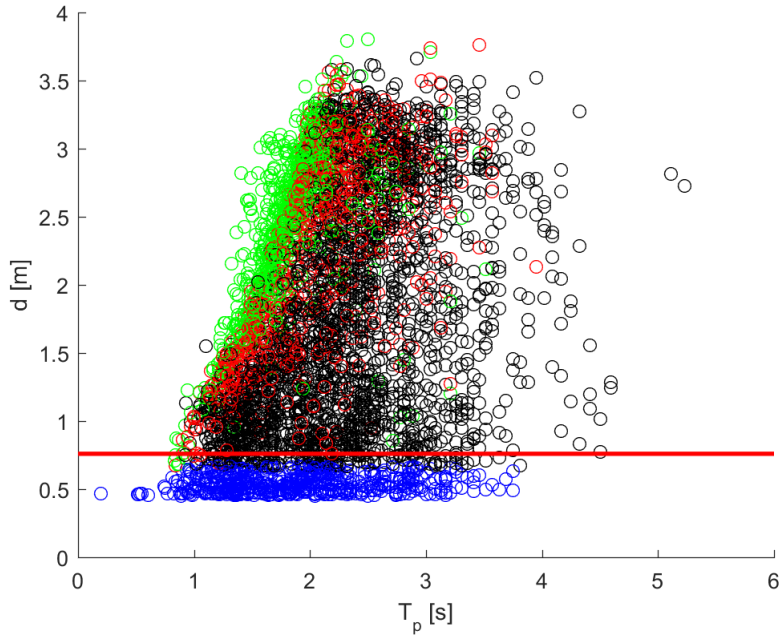

Figure 5.3: Conditionality of sorting process with respect to water depth and peak period at ML2

5.4.2. INCIDENT WAVE DIRECTION

A wide range of wave angles was found during the measurement period. For the upcoming analysis, only waves that approached the reef from the seaside, and passed both the reef and the observed measurement devices, are relevant. This ensures that the measurement devices landward of the reef actually measure waves that were attenuated by the reef. The further away a measurement location, the narrower the range of usable wave direction hereby is. Thus, different criteria were used for the devices at $ML1 - ML5$ and $ML6$. No criteria are given for ML7 since the directional spread of the waves will make waves that passed, or bypassed the reef indistinguishable. The criteria are given in table 5.2. It should be noted that wind direction is typically defined as the direction where the wind is coming from while wave direction is typically defined as the direction in which the waves propagate.

ML	available data	wind criteria	wave criteria
ML1 to ML5	wind and wave	90°-300°	300°-80°
	wind	130°-260°	-
ML6	wind and wave	90°-300°	335°-35°
	wind	155°-215°	-

Table 5.2: Applied conditions for wave and wind angle. During time where ADV data is not available only conditions for wind were used

The wind conditions during the measurement period and the final distribution of the used wave directions at measurement locations $ML1$ to $ML5$ is given in figure 5.4. This figure makes it clear that the dominant wave direction is approximately 20 ° off of the dominant wind direction. Since the reef was built perpendicular to the dominant wind direction, most waves thus approach the reef at an angle. If this difference in wind and wave direction is due to refraction or other causes was not resolved.

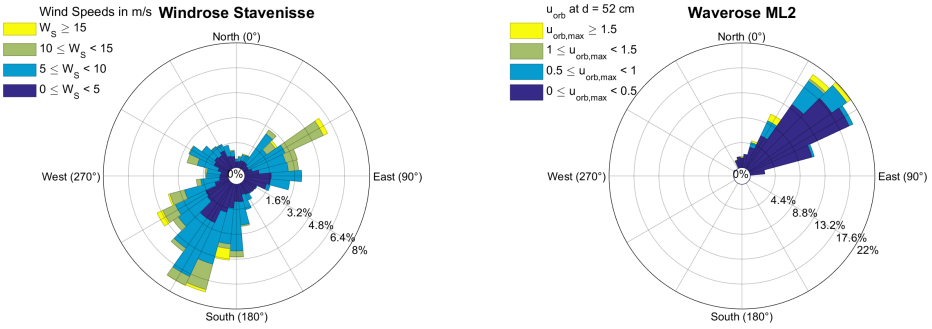

Figure 5.4: wind and wave conditions. left: wind direction and strength during measurement campaign (*Rijkwaterstaat* 2021); right: filtered wave directions during measurement campaign for ML 5; Wind/Wave rose generation: Pereira 2021

5.5. TRANSMISSION

With the derived spectral wave properties the transmission coefficient K_t can be calculated. In literature, this coefficient is typically calculated by comparing an incident wave height H_i with a transmitted wave height H_t, as already explained in section 2. This is feasible if the bed elevation difference between the two measurement points is so small that only little changes in group velocity occur, meaning that shoaling effects on the wave can be neglected. For this case, however, bed elevation differences at the different measurement locations are substantial because of the long transect which was observed (see figure 4.1). To avoid inaccuracies due to the expected shoaling effects, the energy flux F was used instead to calculate a transmission coefficient:

$$K_{t,e} = \frac{F_t}{F_i} \tag{5.7}$$

Where $K_{t,e}$ is the energy flux transmission coefficient, F_t is the transmitted energy flux and F_i is the incident energy flux. The energy flux of spectral wave data can be calculated using linear wave theory. Because of the spectral wave analysis, a representative value of the energy flux had to be found for each spectrum. This was done by calculating the energy flux for each frequency band in the spectrum and then integrating over the results:

$$F = \sum_{1}^{i} S_{\eta\eta,i} * \Delta f * \rho * g * c_{g,i} \tag{5.8}$$

where i is the number of frequency bands, Δf the width of the frequency bands [Hz], $S_{\eta\eta,i}$ the spectral density in frequency band i, $m^2 s$ and $c_{g,i}$ the group velocity in frequency band i. It should be noted that the resulting transmission coefficient $K_{t,e}$ cannot be directly compared to the wave height transmission coefficient K_t, which is usually used in literature. From the squared relationship between wave height and energy, an approximation between $K_{t,e}$ and K_t can be found as:

$$K_t \approx \sqrt{K_{t,e}} \tag{5.9}$$

5.6. UNCERTAINTIES AND SIMPLIFICATIONS

Several simplifications and assumptions were made in the process of calculating the wave parameters and the subsequent analysis. The environment and the instruments themselves further lead to uncertainties. These are treated in more detail in appendix A.6 but quickly summarised below.

Not taken into account is wind-wave input in between the measurement devices, wave reflection from the reef and currents present on the tidal flat.

The instruments themselves have accuracies of ± 0.05 % for the pressure measurements of the OSSIs and accuracies of ± 0.5 % for the velocity measurements of the ADV's and ADCP. However, since temperatures below the recommended range were present during the campaign, higher values might be possible. Furthermore, noise in the measurements due to swinging of the measurement poles can lead to inaccuracies.

Lastly, the applicability of linear wave theory is assumed to represent the present conditions sufficiently enough.

6

RESULTS

With the resulting energy flux data, representing the measured wave data in the obtained data set, objectives two and three were approached. First, a quick overview of the hydraulic forcing over the measurement period is given. Then the wave attenuation is quantified and an attempt to identify the processes involved is made. Finally, the results are parameterized and compared to existing empirical relations.

6.1. HYDRAULIC FORCING

6.1.1. WATER LEVEL DATA

The tidal reference data for the measurement period was retrieved from the Stavenisse weather monitoring site, which is located across from the tidal flat on the opposite side of the channel (figure 6.1). These readings coincide with the water elevation data retrieved from the pressure measurements (see appendix A.4). Visible is a diurnal tide with tidal ranges varying between 2 and 4 m. Additionally, the elevation of the tidal flat at the various measurement locations and the highest reef point (reef crest) are given. For the reef, an immersion time of on average 30 % can be identified.

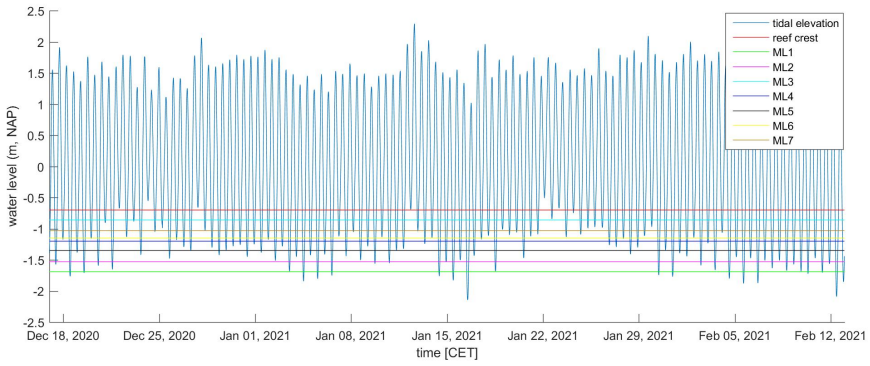

Figure 6.1: Tidal and ML elevation. Tidal data retrieved from the stavenisse weather station located at 51.595576, 4.006483 across the channel of the tidal flat(*Rijkwaterstaat* 2021).

6.1.2. WAVE CHARACTERISTICS

The wave forcing approaching the tidal flat was measured at ML1 with the ADCP (see figure 4.2) and is summarized in figure 6.2. At ML1, the instrument is located close to the edge of the tidal flat and waves are expected to not have changed substantially yet. The maximum observed wave heights H_{m0} are 0.8 m with mean periods reaching up to 3 seconds. Mean wave lengths reached up to 14 m, and are thus of a similar or lower length as the reef width. The maximum peak period was recorded as 4.5 s, but the time series showed strong fluctuations which is why mean wave periods and lengths are shown instead. Curious is the fluctuation of the mean period and wavelength with the tide. This is likely due to tidal induced currents but was not investigated further. During the measurement period four distinctive high energy events at t = 4 days, t = 10 days, t = 27 days and t = 35 days (E1-E4 respectively) with wave heights > 0.5 m can be identified.

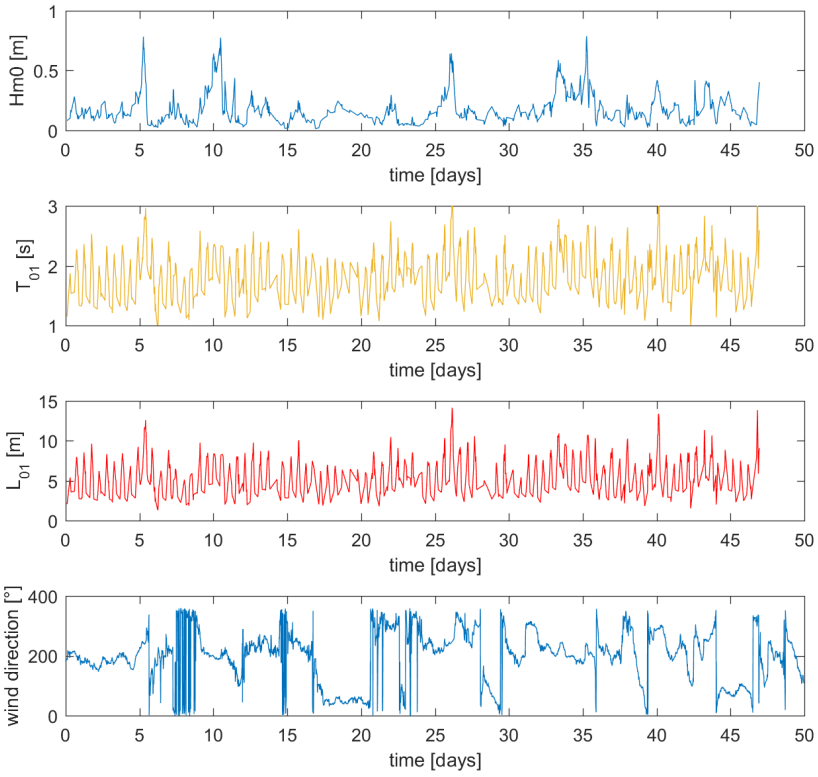

Figure 6.2: Hydrodynamic conditions at ML1 and wind direction. Incoming wave data $H_{m0,i}$, T_{01} and L_{01} retrieved at ML1 (ADCP), measured in period of December 17th 2020 to February 2nd 2021. Wind direction retrieved from the station Stavenisse *Rijkwaterstaat* 2021 used to estimate wave direction.

6.2. USAGE OF THE ENERGY FLUX INSTEAD OF WAVE HEIGHT

In this thesis, the transmission coefficient K_t was calculated using the energy flux contrary to the in literature usually used wave height. This makes it possible to account for expected shoaling effects due to the sloping tidal flat. How this choice affects the end-results is shown in figure 6.3. The red curve shows the relation between the wave height transmission coefficient K_t, calculated as H_t/H_i, and the estimated wave height transmission coefficient $K_{t*} = sqrt(K_{t,e})$, calculated using the energy flux. The concordance is high for K_t values approaching 1 but deviates up to 10 % for lower values, with the mean K_t generally overestimating the transmission compared to the mean K_{t*}. This was to be expected since shoaling leads to an increasing wave height in propagation direction and only occurs when the waves 'feel' the bottom, i.e. waves are attenuating. In conclusion, it can be said that the usage of the energy flux compared to the wave height to calculate the transmission coefficient leads to improved results if shoaling is to be expected.

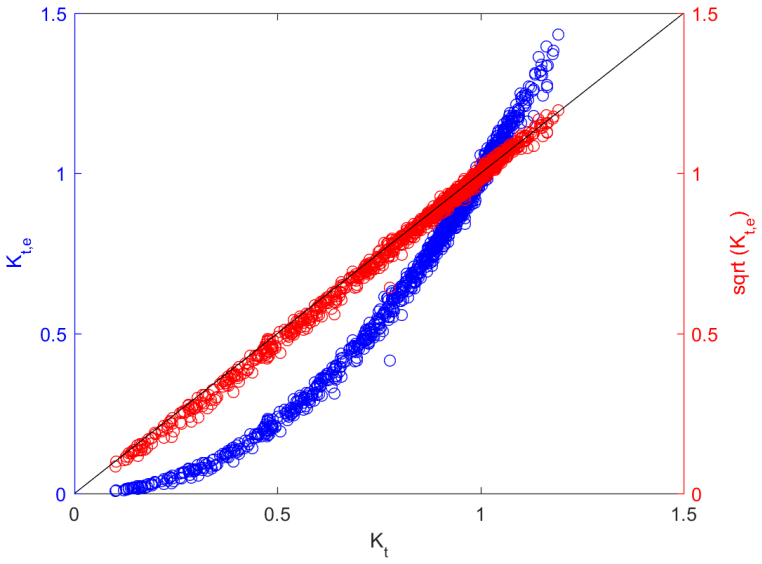

Figure 6.3: Relations between calculated transmission coefficients with: $K_{t,e}$ = energy flux transmission coefficient, K_t = wave height transmission coefficient, $K_{t*} = sqrt(K_{t,e})$ = estimated wave height transmission coefficient

6.3. QUANTIFICATION OF ENERGY ATTENUATION

Before a focus is set on isolating certain processes responsible for the energy attenuation, the total attenuation for all conditions is quantified. This is visualised in figure 6.4, where the relation between incoming, and transmitted energy flux is shown for the different stretches along the measurement transect. The data points are furthermore grouped into seven water depth ranges in steps of 0.5 m. The grouping for all stretches was done in reference to the water depth at ML2, ensuring that per group the same waves are depicted in all stretches. This means that the further landward stretches do not show any values for the lower groups, like d < 1m, since the flat elevation is higher at these points and the measurement devices are not submerged. For each group and stretch then the best fit was found using linear regression. With this linear model, a simple relation between incoming and transmitted energy flux attenuation is found for different water levels using the slope of the line. ML5ML6 and ML6ML7 have a lower amount of data since the wave direction criteria for ML6, explained in section 5.4.2 was applied. Data for all other stretches were filtered for the less strict wave direction criteria regarding ML5 to make sure only waves propagating landward are resolved.

Visible is that the attenuation is most effective over the reef itself, showcased by the stretches $ML2ML5$ and ML3ML4, which represent the total attenuation by the reef and the attenuation on top of the reef respectively. ML2ML5 shows that for water levels < 1m the reef attenuates nearly all energy. With increasing water levels the attenuation reduces, as expected. Generally, the reef seems to be effective up until a water level of 2 m with only minimal reduction for higher water depths. The stretch $ML3ML4$ shows a similar picture. This stretch represents attenuation only on top of the reef, meaning that in the case of no breaking waves this stretch represents attenuation due to oyster induced friction. Consequently, it also shows attenuation up until a water depth of 2 m, but to a lesser extent. No attenuation was measured on the stretch $ML5ML6$ for all water levels. This sector represents the 93 m stretch between ML5 and ML6 behind the reef. At this stretch thus no wave energy reaches the bed. Further landward, at the stretch $ML6ML7$, attenuation can be detected again. This stretch is difficult to interpret though since the directional spread of the incoming waves will always lead to waves being measured at ML7 that did not pass the reef. It does indicate though that in-between ML6ML7 wave energy again reaches the bed.

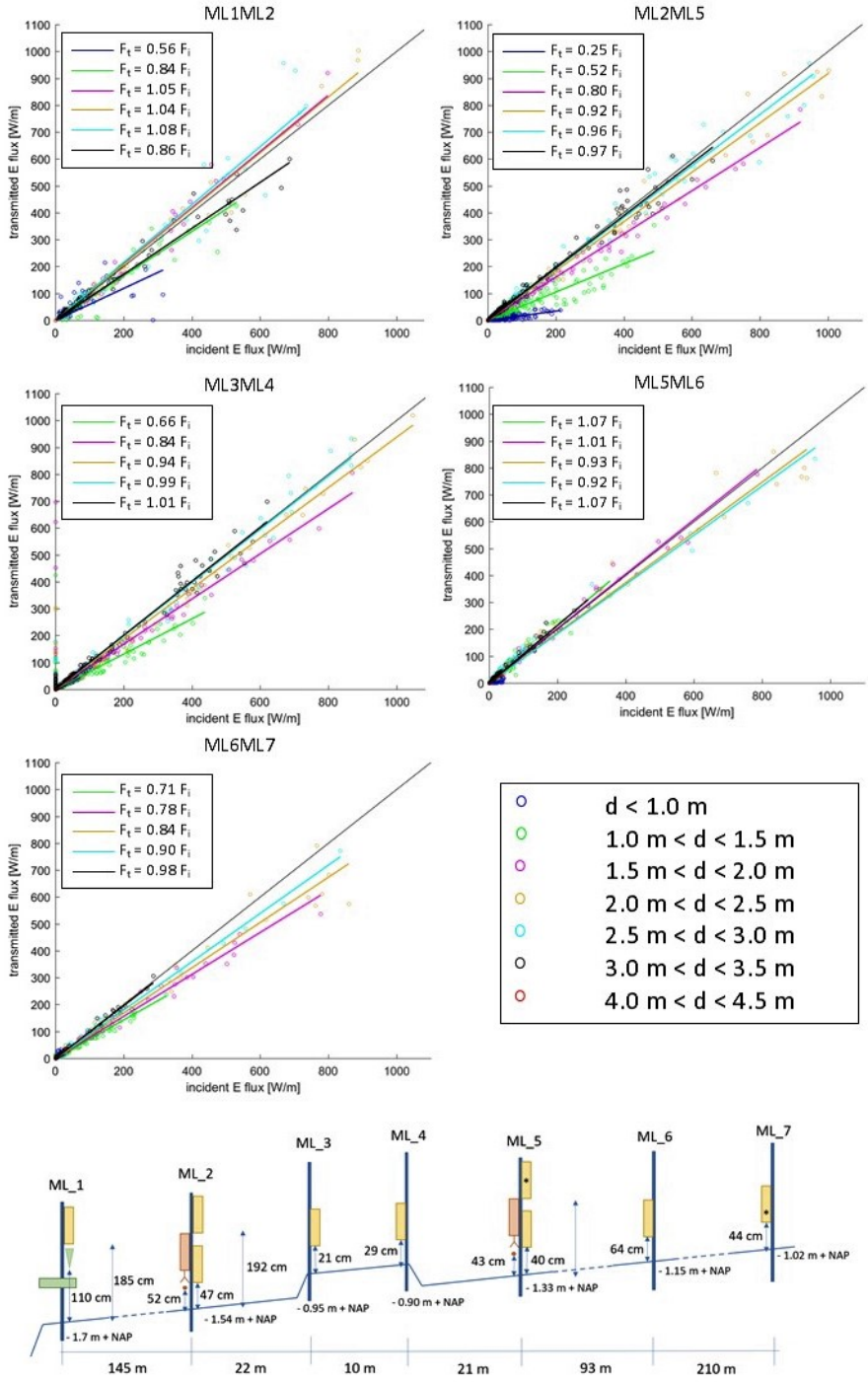

Figure 6.4: Quantification of attenuation by means of water depth. Incident and transmitted energy flux are compared over different measurement transect stretches. The results are grouped into water depth ranges with water depth being in relation to ML2. These groups are indicated with different colors. The legends express the linear relation between incoming and transmitted energy flux. Linear regression was used to find the linear relations.

It should be noted that the observed transects exhibit different lengths, e.g. the dissipation measured in front of the reef, visualised by ML1ML2, is achieved over a stretch of 145 m, while the dissipation over ML2ML5 is achieved over 53 m. Comparing the total attenuation of energy as shown in figure 6.4 can thus lead to misconceptions regarding the effectiveness of the dissipation. A more appropriate way to compare the dissipation by the reef to the dissipation on the bare tidal flat is by showcasing the dissipation rate calculated as:

$$dissipationrate = \frac{\Delta F}{\Delta d} \tag{6.1}$$

Where ΔF is the Energy flux difference between two measurement locations and Δd is the distance between two measurement locations. Figure 6.5 thus shows the dissipation rate in between the stretches ML1ML2 and ML3ML4. The dissipation rate at ML1ML2 hereby represents the dissipation rate by the bare tidal flat, while ML3ML4 represents the dissipation rate on top of the reef. It can be seen that the dissipation over the reef at ML3ML4 is on average ~ 18 times more effective than the dissipation in front of the reef measured at ML1ML2.

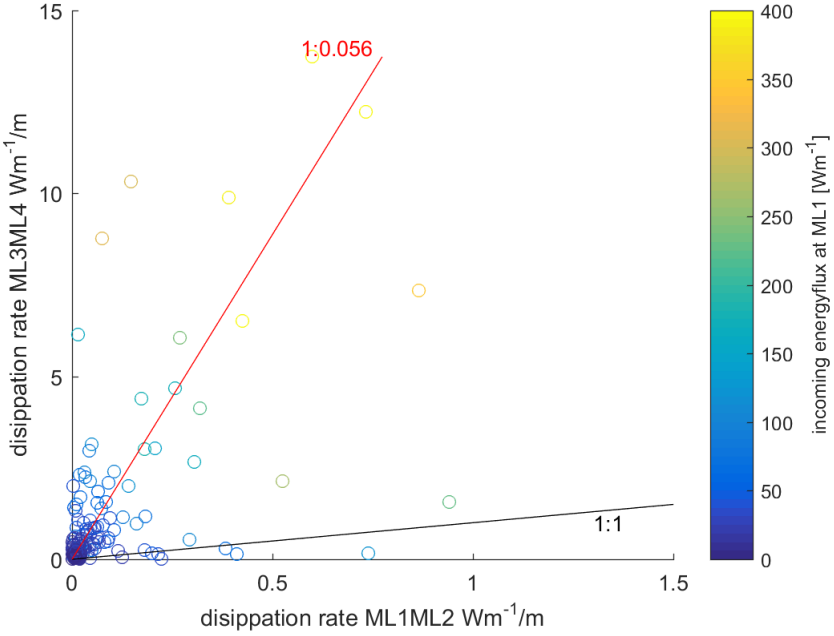

Figure 6.5: Dissipation rate in Wm^{-1}/m for ML1ML2 and ML4ML5. Only time series where both stretches experience energy dissipation are plotted. Black line indicates equal dissipation rate, red line indicates mean relation between the two dissipation rates using linear regression.

Furthermore of interest is the total amount of attenuated energy flux, since this gives context to the contained energy of the incident waves. This is shown in figure 6.6, with each line representing the change in energy flux in front of and behind the reef at $ML2$ and $ML5$ respectively. Lines coloured with the color-code indicate wave attenuation while dashed pink lines indicate energy growth. The area where continuous attenuation can be seen is indicated in red. Interesting is hereby that the highest energy waves for a certain water depth, indicated by the corresponding line being close to the lower red border, all show similar total values of energy flux attenuation, namely 150 to 200 W/m^2. This holds up until a water depth of approximately 2.4 m, above which total attenuation decreases rapidly, also for high energy waves. The figure thus shows that the attenuation capabilities of the reef during high energy events in terms of total energy attenuated are roughly constant up until a certain water depth.

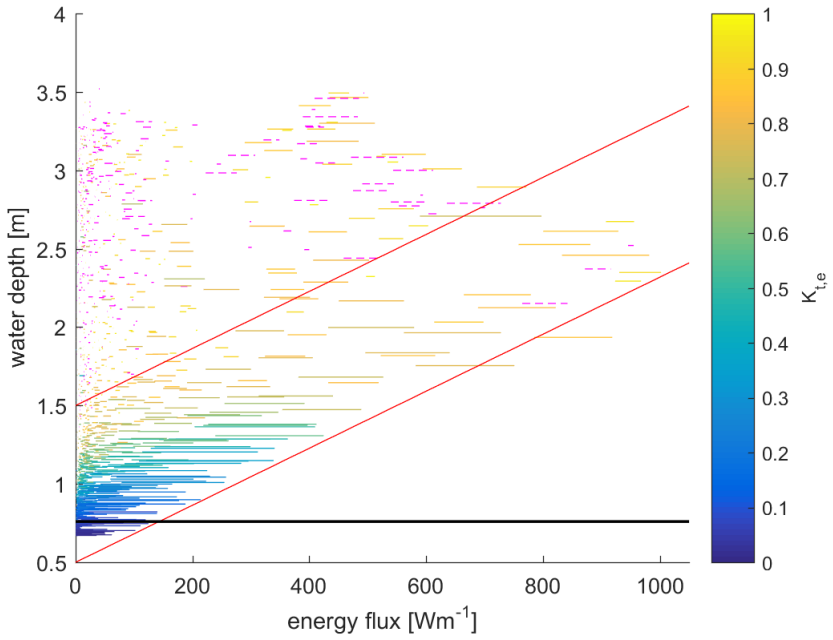

Figure 6.6: Total dissipation. Energy flux difference over the reef at different water depths. Each line represents the change in Energy flux between ML2 and ML5 at a certain time interval. Lines in the color-code indicate energy attenuation, while dashed, pink lines represent energy growth. Water depth is given in relation to ML2, the black line represents the reef crest.

6.4. ATTENUATION MECHANISMS

Several mechanisms lead to wave attenuation over submerged structures. Some important ones are wave breaking, friction and overtopping, with wave breaking generally being considered as the most important one (Seabrook and Hall 1998). All these attenuate energy by inducing turbulent motions, which ultimately convert the energy to heat. Additionally, reflection can reduce wave energy leeward of the structure. Contrary to the other mechanisms this does not directly attenuate wave energy but rather redirects it back seaward. Quantifying each of these mechanisms at different conditions is out of the scope of this thesis. In the following rather an analysis of the relative importance of these mechanisms under different conditions of the relative submergence $d_s / H_{m0,i}$ was made.

6.4.1. ATTENUATION EVOLUTION OVER ONE STORM EVENT

In order to draw some first understanding of what mechanisms govern the attenuation process, we first focus on only one storm event. For this, the storm event E2 (see figure 6.2) was chosen, which lasted for approximately 36 hours on the 26th and 27th of December, including three tidal cycles. Wave heights varied between 20 cm and 77 cm while mean periods were all between 1 and 3 seconds. Wave directions varied between 40 ° and 60°, leading to incident wave angles between 20 ° and 40 ° in relation to the reef. To evaluate the attenuation of the waves the transmission coefficients for the energy flux $K_{t,e}$ were calculated for certain stretches of the measurement transect: ML1ML2 representing the attenuation in front of the reef, ML2ML5 the attenuation over the entire reef, ML3ML4 the attenuation right on top of the reef and ML5ML6 the attenuation behind the reef (See figure 6.4 for instrument locations). Additionally, the relative submergence $H_{m0,i} / d_s$ is plotted, since this is a measure for reef induced wave breaking. $H_{m0,i}$ is hereby the incoming wave height measured at ML2 and d_s is the reef freeboard. The results are visualized in figure 6.7.

Figure 6.7 visualises how the attenuation of waves varies at different locations within a tidal cycle during a storm event. The $ML2 - ML5$ curve shows clearly that even the highest waves are unaffected by the reef during high tide, indicated by a transmission coefficient of $K_{t,e} = 1$. The length of the period where waves are unaffected depends on the wave height, as seen by the high energy waves during the second tidal cycle being unaffected for only 3 hours while the low energy waves during the first tidal cycle being unaffected for roughly 6 hours. The attenuation values measured in between (ML3-ML4) are quite consistent with the attenuation over (ML2-ML5), showing only slightly higher values at decreasing water depths. This indicates, that at least up until the water depth where (ML3-ML4) could be resolved, the attenuation is mainly occurring on top of the reef.

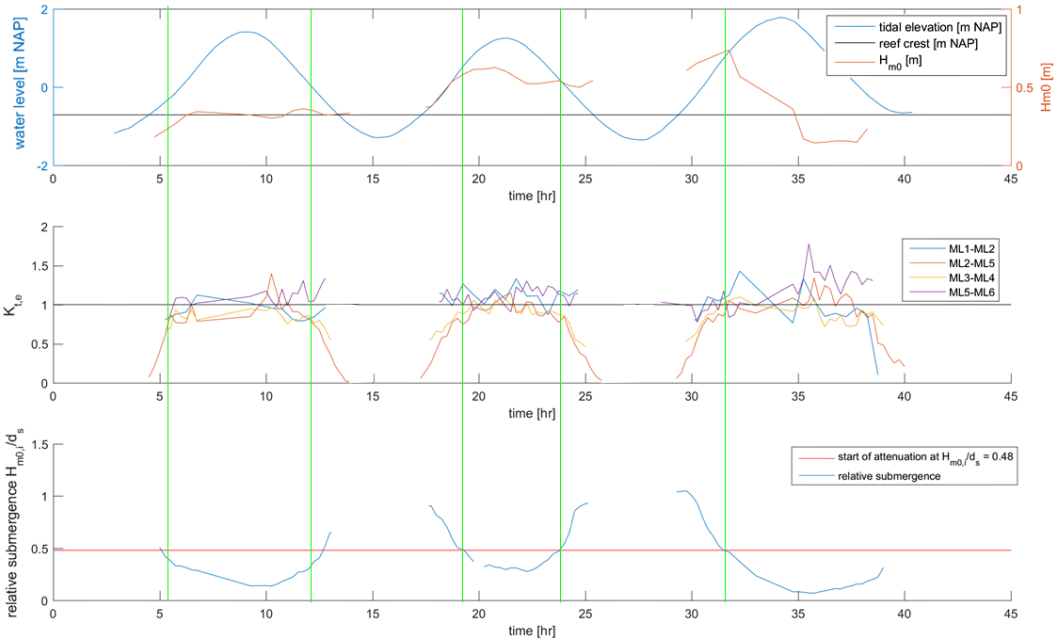

Figure 6.7: Analysis of waves over one storm event. top: tidal elevation(blue), H_{m0} at ML_1 (red) and reef crest elevation (black); mid: transmission coefficient in between two measurement points. ML1ML2 attenuation in front of the reef, ML2ML5 the attenuation over the entire reef, ML3ML4 the attenuation on top of the reef, ML5ML6 the attenuation behind the reef; bottom: relative submergence $H_{m0,i}/d_s$ (blue), with $H_{m0,i}$ being the incoming wave height measured at ML2 and initiation point for attenuation (red); Green lines indicate start of attenuation for stretches ML2ML5 and ML3ML4. Only data with submergence of instruments > 20 cm was used, white areas in between data points indicate lower water levels where no data was measured.

Focusing on the attenuation over (ML2-ML5) only, it can be seen that with decreasing water level, waves start to attenuate rapidly at a certain $H_{m0,i}/d_s$ ratio. For high energy waves, seen during t = 15-33 hr, this ratio seems to constantly be $H_{m0,i}/d_s = 0.48$, while for smaller waves this ratio is lower. The average point where attenuation processes start will be further investigated in the next section. At low tide, when the water level sinks below the reef crest, transmission coefficients reach values below 0.1. The incoming wave energy is reflected back seaward or attenuated on top of the reef due to overtopping.

When looking at the wave attenuation away from the reef, it is visible that both in front (ML1-ML2) and behind the reef (ML5-ML6) transmission coefficients are consistently depicted as around 1. However, especially in front of the reef at ML1-ML2, depth induced breaking is expected to be initiated during lower water depths, meaning that in the blank, not resolved areas, the transmission coefficient will decrease in reality. Yet this figure is showing that wave attenuation is predominately happening on the reef.

Curious are the spikes showcasing transmission values of $K_{t,e} > 1$, indicating an increase

in energy flux. These seem to predominantly happen in between ML1ML2 and ML5ML6, where wind input could be responsible for this energy gain because of the larger distances (see figure 4.2). The scatter furthermore seems to be stronger at low $H_{m0,i}/d_s$ ratios during high tide. During such conditions the spectral analysis is more error-prone, giving a possible explanation for the fluctuations when $K_{t,e}$ is around 1.

6.4.2. WAVE BREAKING

In the previous section, the evolution of the transmission coefficient was analysed over one storm event. An assumption that wave breaking governs the start of attenuation was made. To see under what conditions wave breaking is actually likely to occur, the asymmetry of waves was calculated on the entire measurement transect. The asymmetry hereby indicates the relative steepness of the wavefront and can thus be used as a measure for wave breaking. A high negative value hereby represents a large asymmetry. Since an irregular wave field is analysed, the magnitude of the asymmetry indicates the amount of waves in that wavefield that break. E.g. if the asymmetry is 0 no waves in the wave field break and for increasing negative values an increasing amount of waves in the wave field break.

A strong relation between relative submergence $d_s/H_{m0,i}$ and asymmetry was found (see figure 6.8). The asymmetry clearly increases for smaller relative submergence and transmission coefficients. This effect is approximately visible until relative submergence of $d_s/H_{m0,i} = 2$, indicating that wave breaking only occurs until this value. Looking back at figure 6.7, this is also roughly the value where attenuation starts during the observed storm event.

The asymmetry was furthermore calculated for all other measurement locations (see appendix A.7). At ML2, ML5, ML6 and ML 7 asymmetry values showed no trends, with all values scattered around an asymmetry of 0. It can thus be said that on the measurement transect little to no wave breaking occurs away from the reef. Energy is thus likely dissipating mainly by bottom friction and white capping.

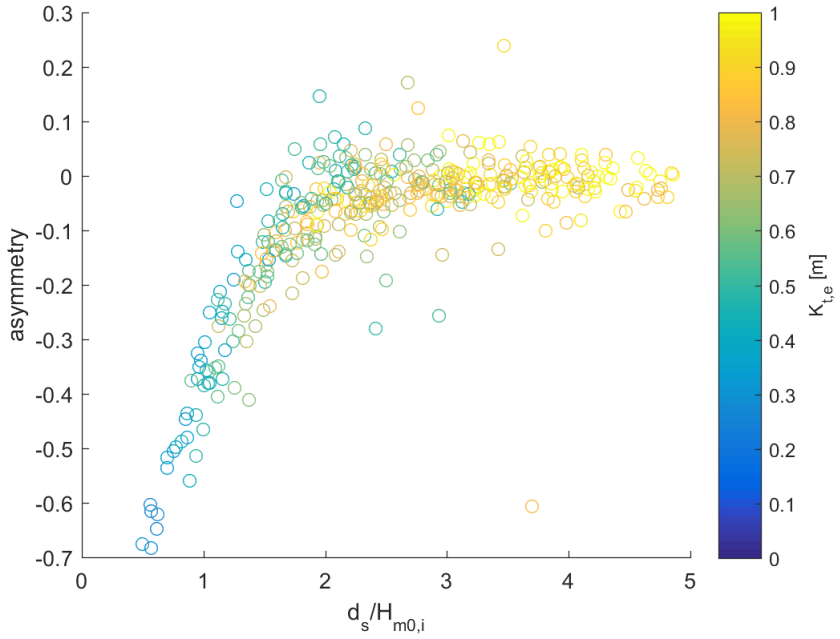

Figure 6.8: Asymmetry plotted vs the relative submergence $d_s/H_{m0,i}$. $H_{m0,i}$ is the incoming wave height at ML2 and d_s is the reef freeboard. Asymmetry was measured on top of the reef at ML3. Asymmetry is increasing with negative values, a value of 0 indicates zero asymmetry. The asymmetry was only calculated for $d_s/H_{m0,i}$ values lower than 5. The color-code indicates the transmission coefficient over the reef

6.4.3. OTHER MECHANISMS

Other relevant mechanisms are reflection, overtopping and friction. Reflection and overtopping are dominant during conditions of $d_s/H_{m0,i} < 0$, where the water line is at or below reef crest. At such water levels the transmission is close to 0 (figure 6.4) and nearly all energy is reflected back offshore or dissipated on top of the reef by overtopping. At $d_s/H_{m0,i} > 0$ the effect of overtopping and reflection will reduce. A quantitative analysis of the conditionality of reflection regarding $d_s/H_{m0,i}$ using the velocity data was not done. At $d_s/H_{m0,i} > 2$, no dissipation by wave breaking can be expected (figure 6.8). However, noteworthy dissipation is still visible up to $d_s/H_{m0,i} = 4$. Thus it can be said that friction contributes significantly to dissipation over a large range of $d_s/H_{m0,i}$. A schematic of the range of the importance of the different mechanisms is given in figure 6.9.

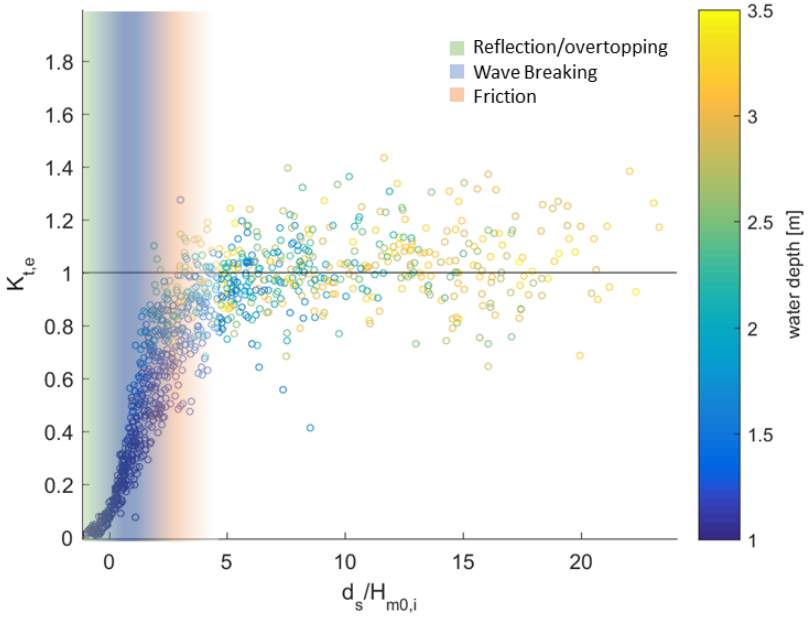

Figure 6.9: Range where attenuation mechanisms are dominant in relevance to $d_s/H_{m0,i}$. $d_s/H_{m0,i}$ is the relative submergence, $K_{t,e}$ is the transmission coefficient between ML2ML5. The color-code indicates the water depth at ML2.

6.5. CONCEPTUALIZATION OF THE FINDINGS

The above analysis quantified the wave attenuation and showed which processes govern it. However, ultimately not only the quantification of the attenuation but also the spatial footprint of the reef where reduced wave energy can be expected is of interest. This was not quantified per se but conceptualised using the collected data.

Figure 6.10 shows the evolution of the energy flux over the measurement transect under different conditions of $d_s/H_{m0,i}$. Visible is that for high $d_s/H_{m0,i}$ values, no wave energy is attenuated both in front of (ML1-ML2) or behind the reef (ML5-ML7). Since the little attenuated energy by the reef is furthermore regained quickly, the footprint of the reef can thus be seen as 0 for such $d_s/H_{m0,i}$ values.

For lower values of the relative submergence such as $d_s/H_{m0,i}$ = 1.5 and 2.6, a footprint can be identified. This is indicated by wave energy being attenuated in areas where the reef has little or no influence (ML1ML2 and ML6ML7), while directly behind the reef (ML5ML6) no attenuation was measured. This can be attributed to the reef attenuating a significantly higher percentage of the incoming wave energy than during high $d_s/H_{m0,i}$ values, leading to the transmitted wave energy not reaching the bed at ML5ML6. Wind input does furthermore not lead to complete recovery of the wave energy, meaning that

reduced energy fluxes can be expected until well behind ML6.

The footprint of the reef for $d_s/H_{m0,i}$ values of 1.5 and 2.6 is further visualised in figure 6.10 by estimating a 'no reef' scenario, where the energy attenuation rate measured on the stretch ML1ML2 is transferred to the entire measurement transect ML1ML7 (see dashed lines). A comparison between the measured and the 'no reef' scenario shows that for a $d_s/H_{m0,i}$ value of 1.5 the measured energy flux at ML7 is likely to be lower than in a no reef scenario, while for higher $d_s/H_{m0,i}$ ratios little effect can be expected by the reef at ML7. This indicates that the footprint of the reef is time-dependent and varies with different $d_s/H_{m0,i}$ values.

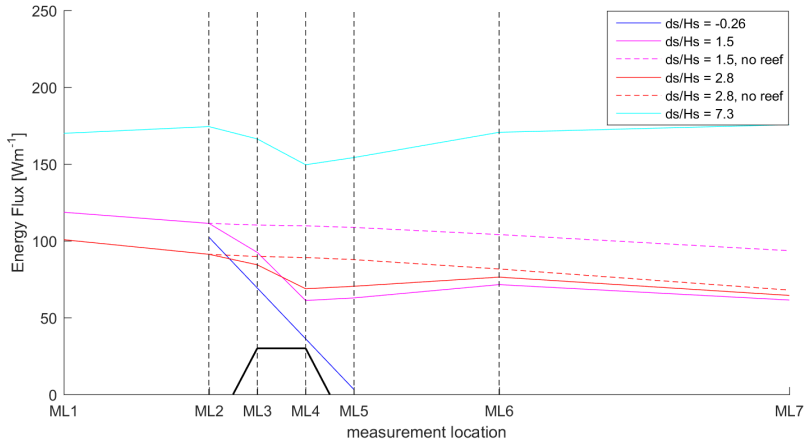

Figure 6.10: Evolution of the energy flux over the measurement transect. Dashed lines: estimated Energy flux by using the attenuation rate of ML1ML2. Note that the x axis is not to scale.

The above findings of the footprint of the reef and the quantification of attenuation are conceptualised in 6.11. Three main lessons are incorporated in the figure which are indicated by the enumeration a.), b.) and c.).

(a) Three distinctive ranges of the freeboard $d_s/H_{m0,i}$ were identified to describe conditions of wave attenuation. In range 1, $d_s/H_{m0,i} < 0$, the water level is below the reef crest and waves are attenuated by nearly 100 %. In range 2, $0 < d_s/H_{m0,i} < 4$, the reef is submerged, and the attenuation reduces with increasing $d_s/H_{m0,i}$. In range 3, $d_s/H_{m0,i} > 4$, the waves cross the reef nearly undisturbed, and little to no energy is attenuated.

(b) Wind input leads to the attenuated waves growing again after they passed the reef. High $d_s/H_{m0,i}$ values hereby lead to a quick and complete recovery of the wave height. For low $d_s/H_{m0,i}$ on the other hand the wind will take a long time until the lost wave energy is recovered. The distance until which the reef has an impact is

thus time-dependent on $d_s / H_{m0,i}$. This has implications for the footprint which is covered in c.)

(c) How strong and how often the reef reduced wave energy at certain distances is described by the footprint. Behind the reef, a strong reduction was measured with no wave energy reaching the bed over some distance for all $d_s / H_{m0,i}$ conditions. Further away from the reef, effects such as wind input and the directional spread of waves become important and reduce the impact of the reef, both in its magnitude and duration wise. Here reduced wave energy was thus measured for only some $d_s / H_{m0,i}$ ratios. Even further away from the reef, no impact of the reef on wave height can be expected for all $d_s / H_{m0,i}$ values.

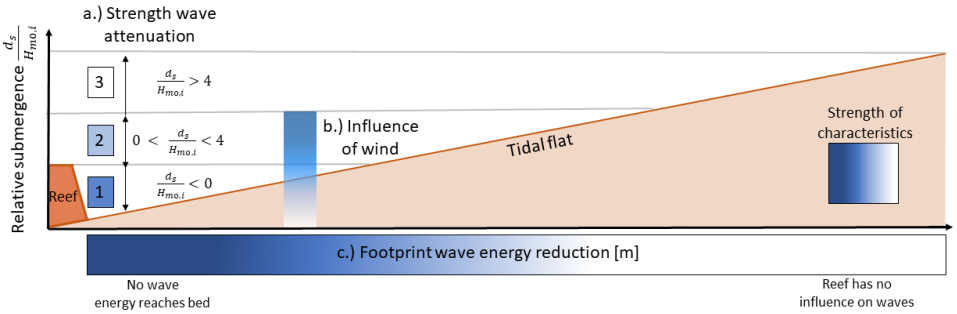

Figure 6.11: Conceptualisation of the conditionality of wave attenuation and the footprint of the reef under different $d_s / H_{m0,i}$ ratios. a.) reflects on the magnitude of attenuation in relation to the relative submergence, the pictured $d_s / H_{m0,i}$ values are exemplary for this case but may vary b.) reflects on how quickly the influence of wind on the transmitted waves restores the waves to their incoming height, c.) reflects on the footprint of the reef where, and how strong reduced energy can be measured behind it. The color-code indicates the strength of the different characteristics at certain relative submergence or distance from reef.

6.6. PARAMETERIZATION OF THE RESULTS

In chapter 6.3 some predictability for the wave attenuation was already achieved by using the water depth. The resulting figure 6.4 however, is only valid for the observed oyster reef. To achieve a more general tool to predict attenuation, which also holds validity for other reefs, the results need to be parameterized. Such a parameterization can ultimately be used to develop an empirical relation describing the attenuation. The aim of this chapter is not yet to develop such a relation, but rather to investigate the relative importance of certain parameters.

This was done by linking dimensionless numbers to the measured distribution of wave transmission. Ideally, the dimensionless numbers further represent the main mechanisms that were found responsible for the attenuation over the reef: wave breaking, overtopping, reef friction and reflection. One dimensionless number may represent the

attenuation by one, or several of the mechanisms involved, while the attenuation is represented by the transmission coefficient $K_{t,e}$ measured between ML2ML5. As a base for this analysis, the empirical relations regarding submerged breakwaters, which were covered in chapter 2.2.2 are used.

The dimensionless numbers are typically composed of 2 to 4 parameters, with at least one describing a reef, and one describing an incoming wave characteristic, e.g. B/h, H_s/B. However, since in this analysis only one reef was observed, the reef characteristics used in the dimensionless numbers, such as B or h_s are constant. Thus only single parameters of the incoming wave characteristics can be responsible for the distribution of the transmission coefficients. One exception is the dimensionless number $d_s/H_{m0,i}$, whose reef parameter is the freeboard, which changes with the tide. The validity of other typical dimensionless numbers such as used in Seabrook and Hall 1998 could however not directly be investigated.

Wave breaking is considered as the most important mechanism in energy attenuation over submerged structures and can be represented by the dimensionless number $d_s/H_{m0,i}$. This parameter describes the relative submergence of the reef crest and is typically used as the main parameter to describe the transmission coefficient over submerged structures (Seabrook and Hall 1998, Van der Meer et al. 2005). How the relative submergence relates to the transmission coefficient $K_{t,e}$ for the observed reef is shown in figure 6.12. A strong dependence is visible, with the overall shape of the relation being quite similar to the one collected for breakwaters in Van der Meer et al. 2005.

For negative or small $d_s/H_{m0,i}$ values, the relation is well defined and shows little scatter. With increasing $d_s/H_{m0,i}$ values, however, the scatter in the data increases continuously and the relation becomes less clear. Part of this scatter is likely caused by other mechanisms becoming more relevant, meaning that additional wave and reef characteristics than d_s and $H_{m0,i}$ play a role. However, it should be noted that also the data quality of the instruments decreases with higher $d_s/H_{m0,i}$, which likely also contributes to some of the scatter.

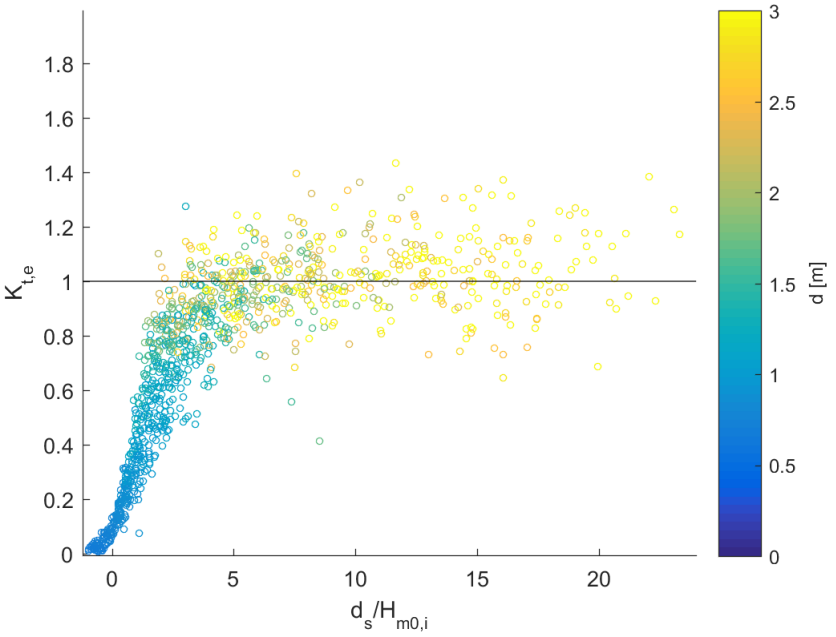

Figure 6.12: Relative submergence vs $K_{t,e}$: The transmission factor was captured in between ML2ML5. d_s is defined as the water depth above the highest reef point and $H_{m0,i}$ is the incoming water height measured at ML2. The color-code indicates the water depth in front of the reef at ML2.

Figure 6.12 shows that the factor $d_s/H_{m0,i}$ defines the transmission coefficient $K_{t,e}$ very well for low $K_{t,e}$ values, and other parameters only become important for higher $K_{t,e}$ values. Which parameters play a role in the spread was investigated in the following by imposing different parameters as a color-code on 6.12.

In the formulas discussed in chapter 2.2.2, the incident wave height appears not only in the dimensionless number $d_s/H_{m0,i}$, but also in the dimensionless number $H_{m0,i}/B$. The wave height hereby plays a different role in these factors, with a increased wave height in $d_s/H_{m0,i}$ leading to a decrease in transmission, while in $H_{m0,i}/B$ a increasing wave height leads to an increase in transmission. The same effect was also found in the measured data (see figure 6.13 top left), where at a specific relative submergence $d_s/H_{m0,i}$ a high incident wave height $H_{m0,i}$ leads to an increase in transmission. This leads to the conclusion that the effect of an increase in d_s dominates the effect of an increase in $H_{m0,i}$, e.g. in a situation where d_s = 1 m and $H_{m0,i}$ = 1 m, more energy is attenuated than in a situation where d_s = 1.5 m and $H_{m0,i}$ = 1.5 m, even though both situations have the same dimensionless freeboard, $d_s/H_{m0,i} = 1$.

The wavelength plays an important role in the attenuation, since the depth until wave energy penetrates into the water column is largely determined by the wavelength. All

formulas discussed in chapter 2.2.2 thus use dimensionless numbers such as L/B or $H_{m0,i}/L_{01,i}$. In figure 6.13 top right, the wave steepness $H_{m0,i}/L_{01,i}$ of the incoming waves was imposed on figure 6.12, showing a strong relation between the factors. A large steepness hereby leads to more transmission, with this effect rising for larger $d_s/H_{m0,i}$ values. This is likely due to less attenuation by friction. For $d_s/H_{m0,i}$ values around or below 0, the effect reverts, with a large steepness leading to less transmission. This is likely due to long waves with smaller wave heights being more likely to roll over the reef while being less likely to break.

The incoming wave direction was imposed in figure 6.13 bottom. It can be seen that the angle at which waves approach the reef generally have no impact on the transmission. This confirms the research made in Van der Meer et al. 2005 and Seabrook and Hall 1998.

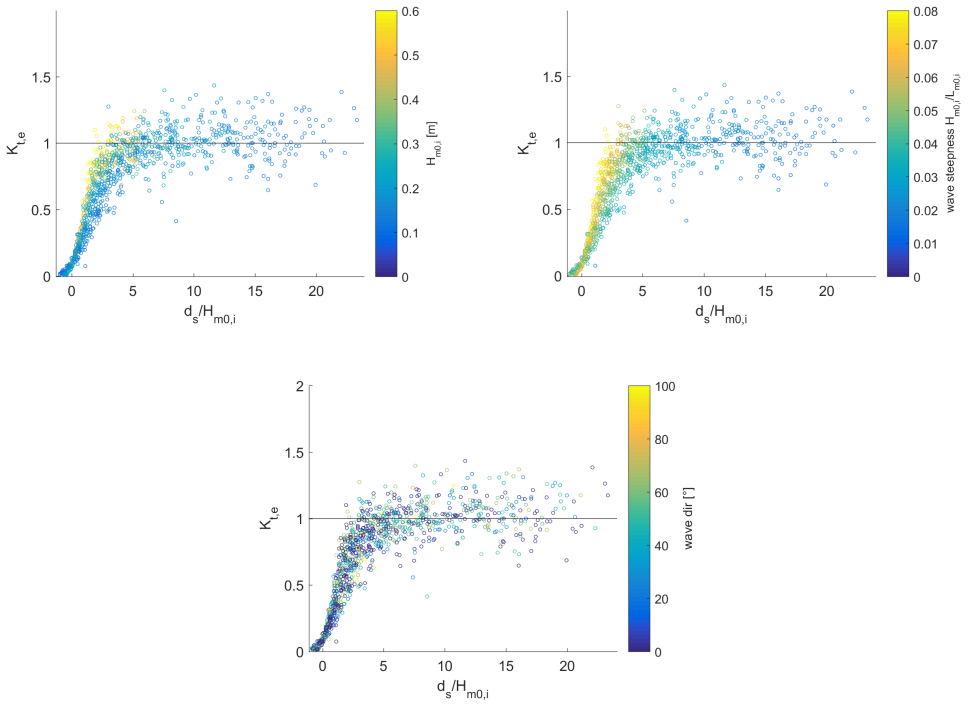

Figure 6.13: Transmission factor captured in between ML2ML5 against the dimensionless freeboard. The color-code indicates a third parameter. Reef parameter were not used since they are constant. Color-code indicates: top left $H_{m0,i}$; top right $H_{m0,i}/L_{01,i}$; bottom wave direction. All wave parameters were measured at ML2

In figure 6.13 top right, a strong dependence between the incoming wave steepness, the relative submergence and the transmission coefficient was found. The wave height being present in both $H_{m0,i}/L_{01,i}$ and $d_s/H_{m0,i}$, indicates that the parameters $L_{01,i}$ and d_s in combination also have a strong dependence with the transmission factor. Thus the

transmission was plotted against the dimensionless number $d_s/L_{01,i}$. The resulting figure shows a similar structure as in figure 6.12, but with less spread in the higher $K_{t,e}$ parts. This spread could not be explained with the influence of any other parameters. Generally the results are intuitive with a higher d_s or a lower $L_{01,i}$ leading to an increase in transmission.

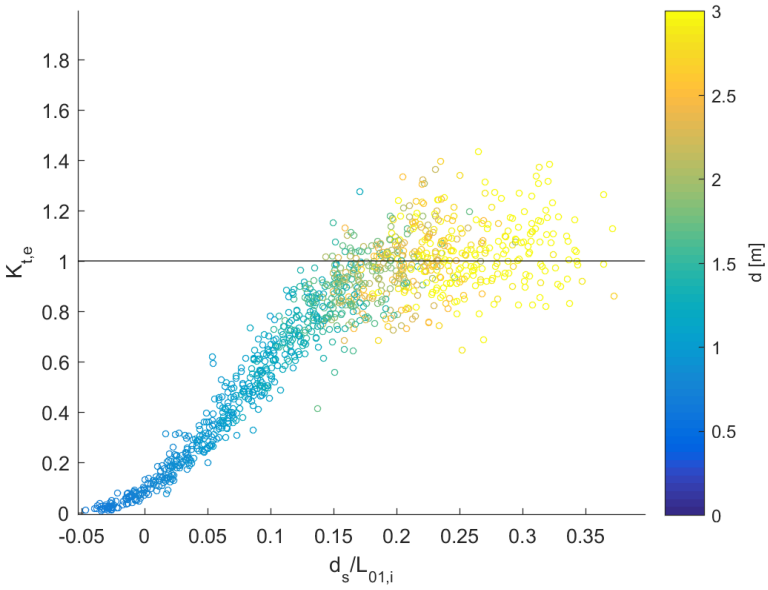

Figure 6.14: Transmission factor captured in between ML2ML5 against $d_s/L_{01,i}$. $L_{01,i}$ is the incoming wave length measured at ML2. The color-code indicates the water depth at ML2.

The above results show which parameters dominate the wave attenuation over the observed oyster reef. Generally, it was found that the dimensionless numbers used in the three empirical relations for submerged breakwaters work similarly for the oyster reef, indicating that these formulations could be used as a base to predict attenuation over oyster reefs. However, the best performing dimensionless number was found to be $d_s/L_{01,i}$, which only plays a minor role in the submerged breakwater equations.

6.7. PREDICTABILITY OF RESULTS WITH EXISTING EMPIRICAL RELATIONS

It was shown that the parameters used in the empirical relations of Van der Meer et al. 2005, Seabrook and Hall 1998 and Srineash and Murali 2019 (see chapter 2.2.2) capture similar effects for the oyster reef as for submerged breakwaters. The performance of these empirical relations in predicting the measured wave transmission between ML2ML5 was thus examined in the following.

To set up the equations, several reef characteristics such as structure width B, structure slope α or armour layer grain size $D_{50,a}$ need to be determined. Considering the inhomogeneous nature of the oyster reef, it is difficult to find representative values of these for the entire reef. As shown in figure 3.7 the width of the reef can vary by several meters. Also, the definition of d_s is not clear because of a varying structure height h_s, oyster density and flat elevation. Assigning the oysters a $D_{50,a}$ is also problematic considering the varying oyster size and population density. All this is in contrast to the well defined, trapezoidal-shaped breakwater structures, used to develop the formulas.

For a first assessment, the reef characteristics on the measurement transect were used as summarized in chapter 3.2. For a reef width B, 4 m was chosen to account for the quickly falling reef height over the width. The highest reef height h_s, which defines d_s was chosen as 0.78 m. For the slope in front of the reef α, 20° was chosen and for the grain size, D_{50a}, 0.1 m. For the wave parameters, the incoming wave characteristics measured at ML2 were used. It should be noted that the chosen reef parameters not only impact the results of the equations but also play a role in determining the bounds of the used equations, limiting the data which can be compared.

The transmission coefficients calculated by the equations can not be directly compared to the measured transmission coefficients, since the equations calculate the wave height transmission coefficient K_t, while the measured transmission is presented as the energy flux transmission coefficient $K_{t,e}$. Thus the measured $K_{t,e}$ was converted to an estimated K_t using equation 5.9.

The resulting comparison of the calculated and the measured transmissions coefficients are shown in 6.15. For the chosen reef parameters the equations underestimate the transmission coefficient, with root mean square errors (RMSE) of around 0.2. However, a high correlation factor R of 0.8 to 0.9 was found. This indicates that the formulas correctly represent the processes happening over the oyster reef and can be tuned to better present the measured data.

The Van der Meer et al. 2005 equations seem to be best suited to represent the measured data. The Srineash and Murali 2019 results show similar RMSE and R values but seem to perform poorly for low transmission coefficients. The Seabrook and Hall 1998 results contain the most data points, especially for larger transmission coefficients, but also show a larger spread.

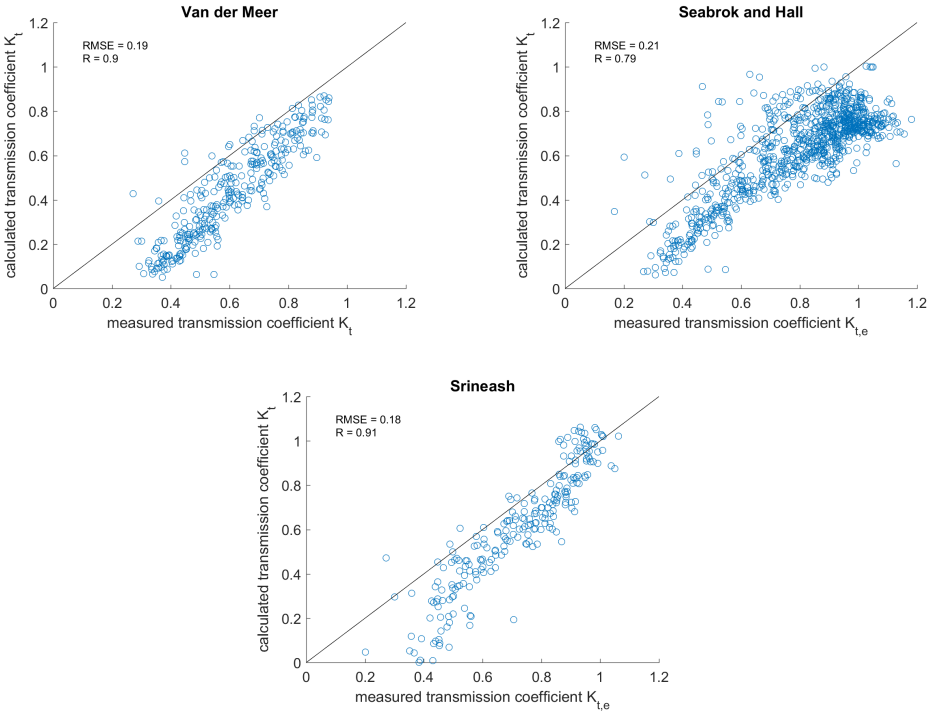

Figure 6.15: Results of the comparison of the calculated transmission coefficients and the measured transmission coefficient for B = 4 m, h_s = 0.78 m, α = 20 ° and D_{50a} = 0.1 m

As explained above it is unclear how to find representative reef input values for the equations because of the inhomogeneity of the reef. Thus it was examined what change in the input values leads to better results than in 6.15.

The equations are most sensible to changes in the reef height h_s (via d_s) and the reef width B. Both a decrease in the reef width B and a decrease in the reef height h_s hereby lead to an increase in the calculated transmission and thus better results. Other reef parameters only have a minor influence. Optimization of the input parameters of the Van der Meer et al. 2005 equation is shown in figure 6.16. By changing the reef width B to 3.7 m and the reef height h_s to 0.66 m a RMSE of 0.087 was obtained. Optimization for the other equations can be found in the appendix (A.8).

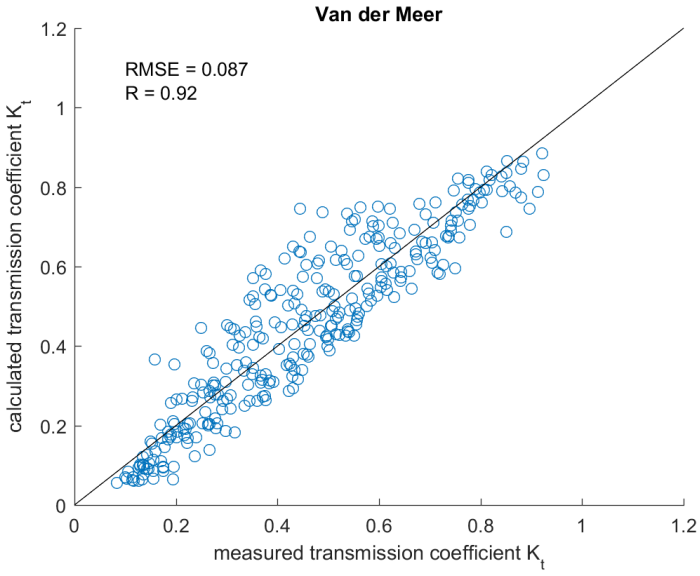

Figure 6.16: Van der Meer transmission compared to measured transmission. VdM calculated with B = 3.6 m and h_s = 0.66 m

It can be concluded that the equations can reproduce the measured transmission reasonable well. However, the values of h_s and B needed to get the best results, deviate from the originally measured values collected on the measurement transect. It can be said though, that the used values to reach the best results, e.g. $h_s = 0,66m$ and B = 3.6 m for the Van der Meer et al. 2005 equations, can still be motivated due to the inhomogeneity of the reef. The h_s = 0.78 m used so far is e.g. defined as the reef height from the bed elevation to the tip of the highest oysters, while a h_s = 0.66, used in 6.16 could be defined as the reef height from the bed to the base of the oysters, where they are attached to the reef structure. The smaller reef with B which is used can be motivated by the reef elevation being substantially below the highest reef elevation h_s for a large part of the reef width. However, it is not clear how and if these definitions could be transferred to other cases.

7

DISCUSSION

In the following, the interpretation of the found results is discussed. First, an overview of the fulfilment of the research objectives and their implications for the current literature is given. Secondly, an evaluation of the applicability of the results to other cases is given. Third, the limitations and uncertainties of the research are discussed. Finally, the implications of the findings for the dutch erosion prevention program is discussed.

7.1. ADDITION TO LITERATURE

DATA COLLECTION

In the process of this thesis, the most extensive wave data set as of known was collected on top of an artificial large scale oyster reef in the field. Instead of the typically just two pressure gauges allocated per reef (as in Chauvin 2018, Wiberg et al. 2018 etc.), measurements were done at seven locations along a transect, including pressure gauges at each location, two ADVs and one ADCP. This setup allows for a far more detailed analysis than usual practised: The long and dense measurement transect enables to follow the wave trajectory more closely, giving insight about where waves are attenuated. The velocity data gives insight into currents around the reef and wave directions. The long measurement period of nearly three months during the winter period enabled the capture of several storm events, containing a large variety of wave characteristics. Thus the data set holds large potential for additional future research, especially regarding the velocity data, of which only basic elements were used.

The raw collected data is made freely available on the 4TU.ResearchData repository and can be found via the DOI 10.4121/14916612 .

QUANTIFICATION OF RESULTS

The wave attenuation was quantified on several sections of the measurement transect. Generally, attenuation over the reef was found until a water depth of 2 m (measured from the reef) and a $d_s/H_{m0,i}$ ratio of 4. Comparing the attenuation of the reef to the attenuation of the tidal flat a dissipation rate of on average 18 times higher was found. Comparing these values to literature, the reef showed similar, or slightly higher attenuation values than the crushed whelk shell reef observed in Wiberg et al. 2018 which shows

comparable reef dimensions to the present case. The oyster castles observed in Chauvin 2018, on the other hand, attenuated waves much less effective than the observed oyster reef.

The footprint of the reef, where reduced wave energy was measured, reached up to 300 m leeward of the reef. At this distance, the effect of the reef is limited though. The stretch where no wave energy reaching the bed was detected reaches until approximately 110 m behind the reef. Generally, the distance until which reduced wave heights were measured is approximately of the same order of magnitude as the reef length. Such a relation was also found by Walles, Salvador de Paiva, et al. 2014, where reef length was identified as the dominating factor determining the area of reduced erosion.

Overtopping, reflection, wave breaking and reef friction were found to dominate the attenuation over the reef. Most important was hereby wave breaking, which was present until a $d_s/H_{m0,i}$ value of approximately 2. Above $d_s/H_{m0,i} > 2$, friction dominates the wave attenuation. This indicates that the reef width B and the surface roughness play an important role in how much energy is attenuated. At $d_s/H_{m0,i} < 0$ reflection and overtopping becomes dominant. The reflection hereby may lead to increased erosion in front of the reef. An indication of this erosion was found in the reef transects (figure 3.7).

CONCEPTUALISATION

The findings regarding the footprint of the reef and the conditionality of attenuation were conceptualised in figure 6.11. This figure gives an insight on the attenuation process at different $d_s/H_{m0,i}$ ratios, and the implications on the footprint. This conceptualisation is mainly valid for wind waves in a macrotidal environment. The presence of only swell waves would simplify the concept. Swell waves are a lot more unidirectional and no or only little wind input can be expected. The footprint of the reef would thus increase. The concept furthermore assumes that behind the reef the tidal flat extends for at least a couple hundred of meters before the marsh edge begins. If the reef is located closer to the coast or marsh, such as < 100 m, the influence of wind input or the concept of a footprint is less important.

PARAMETERIZATION

A parameterization is the first step to develop relations that are valid for a variety of cases. This was done by using dimensionless numbers which describe the distribution of transmission coefficients. The factor $d_s/H_{m0,i}$ is the typical used dimensionless number in literature to best describe attenuation over a structure (Van der Meer et al. 2005, Seabrook and Hall 1998). These authors furthermore link $d_s/H_{m0,i}$ to the attenuation process wave attenuation. This could be confirmed by the strong dependence found between $d_s/H_{m0,i}$ and the wave asymmetry (figure 6.8).

In figure 6.12 it was shown that $d_s/H_{m0,i}$ describes the transmission well for $d_s/H_{m0,i}$ values around 0 but leads to an increasing spread with higher $d_s/H_{m0,i}$ values. Thus this factor represents overtopping, reflection and wave breaking reasonably well. The spread for higher $d_s/H_{m0,i}$ values could partly be parameterized by using the incident wave height (independently of the freeboard) and the wave steepness. The usage of the

wavelength L present in the steepness is likely capable of representing the reef friction, which becomes dominant for $d_s/H_{m0,i} > 2$. However, somehow the reef width B will need to be included to properly represent friction. The exact relevance of the width B of the reef could not be quantified since measurements were only done on one reef and reference data is missing. To reduce such uncertainties it would be desirable to collect a larger data set, including several similar oyster reef structures with different dimensions.

In literature the relative submergence $d_s/H_{m0,i}$ is predominantly used as the main parameter relating the transmission coefficient to structure and wave parameters (see Seabrook and Hall 1998, Van der Meer and Daemen 1994). In this thesis, however, the dimensionless parameter $d_s/L_{01,i}$ performed better in describing transmission. This parameter thus might be better suited than the relative submergence in empirical relations. Should a new relation regarding oyster reefs be developed, it is thus suggested that the performance of $d_s/L_{01,i}$ in combination with other parameters is explored.

PERFORMANCE OF EMPIRICAL RELATIONS

As of now the quantitative impacts of an artificial oyster reef on its surroundings are unknown prior to construction. Finding a relation that can represent wave attenuation over oyster reefs would fill this knowledge gap, making oyster reefs a more attractive option for erosion prevention programs.

The examined oyster reef has similarities to classical breakwaters. Thus several existing relations for submerged breakwaters were used in an attempt to reproduce the results of the measurement campaign. Without any tuning all three relations resulted in large root mean square errors (RMSE), meaning poor predictability. However, generally high correlation factors of around 0.9 were found. This indicates that the processes governing attenuation over the oyster reef are similar to the processes in submerged breakwaters. It was possible to achieve significantly lower RMSE values by changing the definition of the reef width B and the reef height h_s. However, it is unclear if the same definition would be valid for other cases.

Generally, the equations react quite sensitive to a change in the reef height h_s. This is because of the very low structure height of the oyster reef, where small deviations in the order of cm lead to large relative differences. A change of h_s = 10 cm can e.g. lead to a change of the RMSE of 0.1 in the prediction of the transmission coefficient. This complicates the evaluation of the attenuation capabilities of an oyster reef prior to construction since the reef may grow or degrade, leading to the reef height varying significantly both in space and in time.

With a larger data set it is likely that the existing empirical relations can be modified to represent gabion oyster reefs. This is in contrast to findings about oyster castles, where Webb and Allen 2015 concludes that existing empirical relations do not sufficiently represent the observed oyster reefs. However, regarding the uncertainty of where the growth ceiling of the oyster reef is and the inhomogeneity of the structure dimensions, both in space and in time, a precise prediction of attenuation will be difficult to achieve.

APPLICABILITY TO OTHER CASES

As of known, this study is the only one researching wave dissipation over an oyster reef in a macrotidal low energy environment. Thus, many effects not present in existing literature could be observed, especially regarding the fluctuating water depths due to the large tidal range. The conditionality of the wave attenuation due to this large water depth range was schematized. This schematization is likely applicable to all cases in macrotidal systems and can give insight into the basic processes. However, results regarding the quantification of attenuation should be transferred to other cases with care. Especially to oyster castles, the found results show little concordance. This can likely be traced back to a much larger relative reef width B/L of the gabion reef and fragmentary building styles in many oyster castle structures. In what sense the quantification of the results is applicable to other oyster gabions, has still to be researched. Additional data on other reefs with a similar building structure are required to identify the impact of different reef dimensions and biotic factors such as oyster sizes and oyster density. Recommended is also a comparison to data on natural oyster reefs. These are typically much wider and can provide insight on the importance of the reef width B. Since friction was found to be important for dissipation in this thesis, especially for higher water depths, such an increased width is likely gonna increase both the general dissipation and the spatial footprint of the reef.

LIMITATIONS OF THE RESULTS REGARDING EROSION EVALUATION

The results give a deep insight into the wave attenuation processes over the oyster reef. However, no direct quantification of the erosion reduction was done. Consequently, some processes induced by the reef which are not directly relevant for wave attenuation but might alter erosion quantities were not covered.

One of these processes is reef induced currents. During flood and ebb, when the water level is at around reef height, the reef strongly obstructs the natural flow of the water onto, or away from the reef. This might lead to currents alongside the reef which can lead to erosion.

The reef can furthermore decrease the period of waves that propagate over it due to harmonic release. Since smaller periods are linked to smaller wavelengths, wave energy may penetrate less deep into the water column. Such an effect was observed in the measurement data (see A.9) but not discussed further.

IMPLICATIONS FOR THE DUTCH EROSION PREVENTION SCHEME

The results show that the reef is successful in disrupting the incoming waves and protecting the area leeward of the reef. However, the area of influence of the reef is limited. Much of the tidal flat further inland experiences no reduced wave energy and thus also no reduced erosion. This is in concordance with the findings in Walles, Salvador de Paiva, et al. 2014. Furthermore, some erosion in direct proximity behind the reef could still be measured, although with slowed down rates. Generally, the applicability of constructing artificial oyster reefs on tidal flats is limited due to strict requirements in biotic and abiotic factors which are only met on parts of tidal flats. The usage of oyster reefs can thus only be seen as a local, complementary measure for erosion reduction, which

in most cases can only delay, but not prevent more disruptive measures such as nourishments.

8

CONCLUSION

Within this thesis work, an extensive data set was collected to research the attenuation capabilities of an artificial gabion oyster reef. Using the data set wave attenuation was quantified and relevant processes were identified. It was then investigated how and if empirical relations could predict attenuation quantities over such a structure. The conclusion regarding the three objectives and the main research question is addressed below.

OBTAIN A COMPREHENSIVE AND EXTENSIVE DATA SET WITH MEASUREMENTS OF WAVE CHARACTERISTICS AT THE OBSERVED OYSTER REEF.

Despite the challenging environment at the research site due to a large tidal range, an extensive and high-quality data set could be collected. The obtained velocity and pressure data were sufficient to execute a complete and extensive analysis of wave attenuation. The data set was further not fully exploited and leaves much room for additional research in the future.

QUANTIFY THE WAVE ATTENUATION AND IDENTIFY THE PROCESSES WHICH GOVERN THE MODIFICATION OF WAVES OVER THE OBSERVED OYSTER REEF.

The attenuation process over the oyster reef was successfully quantified for different conditions. Compared to the bare tidal flat the reef featured a dissipation rate of on average 18 times higher. The usage of the energy flux instead of the wave height to define the transmission hereby enabled more accurate results than common in research.

For attenuation, the mechanisms of reflection, overtopping, wave breaking and reef friction were identified to be most relevant. By investigating the relative significance of these mechanisms for different conditions, implications on the importance of certain reef characteristics under different conditions could be made.

PARAMETERIZE THE EFFECT OF THE MODIFICATION OF THE WAVE FIELD BY THE OYSTER REEF AND INVESTIGATE POTENTIAL PREDICTABILITY.

The attenuation process was parameterized using dimensionless numbers. The general results hereby show strong resemblance to parameterizations of submerged rubble

mound breakwaters, indicating similarity of these two structure types. The best parameters to represent attenuation over the oyster reef were found to be the freeboard in relation to the incoming wave height, and the freeboard in relation to the incoming wavelength.

Existing empirical relations describing submerged rubble mound breakwaters were found to reasonably well represent attenuation over the oyster reef. However, quantitative data for calibration is still missing. The small reef height in regards to the tidal range, further makes the equations extremely sensitive to the reef height. Because of the inhomogeneity of oyster reefs, there will thus always be a limit to the accuracy of predictions.

HOW EFFECTIVE CAN AN ARTIFICIAL OYSTER REEF GABION CONTRIBUTE TO EROSION PREVENTION ON A MACROTIDAL FLAT BY ATTENUATING WAVES?

The results prove that oyster reef gabions in a macrotidal and low energy environment can be effective in reducing wave energy leeward of the reef. However, the efficacy of the reef in attenuating waves varies greatly with tidal elevation, showing full transmission for water depths > 2m. Furthermore, the footprint of the reef where reduced wave energy was measured was limited to a maximum of about 300 m behind the reef.

These limitations were generalized in a concept figure, where the conditionality of attenuation for different forcing and the implications for the reef footprint are visualised.

Overall the oyster reef showed a strong local effect on its surroundings. However, depending on the size of the intertidal area behind the reef, only a fraction of the lee-side flat may be influenced by the reef. On large intertidal areas, oyster reefs should thus not be considered as an adequate general solution for erosion prevention, but rather as a spatially limited instrument to locally reduce erosion.

9

RECOMMENDATIONS FOR FUTURE RESEARCH

Based on the findings several actions are recommended to further research:

- Much of the available velocity data was not used, or only used briefly. Analysing the ADV and ADCP data could give insights into the tidal currents on the flat and how the reef obstructs these. Furthermore, the reflected wave energy could be quantified. These processes could possibly be linked to added erosion around the reef which is not covered in the attenuation analysis made in this thesis.
- In this thesis only the capability of the observed oyster reef to attenuate waves was verified. To construct a formal link to the actual reduced erosion quantities, the set-up and calibration of a numerical model is recommended with the collected data. Going further, a numerical model could explore the effect of a more extensive usage of oyster reefs on the tidal flat, investigating the limit to which oyster reefs can reduce erosion.
- In order to develop a simple tool to estimate the effect of such oyster reefs the collection of a quantitative data set including transmission data of a variety of oyster gabion reefs with different dimensions and hydraulic forcing is recommended. As shown in this thesis, such a data set could likely be used to develop, or transform a existing empirical relation to estimate attenuation quantities
- The oyster reef has been shown to reduce the wave forcing and locally stabilize the surrounding flat. It is thus recommended to extend the research project and build further oyster reefs at strategical relevant locations. To increase the impact of such projects oyster reefs could be investigated alongside other erosion mitigation measures.

BIBLIOGRAPHY

Aguilera, Moisés A., Jan Tapia, Camila Gallardo, Pamela Núñez, and Katerina Varas-Belemmi (2020). "Loss of coastal ecosystem spatial connectivity and services by urbanization: Natural-to-urban integration for bay management". In: *Journal of Environmental Management* 276, p. 111297. ISSN: 0301-4797. DOI: https://doi.org/10.1016/j.jenvman.2020.111297. URL: http://www.sciencedirect.com/science/article/pii/S0301479720312214.

Beck, Michael W., Robert D. Brumbaugh, Laura Airoldi, Alvar Carranza, Loren D. Coen, Christine Crawford, Omar Defeo, Graham J. Edgar, Boze Hancock, Matthew C. Kay, Hunter S. Lenihan, Mark W. Luckenbach, Caitlyn L. Toropova, Guofan Zhang, and Ximing Guo (Feb. 2011). "Oyster Reefs at Risk and Recommendations for Conservation, Restoration, and Management". In: *BioScience* 61.2, pp. 107–116. ISSN: 0006-3568. DOI: 10.1525/bio.2011.61.2.5. eprint: https://academic.oup.com/bioscience/article-pdf/61/2/107/19406950/61-2-107.pdf. URL: https://doi.org/10.1525/bio.2011.61.2.5.

Borsje, B.W., Bregje Van Wesenbeeck, Frank Dekker, Peter Paalvast, Tjeerd Bouma, Marieke Katwijk, and Mindert de Vries (Feb. 2011). "How ecological engineering can serve in coastal protection". In: *Ecological Engineering* 37, pp. 113–122. DOI: 10.1016/j.ecoleng.2010.11.027.

Bosboom, J and M Stive (2015). "Coastal Dynamics I". In: ISBN: 9789065623720.

Chauvin, Jason (2018). "Wave Attenuation by Constructed Oyster Reef Breakwaters". In:

Climate Stavenisse (Jan. 2021). URL: https://www.meteoblue.com/en/weather/historyclimate/climatemodelled/stavenisse_netherlands_2746823.

Coen, Loren, Robert Brumbaugh, David Bushek, Raymond Grizzle, Mark Luckenbach, Martin Posey, Sean Powers, and S Gregory Tolley (July 2007). "As we see it. A broader view of ecosystem services related to oyster restoration". In: *Marine Ecology Progress Series* 341, pp. 303–307. DOI: 10.3354/meps341303.

Costanza, Robert, Ralph d'Arge, Rudolf de Groot, Stephen Farber, Monica Grasso, Bruce Hannon, Karin Limburg, Shahid Naeem, Robert V. O'Neill, Jose Paruelo, Robert G. Raskin, Paul Sutton, and Marjan van den Belt (1998). "The value of the world's ecosystem services and natural capital". In: *Ecological Economics* 25.1, pp. 3–15. ISSN: 0921-8009. DOI: https://doi.org/10.1016/S0921-8009(98)00020-2. URL: http://www.sciencedirect.com/science/article/pii/S0921800998000202.

Currin, Carolyn A. (2019). "Chapter 30 - Living Shorelines for Coastal Resilience". In: *Coastal Wetlands*. Ed. by Gerardo M.E. Perillo, Eric Wolanski, Donald R. Cahoon, and Charles S. Hopkinson. Elsevier, pp. 1023–1053. ISBN: 978-0-444-63893-9. DOI: https://doi.org/10.1016/B978-0-444-63893-9.00030-7. URL: http://www.sciencedirect.com/science/article/pii/B9780444638939000307.

d'Angremond, Kees, Jentsje W. Van Der Meer, and Rutger J. De Jong (Jan. 1996). "WAVE TRANSMISSION AT LOW-CRESTED STRUCTURES". In: *Coastal Engineering Proceed-*

ings 1.25. DOI: 10.9753/icce.v25.. URL: https://icce-ojs-tamu.tdl.org/icce/index.php/icce/article/view/5401.

de Vet, P.L.M. (2020). "Intertidal Flats in Engineered Estuaries: On the Hydrodynamics, Morphodynamics, and Implications for Ecology and System Management". In: DOI: https://doi.org/10.4233/uuid:2b392951-3781-4aed-b093-547c70cc581d.

de Vet, P.L.M., B.C. van Prooijen, and Z.B. Wang (2017). "The differences in morphological development between the intertidal flats of the Eastern and Western Scheldt". In: *Geomorphology* 281, pp. 31–42. ISSN: 0169-555X. DOI: https://doi.org/10.1016/j.geomorph.2016.12.031. URL: https://www.sciencedirect.com/science/article/pii/S0169555X16303002.

Dorsch, Christian (2012). "The potential of artificial oyster reefs as coastal protection in the Oosterschelde (Master thesis)". English. (not published). PhD thesis.

Drinkward, A.C. (1998). "Introductions and developments of oysters in the North Sea area: a review." In: *Helgolander Meeresunters 52, 301-308.* DOI: https://doi.org/10.1007/BF02908904.

ecoshape (2021). *Oyster reefs.* URL: https://www.ecoshape.org/en/pilots/oyster-reefs/ (visited on 01/28/2021).

Emergo (2021). *unpublished, PhD Lodewijk de Vet.* URL: https://emergoproject.wordpress.com/over/ (visited on 01/28/2021).

Engineering ToolBox (2005). *Properties of Seawater. [online].* URL: https://www.engineeringtoolbox.com/sea-water-properties-d_840.html (visited on 01/28/2021).

Fisheries, NOAA (July 2020). *Oyster Reef Habitat.* URL: https://www.fisheries.noaa.gov/national/habitat-conservation/oyster-reef-habitat.

Google Earth Pro 7.3.3 (2020). (Visited on 01/28/2021).

Gornitz, Vivien (1991). "Global coastal hazards from future sea level rise". In: *Palaeogeography, Palaeoclimatology, Palaeoecology* 89.4, pp. 379–398. ISSN: 0031-0182. DOI: https://doi.org/10.1016/0031-0182(91)90173-O. URL: https://www.sciencedirect.com/science/article/pii/0031018291901730.

Hallegatte, Stéphane, Colin Green, Robert Nicholls, and Jan Corfee-Morlot (Sept. 2013). "Future flood losses in major coastal cities". In: *Nature Climate Change* 3, pp. 802–806. DOI: 10.1038/nclimate1979.

Henderson, Stephen M., R. T. Guza, Steve Elgar, and T. H. C. Herbers (2006). "Refraction of Surface Gravity Waves by Shear Waves". In: *Journal of Physical Oceanography* 36.4, pp. 629–635. DOI: 10.1175/jpo2890.1.

Herbers, T. H. C., Steve Elgar, and R. T. Guza (1999). "Directional spreading of waves in the nearshore". In: *Journal of Geophysical Research: Oceans* 104.C4, pp. 7683–7693. DOI: 10.1029/1998jc900092.

Holthuijsen, L.H. (2009). *Waves in Oceanic and Coastal Waters.* Cambridge University Press. URL: https://books.google.de/books?id=QudIyQEACAAJ.

Jones, Clive, John Lawton, and Moshe Schachak (Apr. 1994). "Jones CG, Lawton JH, Shachak M.. Organisms as ecosystem engineers. Oikos 69: 373-386". In: *Oikos* 69, pp. 373–386. DOI: 10.2307/3545850.

Kala, Yahia (2016). "Wave attenuation over the Oesterdam tidal flat nourishment: Wind-wave transformation in the intertidal zone". English. PhD thesis. URL: http://resolver.tudelft.nl/uuid:90f1036f-40dd-43f5-bc98-bbd0f433551f.

Karimpour, Arash and Qin Chen (2017). "Wind wave analysis in depth limited water using OCEANLYZ, A MATLAB toolbox". In: *Computers Geosciences* 106, pp. 181–189. ISSN: 0098-3004. DOI: https://doi.org/10.1016/j.cageo.2017.06.010. URL: https://www.sciencedirect.com/science/article/pii/S0098300417306489.

Kater, Belinda and J.M.D.D. Baars (Dec. 2004). "The potential of aerial photography for estimating surface areas of intertidal Pacific oyster beds (Crassostrea gigas)". In: *Journal of Shellfish Research 23 (2004) 3* 23.

Kirby, Michael Xavier (2004). "Fishing down the coast: Historical expansion and collapse of oyster fisheries along continental margins". In: *Proceedings of the National Academy of Sciences* 101.35, pp. 13096–13099. ISSN: 0027-8424. DOI: 10.1073/pnas.0405150101. eprint: https://www.pnas.org/content/101/35/13096.full.pdf. URL: https://www.pnas.org/content/101/35/13096.

La Peyre, Megan (Jan. 2017). "Comparison of Oyster populations, shoreline protection service, and site characteristics at seven created fringing reefs in Louisiana: Key parameters and responses to consider". In: pp. 363–382. ISBN: ISBN 9781498740036.

MATLAB (2015). *version 7.10.0 (R2015b)*. Natick, Massachusetts: The MathWorks Inc.

Moody, Ryan, Just Cebrian, SM Kerner, Ken Heck, SP Powers, and Carl Ferraro (Aug. 2013). "Effects of shoreline erosion on salt-marsh floral zonation". In: *Marine Ecology Progress Series* 488, pp. 145–155. DOI: 10.3354/meps10404.

Mouragues, A., P. Bonneton, D. Lannes, B. Castelle, and V. Marieu (2019). "Field data-based evaluation of methods for recovering surface wave elevation from pressure measurements". In: *Coastal Engineering* 150, pp. 147–159. ISSN: 0378-3839. DOI: https://doi.org/10.1016/j.coastaleng.2019.04.006. URL: https://www.sciencedirect.com/science/article/pii/S0378383919300183.

Neumann, Barbara, Athanasios Vafeidis, Juliane Zimmermann, and Robert Nicholls (Mar. 2015). "Future Coastal Population Growth and Exposure to Sea-Level Rise and Coastal Flooding - A Global Assessment". In: *PLoS ONE* 10. DOI: 10.1371/journal.pone.0118571.

Neumeir, Urs (2006). *Properties of Seawater. [online]*. URL: http://neumeier.perso.ch/matlab/waves.html (visited on 04/21/2021).

Nienhuis, PH and AC Smaal (1994). "The Oosterschelde estuary, a case-study of a changing ecosystem: an introduction." In: *Hydrobiologia 282, 1–14*. DOI: 10.1007/BF00024616.

Nortek (2021). URL: https://www.nortekgroup.com/.

ocean sensors (2021). URL: http://www.oceansensorsystems.com/.

Pereira, Daniel (2021). *Wind Rose*. MATLAB Central File Exchange. Retrieved July 8, 2021. URL: https://www.mathworks.com/matlabcentral/fileexchange/47248-wind-rose.

Rijkwaterstaat (2021). URL: https://waterinfo.rws.nl/#!/nav/index/.

Rodriguez, Antonio, F. Fodrie, Justin Ridge, Niels Lindquist, Ethan Theuerkauf, Sara Coleman, Jonathan Grabowski, Michelle Brodeur, Rachel Gittman, Danielle Keller, and Matthew Kenworthy (Apr. 2014). "Oyster reefs can outpace sea-level rise". In: *Nature Climate Change* 4. DOI: 10.1038/NCLIMATE2216.

Salvador de Paiva, João N., Brenda Walles, Tom Ysebaert, and Tjeerd J. Bouma (2018). "Understanding the conditionality of ecosystem services: The effect of tidal flat morphology and oyster reef characteristics on sediment stabilization by oyster reefs". In:

Ecological Engineering 112, pp. 89–95. ISSN: 0925-8574. DOI: https://doi.org/10.1016/j.ecoleng.2017.12.020. URL: http://www.sciencedirect.com/science/article/pii/S0925857417306535.

Scyphers, Steven B., Sean P. Powers, Kenneth L. Heck Jr, and Dorothy Byron (Aug. 2011). "Oyster Reefs as Natural Breakwaters Mitigate Shoreline Loss and Facilitate Fisheries". In: *PLOS ONE* 6.8, pp. 1–12. DOI: 10.1371/journal.pone.0022396. URL: https://doi.org/10.1371/journal.pone.0022396.

Seabrook, SR and KR Hall (1998). "ave transmission at submerged rubble mound breakwaters." In: *Proc. 26th Int. Conf. on Coastal Engineering, ASCE, pp. 2000–2013.*

Shi, Peijun and Roger Kasperson (Jan. 2015). *World Atlas of Natural Disaster Risk*. ISBN: 978-3-662-45429-9. DOI: 10.1007/978-3-662-45430-5.

Smaal, AC, Belinda Kater, and Jeroen Wijsman (Mar. 2009). "Introduction, establishment and expansion of the Pacific oyster in the Oosterschelde (SW Netherlands)". In: *Helgoland Marine Research* 63, pp. 75–83. DOI: 10.1007/s10152-008-0138-3.

Srineash, VK and Kantharaj Murali (Aug. 2019). "Functional performance of modular porous reef breakwaters". In: *Journal of Hydro-environment Research*, pp. 20–31. DOI: 10.1016/j.jher.2019.07.006.

Temmerman, Stijn, Patrick Meire, Tjeerd Bouma, Peter Herman, Tom Ysebaert, and Huib de Vriend (Dec. 2013). "Ecosystem-based coastal defence in the face of global change". In: *Nature* 504, pp. 79–83. DOI: 10.1038/nature12859.

Troost, Karin (2009). "Pacific oysters in Dutch estuaries: Causes of success and consequences for native bivalves". English. Relation: https://www.rug.nl/ Rights: University of Groningen. PhD thesis. ISBN: 9789036740340.

Van der Meer, Jentsje, R. Briganti, Barbara Zanuttigh, and Baoxing Wang (Nov. 2005). "Wave transmission and reflection at low-crested structures: Design formulae, oblique wave attack and spectral change". In: *Coastal Engineering* 52, pp. 915–929. DOI: 10.1016/j.coastaleng.2005.09.005.

Van der Meer, Jentsje and IFR Daemen (1994). "Stability and Wave Transmission at low crested rubble mound structures". In: *Journal of Waterway, Port, Coastal, and Ocean Engineering* 120.1, pp. 1–19. DOI: https://doi.org/10.1061/(ASCE)0733-950X(1994)120:1(1).

Vriend, Huib de, Mark van Koningsveld, and Stefan Aarninkhof (Feb. 2014). "'Building with nature': The new Dutch approach to coastal and river works". In: *ICE Proceedings Civil Engineering* 167, pp. 18–24. DOI: 10.1680/cien.13.00003.

Wall, Charles C., Bradley J. Peterson, and Christopher J. Gobler (2011). "The Growth of Estuarine Resources (Zostera marina, Mercenaria mercenaria, Crassostrea virginica, Argopecten irradians, Cyprinodon variegatus) in Response to Nutrient Loading and Enhanced Suspension Feeding by Adult Shellfish". In: *Estuaries and Coasts* 34.6, pp. 1262–1277. ISSN: 15592723, 15592731. URL: http://www.jstor.org/stable/41333022.

Walles, Brenda, Roger Mann, Tom Ysebaert, Karin Troost, Peter Herman, and A.C. Smaal (Jan. 2015). "Demography of the ecosystem engineer Crassostrea gigas, related to vertical reef accretion and reef persistence". In: *Estuarine, Coastal and Shelf Science* 154. DOI: 10.1016/j.ecss.2015.01.006.

Walles, Brenda, João Salvador de Paiva, B. Prooijen, Tom Ysebaert, and A.C. Smaal (May 2014). "The Ecosystem Engineer Crassostrea gigas Affects Tidal Flat Morphology Be-

yond the Boundary of Their Reef Structures". In: *Estuaries and Coasts* 38. DOI: 10.1007/s12237-014-9860-z.

Walles, Brenda, Karin Troost, Douwe Ende, Sil Nieuwhof, AC Smaal, and Tom Ysebaert (Feb. 2016). "From artificial structures to self-sustaining oyster reefs". In: *Journal of Sea Research* 108, pp. 1–9. DOI: 10.1016/j.seares.2015.11.007.

Webb, B and R Allen (2015). "Wave Transmission through Artificial Reef Breakwaters". In: *Coastal Structures and Solutions to Coastal Disasters 2015*, pp. 432–441. DOI: 10.1061/9780784480304.046. eprint: https://ascelibrary.org/doi/pdf/10.1061/9780784480304.046. URL: https://ascelibrary.org/doi/abs/10.1061/9780784480304.046.

Wiberg, Patricia, Sara Taube, Amy Ferguson, Marnie Kremer, and Matthew Reidenbach (Sept. 2018). "Wave Attenuation by Oyster Reefs in Shallow Coastal Bays". In: *Estuaries and Coasts* 42. DOI: 10.1007/s12237-018-0463-y.

WorldBank (2021). URL: https://www.worldbank.org/en/topic/oceans-fisheries-and-coastal-economies#1.

Ysebaert, Tom, Brenda Walles, Judy Haner, and Boze Hancock (2019). "Habitat Modification and Coastal Protection by Ecosystem-Engineering Reef-Building Bivalves". English. In: *Goods and Services of Marine Bivalves*. Ed. by Aad C. Smaal, Joao G. Ferreira, Jon Grant, Jens K. Petersen, and Øivind Strand. Springer International Publishing, pp. 253–273. ISBN: 9783319967752. DOI: 10.1007/978-3-319-96776-9_13.

Zhu, Linham X, Nicholls MM, and R J (Nov. 2010). *Technologies for climate change adaptation. Coastal erosion and flooding.*

A

APPENDIX

A.1. INSTRUMENTS

A.1.1. OSSIs

Below the most important technical data of the used OSSI pressure gauges is laid out. The full information can be found on *ocean sensors* 2021

General Description
The OSSI-010-003B/C Wave Gauge combines a highly stable Pressure Sensor, a Compact Flash Card Data Logger, a rugged waterproof package and 12 or 28 C size Alkaline Batteries. A Low Power Microprocessor records up to 2 Gigabytes of data on a Compact Flash Card in an ASCII or Binary format with time and date. Then the Card is easily removed and can be read on any PC with a standard Compact Flash Card Reader. The Logger will collect months of continuous data or years of burst data. A serial port is provided as a user interface to configure and monitor the Wave Gauge. Standard pressure ranges are 0 to 1 Bar, 0 to 3 Bars and 0 to 10 Bars.

Features

- **Standard Compact Flash Card Data Storage**
- **Data storage up to 2 Gigabytes**
- **Standard Card Reader Compatible**
- **Power with 12 or 28 C Size Alkaline Batteries**
- **Flush Hastelloy Diaphragm**
- **ABS Plastic Housing Rated to 100 Meters**
- **Months of Continuous Operation**
- **Years of Burst Operation**
- **Rugged Sealed Waterproof Design**
- **Fully Programmable via RS232**
- **PC Interface Software**
- **Binary or ASCII Data Format**
- **Sample Rate From 2 Hz to 30Hz**
- **Burst or Continuous Sampling**
- **Accuracy ± 0.05% FS, 10 to 40 °C**
- **Resolution 0.0033%FS**
- **Long Term Stability ± 0.05%FS**
- **Optional Water Temperature Logging**

Figure A.1: General information OSSI wave gauge. *ocean sensors* 2021

A

Electrical Characteristics

Parameter	Conditions	Min.	Typ.	Max.	Units
Battery Voltage	6 V, 12 cell battery	3.6	6.0	7.0	VDC
	18V, 12 cell battery (4)	9	18	35	VDC
	21V, 28 cell battery (3)	9	21	35	VDC
Temperature Range		-10		65	°C
Battery Drain, Sleep Mode	6 V battery Pack		3		mW
	18V battery Pack (4)		3.4		mW
	21 V battery Pack (3)		3.5		mW
Battery Drain	Sleep mode with RS232 Monitoring (1)		15.0		mW
Battery Drain, Continuous Sampling	6 V battery Pack		74.0		mW
	18V battery Pack (4)		65.2		mW
	21 V battery Pack (3)		66.2		mW
Battery Drain	Continuous Sampling with RS232 Monitoring (1)		90.0		mW
Battery Type, See schematic below	Alkaline 6V		12		C Cells
	Alkaline 18V		12		C Cells
	Alkaline 21V		28		C Cells
Battery Life Continuous Sampling	6 V battery Pack		2.5		Month
	18V battery Pack (4)		3.0		Month
	21 V battery Pack (3)		6.5		Month
Battery Life 25% Sample (2)	6 V battery Pack		8.5		Month
	18V battery Pack (4)		9.7		Month
	21 V battery Pack (3)		21.7		Month
Battery Life 10% Sample (2)	6 V battery Pack		16.7		Month
	18V battery Pack (4)		17.8		Month
	21 V battery Pack (3)		40.3		Month

(1) Powered up External Monitoring PC connected to RS232 Serial port.
(2) Industrial Alkaline Batteries 12 C cells totaling 102 Watt hr. Typ. or 28 calls totaling 238 Watt hr. Typ.
(3) Only available with the extended Wave Gauge case (Identified with the letter E at the end of the Wave Gauge part number)
(4) Version C Wave Gauge only

Figure A.2: Electrical Characteristics OSSI wave gauge. *ocean sensors* 2021

Data Characteristics, Pressure

Parameter	**Conditions**	Min.	Typ.	Max.	**Units**
Pressure Numeric (4) Format & Units	OSSI-010-003C-01			+.99999	Bars
Pressure Numeric Format & Units	OSSI-010-003C-03			+3.0000	Bars
Pressure Numeric Format & Units	OSSI-010-003C-10			+9.9999	Bars
Data Accuracy (1)(2)(3)	10 to 40 °C			0.05	±% FS
Data Accuracy (1)(2)(3)	-10 to 65 °C			0.1	±% FS
Data Resolution			0.0033		% FS
Long Term Stability	OSSI-010-003C-01		0.0005		Bar
Long Term Stability	OSSI-010-003C-03, -10		0.05		% FS

(1) Linearity + Hysteresis + Repeatability + Temperature Coefficients + Zero + Span Tolerance
(2) Accuracy and Resolution are valid for Basic Pressure Range
(3) Linearity: Best Straight Line
(4) The 1 bar unit data format when over full scale (greater than +.99999) reads 1.00000 to 1.25000

Figure A.3: Data Characteristics, Pressure, OSSI. *ocean sensors* 2021

A

A.1.2. ADV

The used User setup is given in A.4.

```
User setup
-----------------------------------------------------------------------
Sampling rate                          8 Hz
Nominal velocity range                 1.00 m/s
Burst interval                         1800 sec
Samples per burst                      7200
Sampling volume                        14.9 mm
Measurement load                       59 %
Transmit length                        4.0 mm
Receive length                         0.01 m
Output sync                            VECTOR
Analog output                          DISABLED
Analog input 1                         NONE
Analog input 2                         NONE
Power output                           DISABLED
Output format                          VECTOR
Velocity scaling                       1 mm
IMU mode                               OFF
IMU data type                          AHRSC3
IMU Mag digital filter size            17
IMU Gyro/Accel digital filter size     15
Powerlevel                             LOW+
Coordinate system                      XYZ
Sound speed                            MEASURED
Salinity                               32.0 ppt
Distance between pings                 1.01 m
Number of beams                        3
Software version                       1.39.09
Deployment name                        Oyste1
Wrap mode                              OFF
Deployment time                        16.12.2020 12:00:00
```

Figure A.4: Used configurations for the ADVs

Below the most important technical data of the used ADVs is laid out. The full information can be found on *Nortek* 2021

Technical specifications

⟶ Water velocity measurements	
Maximum profiling range	N/A
Distance from probe	0.15 m
Sampling volume diameter	15 mm
Sampling volume height (user-selectable)	5-20 mm
Cell size	N/A
Velocity range	±0.01, 0.1, 0.3, 1, 2, 4, 7 m/s (software-selectable)
Adaptive ping interval	N/A
Accuracy	±0.5% of measured value ±1 mm/s
Velocity precision	typ. 1% of velocity range (at 16 Hz)
Sampling rate (output)	1-64 Hz
Internal sampling rate	100-250 Hz
⟶ Distance measurements	
Minimum range	N/A
Maximum range	N/A
Cell size	N/A
Accuracy	N/A
Sampling rate	N/A
⟶ Echo intensity	
Acoustic frequency	6 MHz
Resolution	0.45 dB
Dynamic range	90 dB
⟶ Sensors	
Temperature:	Thermistor embedded in end bell
Temp. range	-4 to +40 °C
Temp. accuracy/resolution	0.1 °C/0.01 °C
Temp. time response	10 min

Figure A.5: Technical data ADV 1. *Nortek* 2021

A

⟶ Sensors	
Compass:	Magnetometer
Accuracy/resolution	2°/0.1° for tilt < 20°
Tilt:	Liquid level
Accuracy/resolution	0.2°/0.1°
Maximum tilt	30°
Up or Down	Automatic detect
Pressure:	Piezoresistive
Standard range	0-20 m (inquire for options)
Accuracy/precision	0.5% FS / Better than 0.005% of full scale
⟶ Analog inputs	
No. of channels	2
Supply voltage to analog output devices	Three options selectable through firmware commands:1) Battery voltage/500 mA, 2) +5 V/250 mA, 3) +12 V/100 mA
⟶ Data recording	
Capacity (standard):	9 MB, can add 4/16 GB
Data record (Standard)	24 bytes at sampling rate + 28 bytes/second
Data record (IMU)	72 bytes at sampling rate
⟶ Real-time clock	
Accuracy	±1 min/year
Backup in absence of power	4 weeks

Figure A.6: Technical data ADV 2. *Nortek* 2021

⟶ Data communications	
I/O	RS-232 or RS-422
Communication baud rate	300-115 200 Bd
Recorder download baud rate	600/1200 kBd for both RS-232 and RS-422
User control	Handled via "Vector" software, ActiveX® function calls, ordirect commands.
Analog outputs	3 channels standard, one for each velocity component or two velocities and pressure.
Output range	0–5 V, scaling is user-selectable.
Synchronization	TTL (5V tolerant) sync in/sync out, start on sync, sample on sync
⟶ Connectors	
Bulkhead	MCBH-8-FS
Cable	PMCIL-8-MP on 10 m polyurethane cable
⟶ Software	
Functions	Deployment planning, instrument configuration, data retrieval and conversion (for Windows®).
⟶ Multi unit operation	
Software	N/A
I/O	N/A
⟶ Power	
DC input	9-15V DC
Maximum peak current	3 A
Max. consumption	1.5 W at 64 Hz
Typical consumption, 4 Hz	0.6 - 1 W
Sleep consumption	< 100 µA
Transmit power	2 adjustable levels
⟶ Batteries	
Battery capacity	50 Wh (alkaline or Li-ion),165 Wh (lithium), single or dual
New battery voltage	13.5 V DC (alkaline)
Data collection capacity	Refer to planning section in software
⟶ Environmental	

Figure A.7: Technical data ADV 3. *Nortek* 2021

A

Operating temperature	-4 to +40 °C
Storage temperature	-20 to +60 °C
Vibration	IEC 60068-1/IEC60068-2-64
Depth rating	300m
⟶ Materials	
Standard model	POM housing, titanium probe and fasteners
⟶ Dimensions	
Maximum diameter	75 mm
Maximum length	468 mm (housing only), 246 mm (fixed stem) add 110 mm for double battery
⟶ Weight	
No batteries	Weight in air: 2.32 kg, in water: buoyant
2 batteries	Weight in air: 3.20 kg, in water: 0.54 kg
⟶ Options	
Probe mounted on fixed stem or on 2 m cable	
Vertical or horizontal probes	
Alkaline, lithium or Li-ion external batteries	
IMU - Inertial Measurement Unit	

Figure A.8: Technical data ADV 4. *Nortek* 2021

A.1.3. ADCP

The used User setup is given in A.13.

```
User setup
-----------------------------------------------------------------------
Measurement/Burst interval              1800 sec
Cell size                               100 mm
Orientation                             UPLOOKING SHALLOW WATER
Distance to surface                     2.00 m
Extended velocity range                 ON
Pulse distance (Lag1)                   1.00 m
Pulse distance (Lag2)                   0.33 m
Profile range                           0.70 m
Horizontal velocity range               0.91 m/s
Vertical velocity range                 0.39 m/s
Number of cells                         7
Average interval                        1 sec
Blanking distance                       0.104 m
Measurement load                        20 %
Burst sampling                          ON
Samples per burst                       7200
Sampling rate                           8 Hz
Compass update rate                     1 sec
Analog input 1                          NONE
Analog input 2                          NONE
Power output                            DISABLED
Powerlevel first ping                   HIGH-
Powerlevel ping 2                       HIGH
Coordinate system                       XYZ
Sound speed                             MEASURED
Salinity                                32.0 ppt
Number of beams                         3
Number of pings per burst               1
Software version                        1.11.03
Deployment name                         Oyst4
Wrap mode                               OFF
Deployment time                         16.12.2020 12:00:00
```

Figure A.9: Used configuration for the ADCP

Below the most important technical data of the used ADVs is laid out. The full information can be found on *Nortek* 2021

A

Technical specifications

→ Water velocity measurements	
Maximum profiling range	12-25 m
Cell size	0.3-4 m
Minimum blanking	0.20 m
Maximum number of cells	128
Measurement cell position	N/A
Default position (along beam)	N/A
Velocity range	±10 m/s
Accuracy	±1% of measured value ±0.5 cm/s
Velocity precision	Consult instrument software
Maximum sampling rate (output)	1 Hz
Internal sampling rate	7 Hz
→ Echo intensity (along slanted beams)	
Sampling	Same as velocity
Resolution	0.45 dB
Dynamic range	90 dB
Transducer acoustic frequency	1 MHz
Number of beams	3
Beam width	3.4°

Figure A.10: Technical data ADCP 1. *Nortek* 2021

⟶ HR option	
Maximum profiling range	6 m
Cell size	20-300 mm
Minimum blanking	0.2 m
Maximum number of cells	128
Range/Velocity limitations	Product of profiling range and velocity should not exceed 1.0 m2/s
Accuracy	±1% of measured value ±0.5 cm/s
Max. sampling rate	1 Hz (continuous mode), 8 Hz (burst mode)
⟶ Z-Cell option	
Cell zero acoustic frequency	N/A
Maximum profiling range	N/A
Number of beams	N/A
⟶ Sensors	
Temperature:	Thermistor embedded in head
Temp. range	-4 to +40 °C
Temp. accuracy/resolution	0.1 °C/0.01 °C
Temp. time response	10 min
Compass:	Magnetometer
Accuracy/resolution	2°/0.1° for tilt < 20°
Tilt:	Liquid level
Accuracy/resolution	0.2°/0.1°
Maximum tilt	30°
Up or Down	Automatic detect
Pressure:	Piezoresistive
Range	0-100 m (inquire for options)
Accuracy/precision	0.5% FS / 0.005% of full scale
⟶ Analog inputs	
No. of channels	2
Supply voltage to analog output devices	Three options selectable through firmware commands: 1) Battery voltage/500 mA, 2) +5 V/250 mA, 3) +12 V/100 mA

Figure A.11: Technical data ADCP 2. *Nortek* 2021

A

⟶ Analog inputs	
Voltage input	0-5 V
Resolution	16 bit A/D
⟶ Data recording	
Capacity	9 MB, can add 4/16 GB
Data record	9*Ncells + 32 bytes
Diagnostics record	N/A
Wave record	Nsamples * 24 + 60 bytes
Mode	Stop when full (default) or wrap mode
⟶ Real-time clock	
Accuracy	±1 min/year
Backup in absence of power	4 weeks
⟶ Data communications	
I/O	RS-232 or RS-422
Communication baud rate	300-115200 Bd
Recorder download baud rate	600/1200 kBd for both RS-232 and RS-422
User control	Handled via "Aquadopp" software, ActiveX®function calls, or direct commands with binary or ASCII data output
⟶ Connectors	
Bulkhead	MCBH-8-FS
Cable	PMCIL-8-MP on 10 m Polyurethane cable
⟶ Software	
Functions	Deployment planning, instrument configuration, data retrieval and conversion (for Windows®)
⟶ Power	
DC input	9-15 V DC
Maximum peak current	3 A
Avg. power consumption	0.05 W
Sleep current	< 100 µA
Transmit power	0.3-20 W, 3 adjustable levels

Figure A.12: Technical data ADCP 3. *Nortek* 2021

→ Batteries	
Battery capacity	1) 50 Wh (alkaline or Li-ion), 2) 165 Wh (lithium), 3) Single or dual
New battery voltage	13.5 V DC (alkaline)
→ Environmental	
Operating temperature	-5 to +40 °C
Storage temperature	-20 to +60 °C
Shock and vibration	IEC 721-3-7
EMC approval	IEC 61000
Depth rating	300 m (3000 m option)
→ Materials	
Standard model	POM and polyurethane plastics with titanium fasteners
→ Dimensions	
Maximum diameter	75 mm
Maximum length	~550 mm (single battery), +110 mm (double battery) depending on head configuration
→ Weight	
Weight in air	2.2 kg
Weight in water	0.2 kg
→ Options	

1) Alkaline, lithium or Li-ion external batteries, 2) Inquire for different head configurations

Figure A.13: Technical data ADCP 4. *Nortek* 2021

A

A.2. PRESSURE DATA PREPARATION

The core of the data analysis used to determine wave attenuation was done with the pressure measurements of the OSSI devices. These produce data files in .csv format with a burst interval of 24 hours after which a new csv file is created. This ensures that a corrupted file does not lead to full data loss. Each file is closed approximately 10 seconds before the end of the 24 hour burst. The resulting missing data is filled up with NaN values so that all files have the same length of 864 000 data points (at 10 Hz in one day). The resulting files present raw pressure readings in respect to 1 bar. These have to be corrected for atmospheric (atm) pressure variations and individual calibration errors. To measure atm pressure at the measuring location a CTD sensor was placed at a point of high elevation on a close salt marsh. This device later showed no measurements due to a set up error. Thus atm pressure data of the Lichteiland Goeree station offshore of the Oosterschelde had to be used. After the atm correction the pressure time series was adjusted for calibration errors so that pressure readings equal zero during emergence. The above explained process is visualised in figure XX below. (still changes axes of this figure)

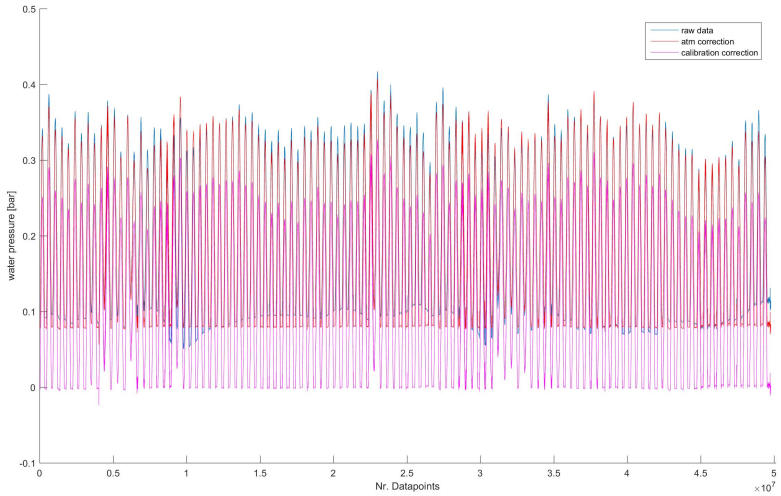

Figure A.14: correction of raw pressure data. Blue: raw data, red: atm corrected, pink: atm and calibration corrected

In order to measure at the set frequency rate, each measurement device is equipped with an internal clock. These can be reset at the start of the campaign but will still lead to individual clock offsets for each instrument. If the offset differences are large the time series have to be corrected to ensure comparability between the devices. Possible differences were determined by dipping the OSSI devices into Water at the end of the campaign, leading to a distinctive pressure signal in the time records. Unfortunately, 4 out of the 8

Ossis ran out of battery during the campaign, making it impossible to determine possible clock differences for those. For the remaining 4 Ossis, which still had battery left, the maximum time difference was determined as 2 minutes. This seems acceptable considering 15 minute time series and the rate at which storm conditions change.

A.3. CALCULATION WAVE ASYMMETRY

Matlab code used to calculate the wave asymmetry.

$$\begin{aligned} Hi &= imag(hilbert(eta)) \\ As &= nanmean((Hi.^3))/(nanmean(eta.^2).^(3/2)) \end{aligned} \tag{A.1}$$

Where eta is the detrended pressure time series and As indicates the asymmetry. Increasing negative As values hereby mean an increased asymmetry while As = 0 means no asymmetry.

A.4. DATA VALIDATION

Raw pressure measurements at ML2 are shown in A.15. The fluctuation with the passing waves is visible as well as the tidal trend.

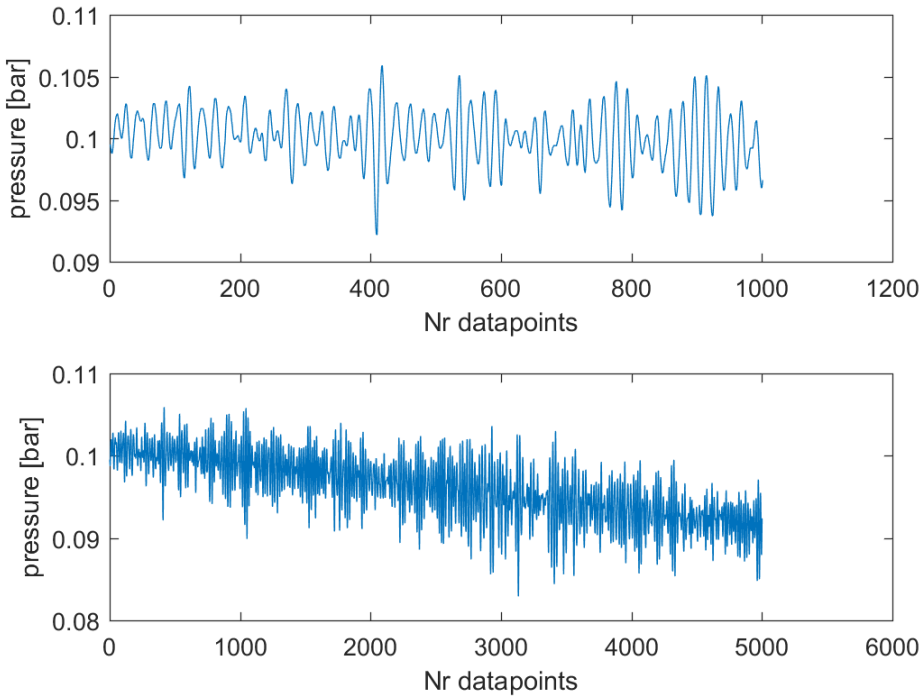

Figure A.15: measured raw pressure at ML2

Raw velocity measurements for all three beams of the ADV at ML2 are shown in A.16. THe fluctuation of the three beams with the orbital velocity are visible as well as a current.

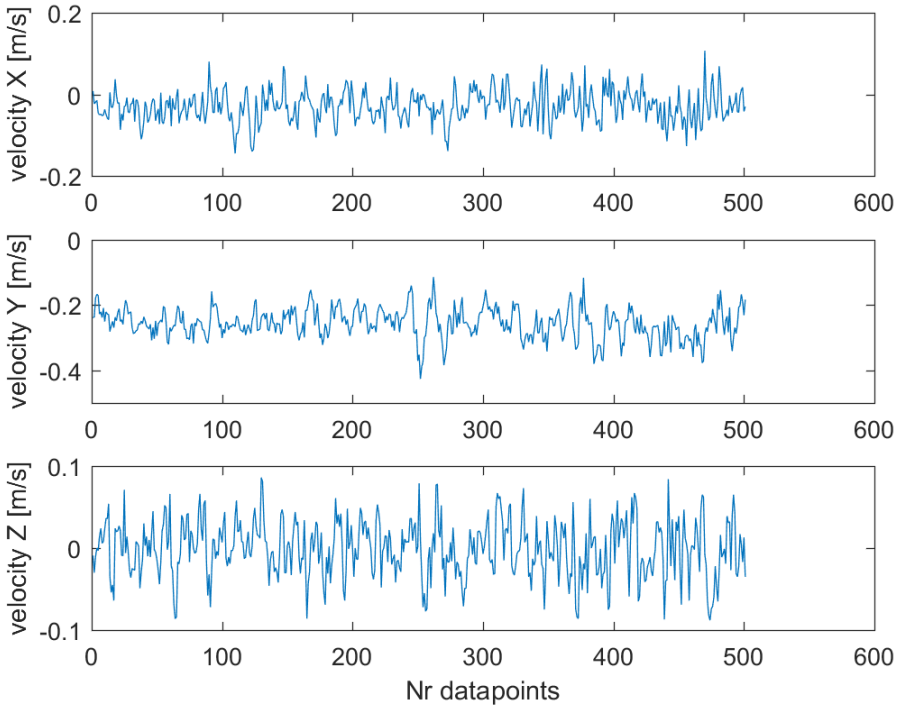

Figure A.16: measured raw velocity of three beams at ML2

To get an idea about the accuracy of the determined instrument elevation, the water depth time series derived from all instruments were converted into water elevations in respect to NAP and compared to the stations tidal data. Two tidal cycles are plotted in figure A.17 below, showing good agreement between all instruments and the reference station with deviations in the order of 2 cm. The inaccuracy only slightly increases to 4 cm during high energy events, meaning that no significant set up was recorded on top of the tidal flat. The horizontal lines at low tide indicate the elevation until which the devices are submerged and can record data.

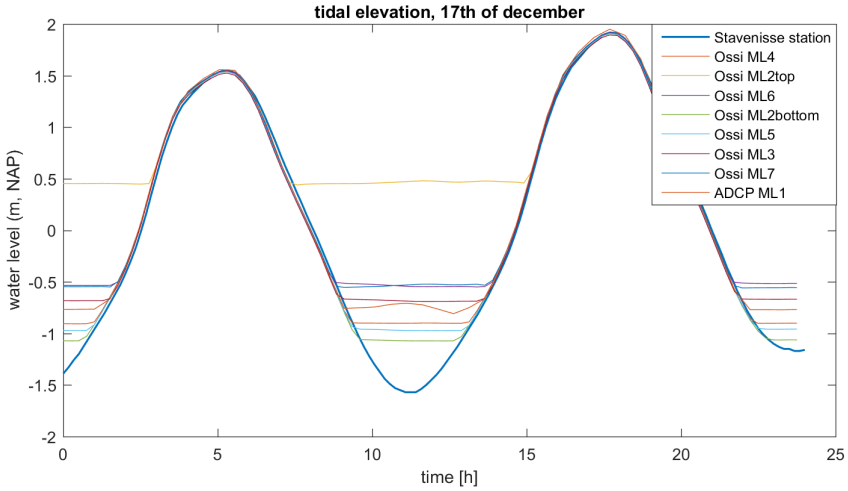

Figure A.17: Tidal data retreived from Stavenisse (*Rijkwaterstaat* 2021) compared to water elevation data from OSSI and ADCP measurement devices on the 17th of December 2020.

A

A.5. SPECTRA EVOLUTION

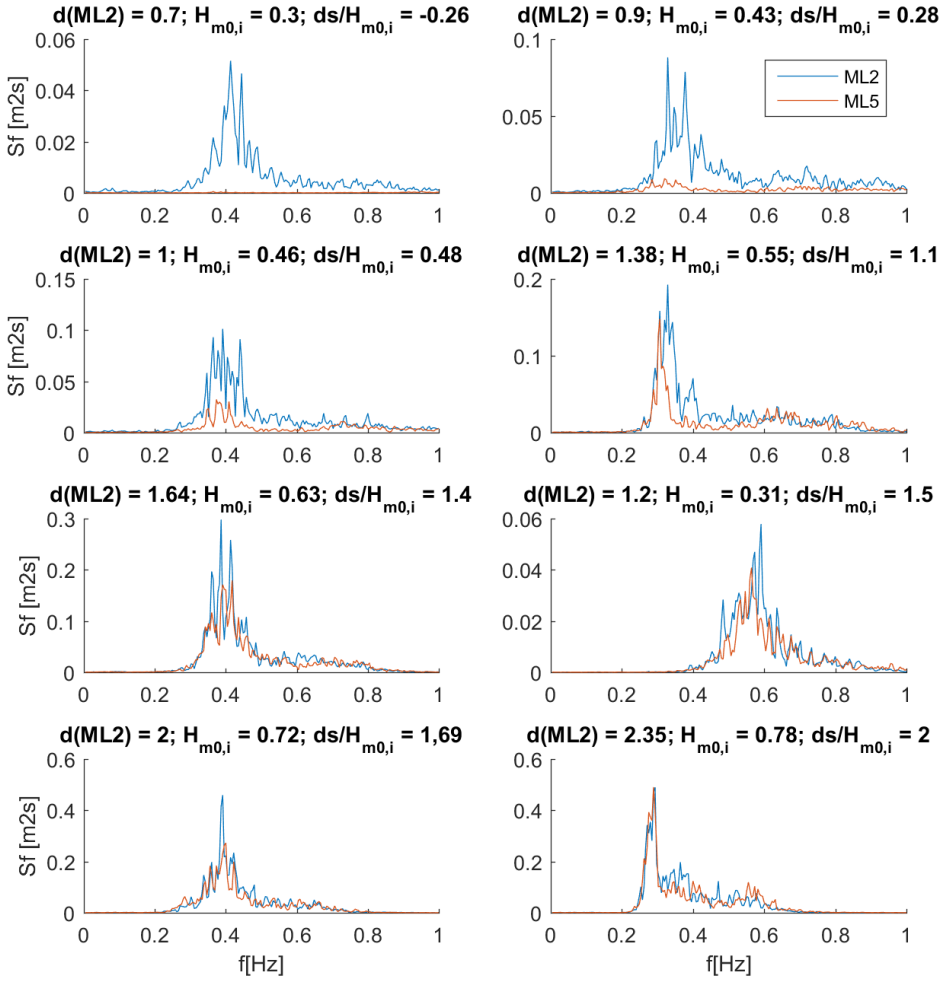

Figure A.18: Spectral evolution of ML2ML5 under different conditions

A.6. UNCERTAINTIES AND SIMPLIFICATIONS

A.6.1. EMPIRICAL MODELLING FETCH RELATED WAVE GROWTH

It is assumed that there is no further wind energy input into the waves after the waves pass ML_1. This is reasonable if the two considered measurement locations are close to-

gether but can become a problem if large distances lie in between the considered measurement locations. The focus in this thesis lies in waves during storm conditions between the measurement locations of ML_2 and ML_5. With a distance of 50 m in between only little wind input is to be expected. For longer distances however, such as the 200 m in between $ML6$ and $ML7$ wind input can become significant. This effect of wind input was addressed in Kala 2016, where wave height loss due to a nourishment hook in the Oosterschelde was recovered within only 300 m. To give some insight about the expected wave growth due to wind at storm conditions some simple empirical relations are explored in the following(Holthuijsen 2009). These show wave growth in the order of 1 cm for distances of about 50 m and wave growth in the order of 10 cm for distances of several hundreds of meters, confirming the above assumption.

$$\widetilde{F} = \frac{F * g}{U_{10}^2} \tag{A.2}$$

$$\widetilde{H} = \widetilde{H_\infty}(tanh(k_1 * \widetilde{F^{m1}}))^p \tag{A.3}$$

$$\widetilde{H} = \frac{H * g}{U_{10}^2} \tag{A.4}$$

The results for some choices of the Fetch and the wind speed are given in the table below.

wave heigth [m]		**Fetch [m]**					
		50	**100**	**500**	**2000**	**2050**	**2500**
$\mathbf{U}_{10}[m/s]$	**10**	0.06	0.08	0.17	0.31	0.31	0.34
	15	0.09	0.12	0.26	0.48	0.49	0.53
	20	0.12	0.17	0.35	0.66	0.67	0.73

Table A.1: empirical wave heights estimated with fetch and wind speed

A.6.2. OTHER SIMPLIFICATIONS

Wave reflection is neglected. Part of the energy transported in the wave is not going to be attenuated or transmitted, but reflected from the reef. This reflected energy is transported back offshore, where it can have an impact on the measurements at ML_2. This impact is highest when the water level is below the reef crest, and a nearly all wave energy is reflected.

Also not taken into account are the wind or tidal induced currents which can be found on the tidal flat. Biofouling on the instruments can often lead to a degradation of the data quality in marine settings, when algae or other marine live start covering the instruments. For this campaign however, no biofouling was observed.

Furthermore, the instruments themselves and and their installation lead to inaccuracies. The accuracy for the used OSSI pressure measurements is given as ±0.05% at temperatures between 10 and 40 $°C$ (*ocean sensors* 2021). Since temperatures reached up to

A

$-10°C$ during the measurement campaign, the maximum inaccuracy can be expected to be higher. The ADCP has an accuracy of ±0.5% and a precision of ±0.005% for the pressure readings and an accuracy of ±1% or $\pm 0.5 cm/s$ for the velocity readings (*Nortek* 2021). The velocity readings of the Vector ADVs have an accuracy of ±0.5% or $\pm 1 mm/s$ (*Nortek* 2021). Additionally the stiffness of the measurement frames can lead to inaccuracies. While the frames for the ADV and ADCP could be build reasonably stiff, the poles on which the OSSIs were mounted experienced some freedom of movement. This was relatively small for the lower OSSIs but in the order of several centimeters for the higher mounted OSSIs. During high energy events the resulting swinging of the poles can then lead to additional noise in the measured time series.

Lastly the assumption of the applicability of linear wave theory will lead to inaccuracies in the results. The observed waves are expected to have some non linear characteristics, since the conditions on the tidal flat are mostly shallow, or intermediate water conditions. Some methods exist to introduce non linear terms to the wave analysis, but these add another level of complexity. Since linear wave theory is generally seen as sufficient for most practical applications in the field (Karimpour and Chen 2017), linear wave theory was thus chosen.

A.7. ASYMMETRY MEASUREMENT LOCATIONS

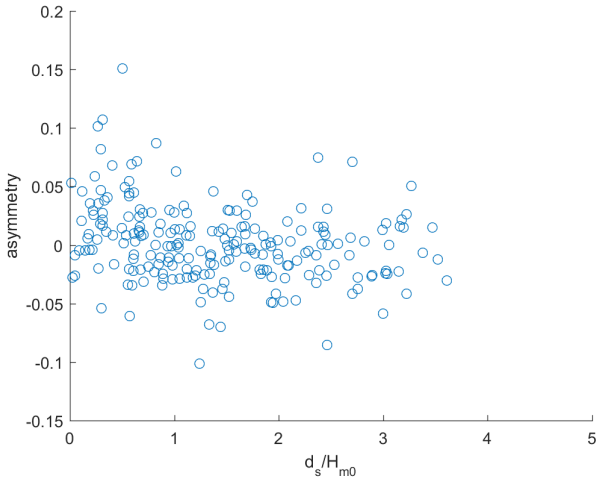

Figure A.19: Asymmetry plotted vs the relative submergence $d_s/H_{m0,i}$. $H_{m0,i}$ is the incoming wave height at ML2 and d_s is the reef freeboard. Asymmetry was measured at ML2. Asymmetry is increasing with negative values, a value of 0 indicates zero asymmetry. The asymmetry was only calculated for $d_s/H_{m0,i}$ values lower than 5.

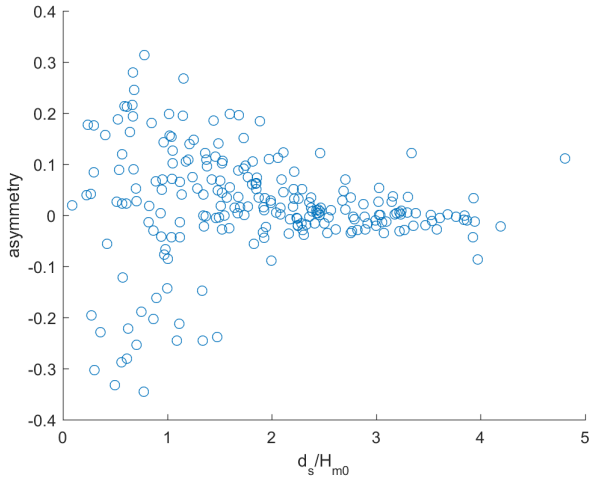

Figure A.20: Asymmetry plotted vs the relative submergence $d_s/H_{m0,i}$. $H_{m0,i}$ is the incoming wave height at ML2 and d_s is the reef freeboard. Asymmetry was measured at ML4. Asymmetry is increasing with negative values, a value of 0 indicates zero asymmetry. The asymmetry was only calculated for $d_s/H_{m0,i}$ values lower than 5.

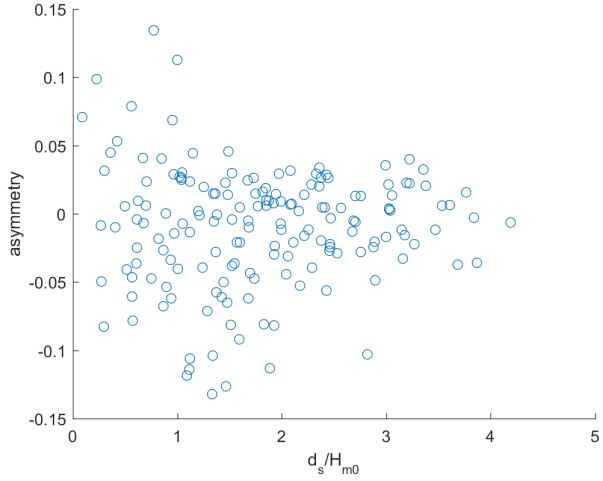

Figure A.21: Asymmetry plotted vs the relative submergence $d_s/H_{m0,i}$. $H_{m0,i}$ is the incoming wave height at ML2 and d_s is the reef freeboard. Asymmetry was measured at ML5. Asymmetry is increasing with negative values, a value of 0 indicates zero asymmetry. The asymmetry was only calculated for $d_s/H_{m0,i}$ values lower than 5.

A

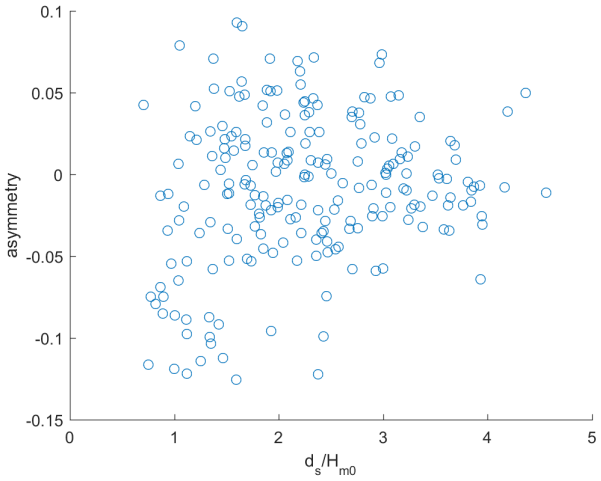

Figure A.22: Asymmetry plotted vs the relative submergence $d_s/H_{m0,i}$. $H_{m0,i}$ is the incoming wave height at ML2 and d_s is the reef freeboard. Asymmetry was measured at ML6. Asymmetry is increasing with negative values, a value of 0 indicates zero asymmetry. The asymmetry was only calculated for $d_s/H_{m0,i}$ values lower than 5.

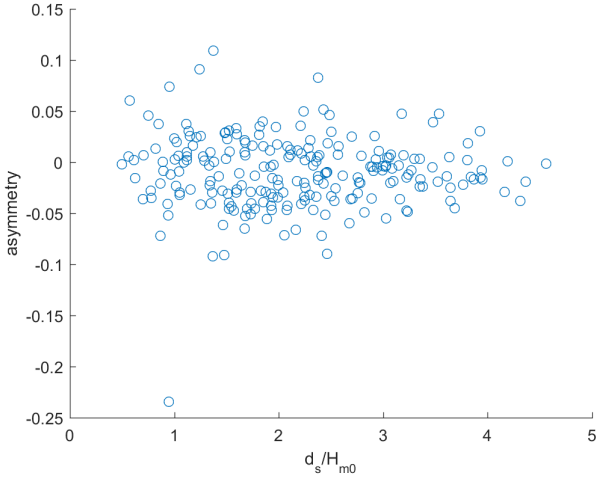

Figure A.23: Asymmetry plotted vs the relative submergence $d_s/H_{m0,i}$. $H_{m0,i}$ is the incoming wave height at ML2 and d_s is the reef freeboard. Asymmetry was measured at ML7. Asymmetry is increasing with negative values, a value of 0 indicates zero asymmetry. The asymmetry was only calculated for $d_s/H_{m0,i}$ values lower than 5.

A.8. PREDICTABILITY OF RESULTS WITH EMPIRICAL RELATIONS

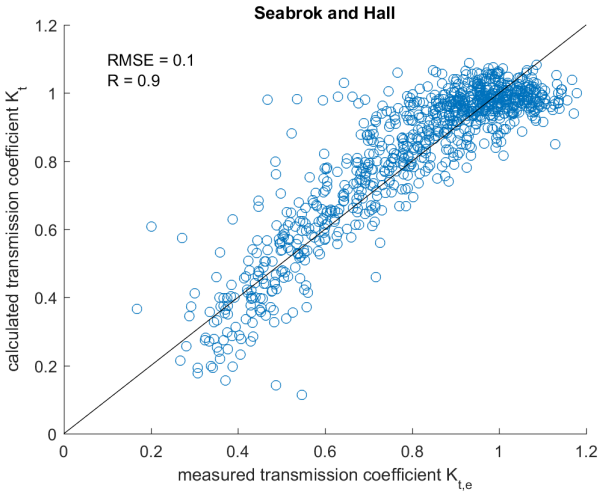

Figure A.24: Seabrook fitted with B = 1 m, D_{50a} = 0.1 m

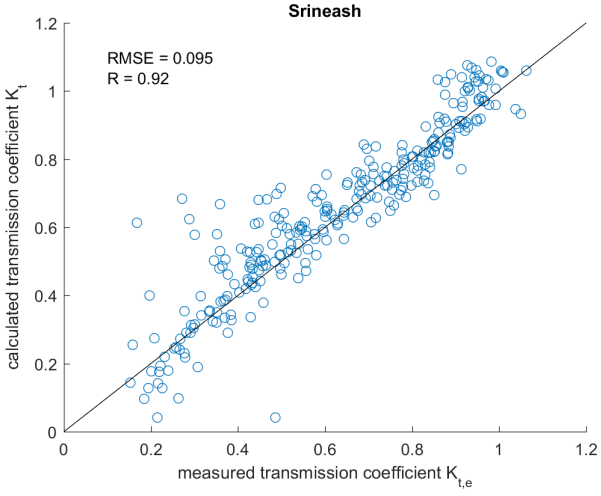

Figure A.25: Srineahs fitted with B = 3.5 m and h_s = 0.66 m

A

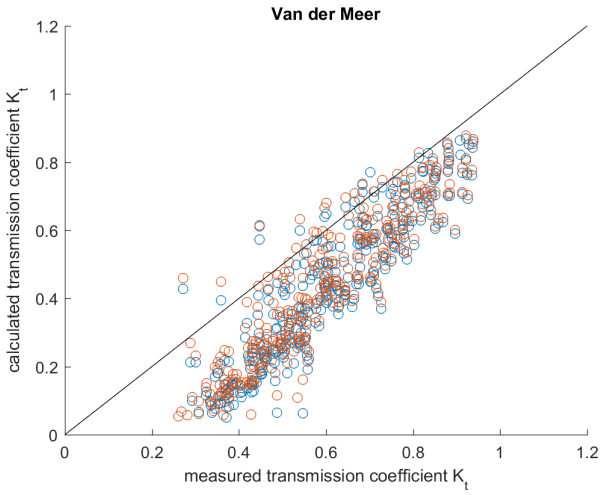

Figure A.26: Van der meer: Change of results for a d_s change of 1 cm

A.9. PERIOD DIFFERENCES IN BETWEEN ML2ML5

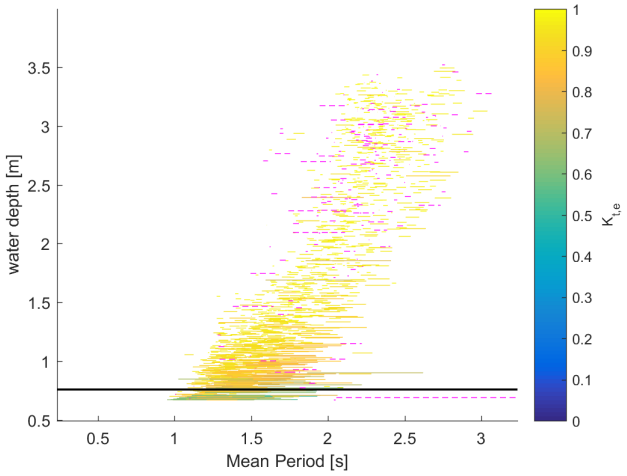

Figure A.27: Change in mean period between ML2 and ML5 indicated by lines. Lines colored in the color-code indicate a period decrease. Dashed lines in pink indicate a period increase